MICROFABRICATED DEVICES FOR FLUIDIC NEUROPROSTHETICS AND EXTRACELLULAR RECORDING *IN VITRO* AND *IN VIVO*

A Dissertation

Presented to the Faculty of the Graduate School

of Cornell University

in Partial Fulfillment of the Requirements for the Degree of

Doctor of Philosophy

by

Andrew Jack Howorth Spence

August 2003

MICROFABRICATED DEVICES FOR FLUIDIC NEUROPROSTHETICS AND EXTRACELLULAR RECORDING *IN VITRO* AND *IN VIVO*

Andrew Jack Howorth Spence, Ph.D.

Cornell University 2003

Microfabricated devices have been fabricated and used in three areas of neurobiology. Model brain prostheses were fabricated using deep reactive ion etching (DRIE) techniques, implanted in the rat cortex, and immunocytochemistry used to image the brain response. We have found that the immune response follows a two phase time course, an initial phase in which the response is proportional to device size, and a second phase in which the response is independent of device size. We then developed fabrication techniques to incorporate microfluidic channels for drug delivery on the chronically implantable probe. The second class of microfabricated devices were planar multielectrode arrays (MEAs), on which hippocampal neural networks were cultured. Microcontact printing (μCP) was used to pattern surface proteins to guide cell attachment and growth on the MEAs. Recordings of spontaneous activity across several recording sites were analyzed and compared with theoretical calculations and simulations. Finally, DRIE was combined with thin film electronic fabrication to produce multielectrodes of various geometries for recording from a system of neurons *in vivo*. Invertebrate sensory systems provided model systems in which to test these devices on small networks of neurons acting as an information channel. Devices for recording along the length of a nerve cord were tested on the ventral nerve cord of the cricket, where sixteen channel templates suitable for filtering multiunit activity were constructed for eight neurons. Simulations using our templates show that the device is capable of resolving isolated spikes from all eight neurons even in the presence of large amounts of background noise. In further simulations we

show that during bursts of activity the device can resolve four neurons, despite the large amount of neural activity and spike superposition. In order to improve the resolving capability of MEAs, devices with novel circumferential geometry were fabricated. Recordings around the circumference of the moth auditory nerve did not provide additional resolving capability. Tweezer multielectrodes, designed to record laterally across the top and bottom surfaces of nerve cords, were fabricated and tested. These devices improved the ability to create templates, but did not improve the ability to resolve overlapped spikes.

BIOGRAPHICAL SKETCH

Andrew Jack Howorth Spence was born February 25th, 1975 in Oxford, England to John Spence and Susan Somerville. After graduating in 1993 from Tempe High School, Andrew attended the University of California, Berkeley. He studied physics, with a minor in computer science, graduating in 1997. In the fall of 1997 he came to Cornell University to pursue a doctorate in Applied and Engineering Physics.

ACKNOWLEDGEMENTS

My foremost acknowledgement goes to my thesis advisor, Michael Isaacson, for his support and invaluable critical evaluation of this work. Ron Hoy provided great direction and was an incomparable mentor. The advising of Harold Craighead was likewise central to this project.

I would also like to thank Conrad James, the Isaacson lab, Scott Retterer, Keith Neeves, Marc Meyer, Steve Turner, the Cornell Nanofabrication Facility, the Wadsworth Center and William Shain, Jim Turner, Natalie Dowell, Beth Sipple, and Don Szarowski. Members of the Hoy lab, including Damien Elias, Nicole VanderSal, Elke Buschbeck, and Eileen Hebets were instrumental in their support. I have been fortunate in the long term support of my friends, Jeff Fox, Dan Larson, Mike Levene, Kevin Brown, and Mike Enyeart. I would like to thank the Applied & Engineering Physics department, the Keck Foundation for their generous fellowship support, and the National Institutes of Health for supporting the neuroprosthetics work. In addition, Professors Silcox, Lovelace, and Kusse gave me added direction and personal guidance. For love and support, Rebecka Rosenquist. Most of all, my thanks go to my parents, John Spence and Susan Somerville.

TABLE OF CONTENTS

LIST OF TABLES

LIST OF FIGURES

LIST OF TERMS

DRIE – Deep reactive ion etching
MEA – Multielectrode array
μCP – Microcontact printing
MEMS – Microelectromechanical systems
PLL – Poly-L-lysine
GI – Giant interneuron
GFAP – Glial fibrillary acidic protein
SOI – Silicon on insulator
KOH – Pottassium hydroxide
BOX – Buried oxide
GLUT-1 – Glucose transporter-1
PECVD – Plasma enhanced chemical vapor deposition
HF – Hydrofluoric acid
SNR – Signal to noise ratio
ECM – Extracellular matrix
SAM – Self-assembled monolayers
PEI – Poly(ethyleneimine)
PDMS – Polydimethylsiloxane
AFM – Atomic force microscopy
HMDS – Hexamethyldisilazane
MEM – Mimimum essential media
RT – Room temperature
MAP2 – Microtubule associated protein
DIV – Days *in vitro*
DIP – Dual inline package
ICA – Independent component analysis
EEG – Extracellular encephalogram
NEO – Nonlinear energy operator
PCA – Principal components analysis
CNS – Central nervous system
FET – Field effect transistor
PCB – Printed circuit board
A/D – Analog to digital converter
FFC – Flat flex cable
BSA – Bovine serum albumin

CHAPTER 1: INTRODUCTION

The ongoing drive to produce faster, cheaper, and smaller integrated circuits for the consumer electronics industry has resulted in profound advances in micro- and nano-fabrication technology. These techniques are continuing to find broader application. Perhaps the first major field to split from integrated circuits was microelectromechanical systems (MEMS). Designed primarily for sensing and actuating, these devices found success as accelerometers and inkjet printer nozzles. In recent years, however, attention has turned to biological systems [1]. The three-dimensional nature of devices developed for MEMS applications made them much more suited to the complex environments of biological systems. These devices were, and are, increasingly integrated, incorporating fluid channels, field effect antennae, cantilevers, and photonic structures among myriad other structures. With this capability comes a whole new set of tools for biological investigation, tools that can be applied across a range of size scales, from whole organs [2], to systems of cells [3], to single biomolecules [4]. This new field is interdisciplinary in nature, and has lead to an explosion of collaboration across engineering, biology, chemistry, materials science, and physics [5]. In addition to the application of microfabrication to biological systems, design principles found in nature have been mimicked or utilized in technology. Miniature transducers found in insect sensory systems have led to examples of biomimickry in microdevices [6] while their locomotive abilities have led to advances in robotics [7]. This new collaboration at the micro- to nanometer length scale is helping scientists tackle difficult questions in each discipline in innovative ways, and is rapidly pushing back scientific frontiers.

1.1 Fluidic Neuroprosthetic devices and Biocompatibility

Understanding and controlling the interface between biological tissue and artificial devices is vital to both biological science and technology. Having control of this interface means not only better treatment of disease via prosthetics and drug delivery devices, but is of great importance to biology in the ability to chronically probe and stimulate natural structures *in vivo*. The development of neuroprosthetic devices to restore nervous system function, lost due to trauma or disease, has been investigated for nearly three decades [8-13]. Such devices are becoming a practical reality in both the peripheral [8, 14-22] and central nervous systems [23-28]. The most notable successes in humans are the alleviation of symptoms due to Parkinson's disease via deep brain stimulation [25, 27, 28] and deafness using cochlear implants [29-31]. More recently, Prosthetic devices that interface to the visual system in higher centers [30-35] and more recently in the retina [32-34, 36] are likewise becoming feasible, and even showing positive rehabilitation in humans. Prostheses in the brain have been successfully used as a method of communication for a paralyzed patient, who has primitive control over external devices using thought [37].

One of the most important factors limiting progress in neural prosthetics, however, is encapsulation of implanted devices by neural tissue as part of the immune response [38-41]. During chronic implantation, a protective, electrically insulating, astrocyte-glial cell sheath forms around the probe, rendering long-term cellular recording and stimulation nearly impossible (Figure 1.1). Although devices have been successful in recording from and stimulating single units and groups of neurons, the short- and long-term stability of the connection is very poor. The yield of stable recording sites is thought to be about 30 percent at best [42].

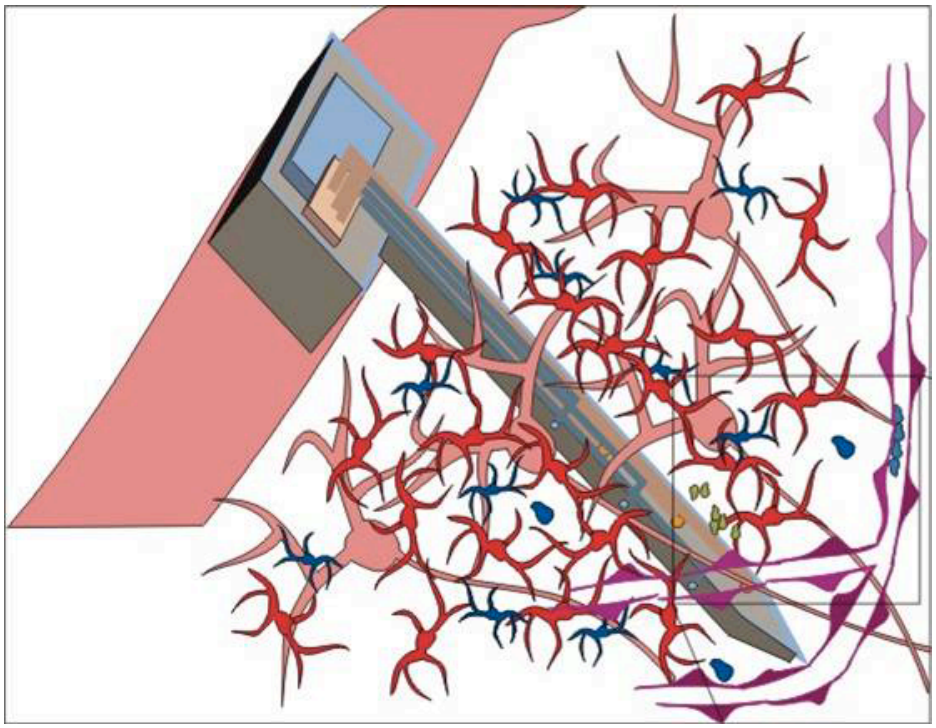

Figure 1.1 Schematic of Neural Tissue Response to Prosthetic Device
The prosthetic device is shown in grey, with fluid channels (blue) and electrical connections (gold). Neurons (pink), microglia (blue), astrocytes (red), and vasculature (purple) are seen encapsulating the probe. Figure taken from [43].

Several approaches have been taken to improve the biocompatibility of these devices. Control of device size, and utilization of micro- and nano-fabrication techniques to miniaturize the probe is one promising approach. Changes in surface chemistry can also be used to affect the probe-tissue interface. Delivery of biologically relevant modulatory agents to the insertion site is another technique, one that is well suited to the microfabrication of fluidic channels [44]. Our results indicate that simple modifications to probe geometry and surface chemistry are not enough to prevent an insulating long-term response [43]. Accordingly, there is a need for a) an understanding of the cell signaling pathways underlying the immune response, b) candidate neuromodulators to be identified from this understanding, and c) a means to

deliver these drugs to the insertion site. We have developed chronically implantable probes that incorporate microfluidic channels to address the problem of drug delivery.

1.2 Substrate Multielectrodes for Patterned Neural Cell Culture

The motivation to establish a chronic two way connection to neuronal cells comes from the desire to understand how neuronal networks compute. The mammalian brain is a fascinating and complex structure whose massive parallelism, adaptability, and superior pattern recognition capabilities make it an attractive specimen for investigation not just by neuroscientists, but also by computer hardware engineers and software programmers. In fact, artificial neural networks, which are mathematical models based upon neuronal cell and cell network theory and operation, are used for recognizing domains in protein sequences and predicting behavior of chaotic systems such as weather patterns [45, 46]. Specifically, the hippocampus has been of extreme interest to researchers due to its implication in learning and memory [47]. In order to investigate *in vivo* neuronal networks and to elucidate the mechanisms of computation, long-term investigations of neuronal cell networks are required. Spontaneous and elicited electrical activity need to be monitored, and multiple simultaneous recordings are required for monitoring individual unit and collective network activity. In this way, both individual cells and cell networks can be scrutinized in order to understand how changes in single unit activity and functionality shapes network development and operation through synaptic plasticity.

We present a method for producing neuronal cell networks on planar electrode array surfaces using poly-L-lysine (PLL) as a cell attachment cue. The PLL layer is selectively localized near electrode recording sites, and provides a surface for cell attachment and outgrowth of axons and dendrites. The layer is stable and robust enough to withstand dehydration and solvent exposure, and it exhibits strong and well-

characterized binding to silica surfaces that is reversible. Extracellular recording was accomplished using planar microelectrode arrays after two weeks of culture. Single units were successfully isolated using template matching and principal component analysis on multichannel recordings. Our array design offered excellent reproducibility and adequate spatial sampling with the arrangement of electrode recording tips.

1.3 Neuroethology and Invertebrates

Invertebrate organisms offer tractable systems in which to study the entire "input-output" relationship of an animal. Their sensorimotor systems are highly sophisticated, yet often small enough in neuronal number for quantitative examination (Figure 1.2). These properties make them well suited to one of the ultimate goals of neuroscientific research, often termed neuroethology: understanding the neural mechanisms underlying behavior [48-54]. In invertebrates the behavioral effects of genetics and biochemistry can often be directly studied, moving stepwise in level from the genetics to protein structure, to membrane dynamics, to network dynamics, to muscle movements, and finally behavior.

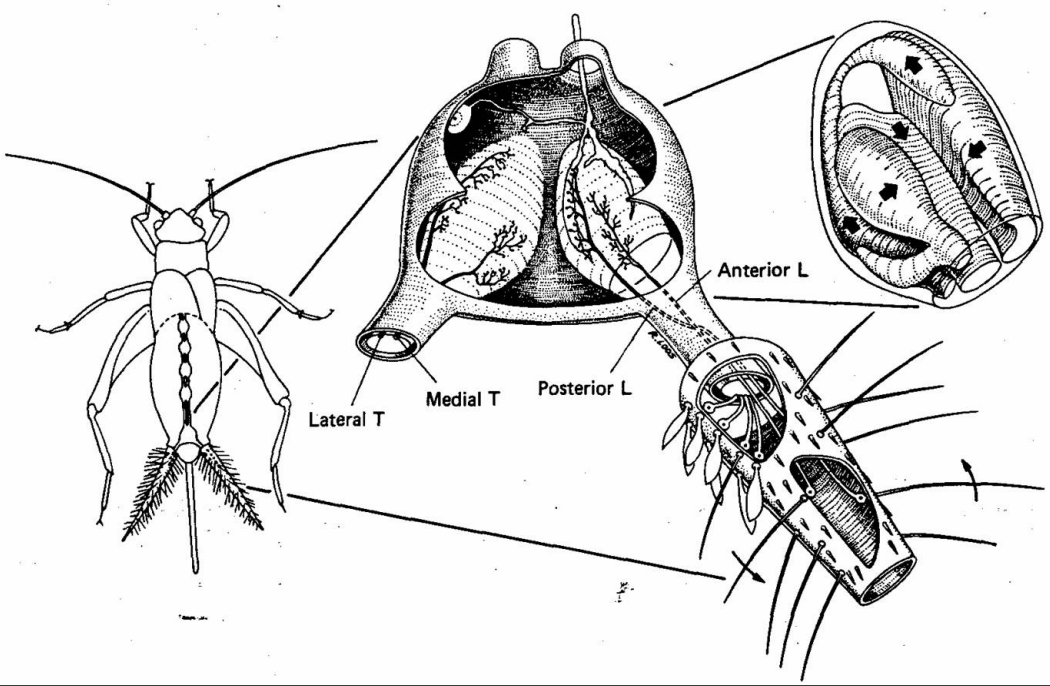

Figure 1.2. Example of an invertebrate neural ensemble
The cercal system of the cricket is an example of an ideal model system in which to study neural encoding (adapted from Bacon and Murphey, 1984 [55]). The cerci (conical appendages at the end of the abdomen, left)) are covered with mechanosensory filiform hairs. The hairs are sensitive to near field wind motion. Each hair is constrained to move in the horizontal plane and in one direction. The length of the hair determines it's frequency tuning characteristics. Primary afferent neurons from each hair project to the terminal ganglion (center), where they synapse onto giant internueurons which transmit information to higher centers via the ventral nerve cord. The terminal ganglion is organized in a volumetric map of wind direction. That is, axons sensitive to similar wind directions map into the same volume of the ganglion (right). The giant interneuron get their directional, frequency, and temporal wind sensitivity pattern by projecting dendrites into different parts of the ganglion. The sensitivity of the giant interneurons (GIs) can be predicted from their dendritic morphology, and hence the regions of the wind direction map they synapse into [56].

Likewise, behavioral tasks such as learning and memory can be traced backwards down to membrane channels and even genetic changes. An understanding of how information is transduced, computations performed, and motor output generated is possible, as is the case in studies of the thoracic nervous system of insects [57-59].

With advances in microfabrication the minute dimensions of invertebrate neural systems becomes less problematic, and their study becomes even more attractive.

1.4 Multielectrodes for *in vivo* Multineuron Electrophysiology

Even with the tractability of invertebrate neural systems, the technology to study more than one neuron simultaneously is only just emerging. The difficult experimental problem of recording the activity of several neurons simultaneously must be solved in order to make more rapid progress in our understanding of neural network computation. Most of what we know about neural systems comes from single unit studies. Ideally, the intracellular voltage of multiple neurons could be recorded over their full dynamic range and with high temporal precision. While intracellular techniques have adequate dynamic range and temporal resolution, for multi-unit recording the operator is required to independently penetrate each neuron with an electrode. This requires a high level of operator skill, several manipulators crowded around the preparation, and can cause damage to penetrated cells, limiting recording time. In many preparations, it is physically impossible. Optical techniques including voltage sensitive dyes offer an elegant solution to imaging groups of neurons, but suffer from poor dynamic range, temporal resolution, or signal to noise ratio [60]. Extracellular devices such as metal multi-wire arrays and microfabricated silicon multielectrodes have good temporal resolution, but sacrifice measuring any small synaptic potentials or DC behavior due to their capacitive coupling. In addition they are only easily constructed in planar or two dimensional geometries [61-65]. For studies of neural systems where information is carried in patterns of spike arrival times, however, extracellular multielectrode techniques are proving a useful tool in resolving the firing times of multiple neurons [66]. A large fraction of previous silicon and multiwire array work has focused on fabricating devices for mammalian brain

studies, where priority has been given to small cross sectional area, in order to minimize damage during insertion. For studies of invertebrate neural systems, however, device structure can be optimized for unit discrimination and identification. These invertebrate ensembles have fewer neurons than vertebrate systems, yet offer model systems in which to study general principles of neural coding.

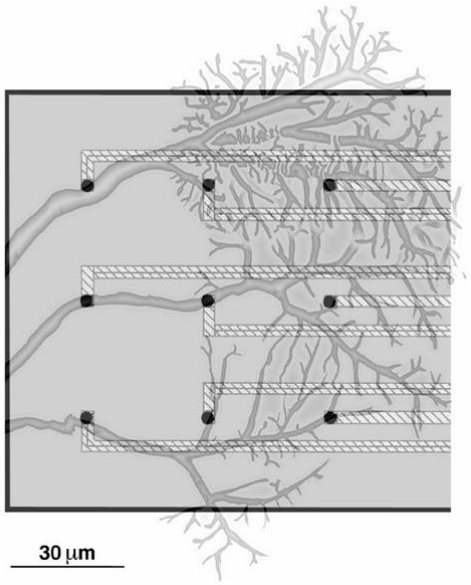

Figure 1.3. Schematic of a multielectrode and fly visual neuron anatomy
This sketch illustrates the use of multielectrodes in neural recording. A group of recording sites record the activity of a small number of neurons, analogous to an antennae array picking up signals emanating from a group of cables.

One of the difficult problems in analyzing data produced by multielectrode arrays is the resolution of overlapped spikes. Resolving overlapped spikes is a combinatorial problem that has only been solved adequately in selected preparations. Gozani and Miller used a two step process of multichannel spike template creation and optimal linear filtering that benefited from conduction velocity information garnered over the relatively large (1 cm) length of nerve available in the cricket preparation [67]. They were able to resolve the firing times of four giant interneurons of the cricket cercal system, inclusive of activity with a high degree of spike overlap. The

cercal system has become a test bed for some very exciting analyses of neural encoding [68-72]. The recording apparatus in this case consisted of eight metal wires, deinsulated at the midpoint, and spaced evenly underneath the nerve. Rinberg and Davidowitz have recently used 8 hook electrodes and a Fourier domain spike sorting algorithm in the cercal system of the cockroach [66]. How many and what geometric configuration of recording sites are necessary to resolve the activity of multiple neurons remains an open question. Microfabricated devices have the advantage of scalability to high numbers of recording sites (Figure 1.3).

Another drawback of extracellular multielectrodes lies in identifying which neuron produces each discriminated spike. In invertebrates, the diameter and location of axons within a nerve cord is consistent from specimen to specimen, offering additional information that can be used to identify them *in situ*. Precise measurement of conduction velocity may be a means to identify neurons *in situ* from known histology. This requires recording sites spaced at known distances, and validation via simultaneous intracellular studies. We demonstrate the functionality of silicon multielectrodes designed specifically for nerve cord preparations, that samples spike conduction at several known positions, and can be used in conjunction with intracellular recording.

1.5 Thesis Objectives

We present microfabricated devices that have specific advantages over previous tools in three areas of neurobiology. The background, fabrication, results, and limitations of our neuroprosthetic devices and cell culture MEAs will be discussed, and a detailed treatment of how their fabrication technologies were combined to produce multielectrodes for *in vivo* studies of invertebrates is presented in Chapter 4.

Model neuroprosthetic silicon probes that have precisely controlled geometry, surface chemistry, and insertion kinetics have been fabricated. Part of these probes functions as a handle for precise gripping by an aligned insertion device. This precise alignment is important in quantifying what spatial extent of the immune response is due to the presence of the probe, and not due to excess tearing due to misalignment on insertion [41]. We use these devices to elicit an immune response in the brain of rats, and document the biological response using histological and confocal microscopic methods [42, 73]. We discuss the effects of varying probe geometry, size, surface chemistry, and insertion method. We present the finding of a two-phase immune response, including one that is independent of surface chemistry and probe size. Our incorporation of fluidic channels in the probe is then discussed, including modifications to the fabrication process, and testing.

We then present a method of fabricating substrate MEAs suited for *in vitro* studies of cultured neuronal cells. MEAs with 124 recording sites were fabricated, and methods to pattern chemical guidance cues for growing patterned neurons successfully used. Imaging of neuronal morphology and electrophysiological recordings are presented, and an analysis of the multichannel waveforms carried out. Equivalent circuit and volume conductor models of the electrode-neuron interface are used to explain the extracellular waveforms.

Finally, a method for fabricating multielectrodes with more complicated geometry, and their testing *in vivo* in invertebrate preparations is presented. We discuss development of the fabrication process, characterization of the devices, and their use in neural recording. Development of the geometry of the devices to best discriminate spikes from different neurons is shown. Geometries for separating neurons based on differences in their spike conduction velocity are shown to

discriminate 8 units in the ventral nerve cord of the cricket. Methods in spike sorting, in particular with multichannel arrays, are presented. A multielectrode hook that records the circumferential potential distribution about the moth auditory nerve is presented, and its limitations discussed. Finally, we present the development of interconnection systems to overcome the limitations of sealing impedance through tweezing electrodes, and the results of testing these tweezing multielectrodes.

CHAPTER 2: NEUROPROSTHETIC MICRODEVICES

The relatively crude neuroprosthetic devices used in the early studies discussed in the introduction were able to show a great deal of promise in the treatment of nervous disorders. As such it is clear these devices, especially in the brain, will substantially benefit from miniaturization and semiconductor integration. In the human brain target regions often have linear dimensions of a few millimeters, leaving plenty of "real estate" for devices with sophisticated features. Miniature neuroprosthetics with advanced engineering capabilities have been fabricated using the technology of micro- and nano-fabrication developed by the electronics industry [10, 74]. Some of these devices have on-board electronics, including telemetry [75, 76], and others have multiple electrodes, some with complex three-dimensional electrode arrays [74, 76-81]. The shafts of these devices have dimensions measured in 10 to 100s of micrometers, thus making it possible to insert a device into a target region.

Again, the long term function of all of these devices is limited due to cellular encapsulation that electrically and mechanically isolates the prosthesis from the brain [38, 39, 41, 73, 77]. This tissue response occurs following implantation of many materials other than silicon [8, 22, 82-84]. It has been generally described by visualizing reactive gliosis, especially the hypertrophy and increased expression of glial fibrillary acidic protein (GFAP) by astrocytes [85-90]. We have demonstrated that astrocytes are a major cell type in the cellular sheath around inserted silicon devices [42]. It is clear that microglia are also present [42, 73]. Until this response is understood and reduced, however, the usefulness of neuroprosthetics will be limited. In order to quantify the immune response, we present here the development a microfabrication process that permits construction of model prosthetic devices of

controlled geometry, and that can incorporate microfluidic channels. We report the effects of varying the device cross-section and surface properties on the immune response.

2.1 Model neuroprosthetic device fabrication and insertion

2.1.1 *Silicon On Insulator (SOI) Probe Fabrication*

The first generation devices fabricated for this study used a KOH wet etch process, yielding devices of trapezoidal cross section [42]. While this fabrication process was relatively simple, the KOH etch results in sidewalls angled at 54 degrees to surface normal, limiting the probe shank to a relatively large width at the base. This limitation, coupled with the need for automated, reproducible, carefully aligned insertion of the prosthetic devices led to development of a new fabrication process. The recent acquisition of a PlasmaTherm 770 DRIE system meant that anisotropic etching of bulk silicon was now a possibility. Used extensively in MEMs devices, this plasma etching system etches silicon at ~ 2 μm / minute, and through cyclic chemical deposition/etching steps can yield deep trenches with sidewalls having aspect ratios of approximately 20:1 (depth:lateral undercut). These attributes meant that a) devices with more complicated (3D) structure could more easily be constructed, and b) features of intermediate scale (hundreds of microns) could also be fabricated, alleviating many of the interconnection problems associated with standalone thin film devices. Mechanisms by which an automated insertion device consisting of machined clamping forceps could grasp the probe were discussed, and a three point alignment system was decided upon. The probe was required to have a macroscopic cubic “tab” at the base of the shank, which could in turn be grasped on three sides (providing alignment) by the forceps. The forceps consisted of one flat tong opposing two pins,

and when closed around the "tab" of the probe, it aligns the probe shank to the axis of the forceps (Figure 2.2). To facilitate gripping with the forceps, the "tab" was specified to be cubic, 500 μm on a side.

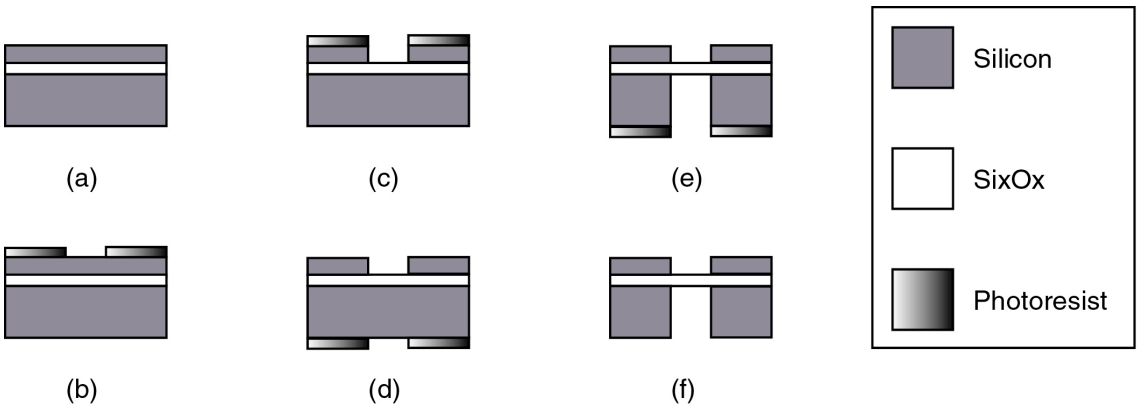

Figure 2.1 Detailed fabrication process for SOI probes
(1) SOI wafer substrate: 100 mm silicon device layer, 1 mm buried oxide layer, 400 micron thick "handle" layer. (2) Spin coating of device layer with thick resist. (3) DRIE of device layer, stopping at buried oxide layer. (4) Spin coating of handle layer with thick resist. (5) DRIE of handle layer. (6) Completed device after resist strip.

In order to fabricate a device consisting of this macroscopic tab section and a miniature probe shank, a process utilizing Silicon-on-insulator (SOI) wafers and the DRIE was formulated [43]. The fabrication process is displayed schematically in Figure 2.1, and a 3D view of the overall probe structure is seen in Figure 2.2. SOI wafers consist of a thin (<100 microns) silicon device layer, a thin film (~ 1 micron) of silicon dioxide or buried oxide (BOX) layer, and a thick (500 microns) silicon "handle" layer (Figure 2.1a). The device layer used in probe fabrication was typically 100 microns thick, but substrates with 50 and 25 micron thick device layers were also used to make probes of smaller shank cross section. Fabrication begins with spin coating the device layer with photoresist (Figure 2.1b). A conservative estimate of the DRIE Silicon:photoresist selectivity is 50:1, thus any coating greater than 2.5 microns is adequate for the device layer etch. Shipley S1045 spun at 3000 rpm is adequate.

Resist is soft baked on a hotplate at 115°C for 90 seconds. The resist is exposed in a contact aligner, and developed for >2 minutes in an appropriate developer, such as AZ300MIF. The resist is not hard baked, as this was found to reflow the thick resist substantially, and did not improve selectivity. The outermost 5 mm of resist is then stripped to prevent the wafer sticking to the clamp inside the DRIE, and the wafer was deep etched. The DRIE etch rate was, unfortunately, a varying function of chamber condition, and hence machine age. After installation, etch rates were approximately 2.2 μm/minute. This rate dropped to about 1.6 μm/minute as the chamber was conditioned through use. The top viewport of the machine provided the only way to monitor etch status *in situ*. Fortunately, contrast in the etched trenches changed dramatically as the silicon was cleared to the buried oxide (BOX) layer (Figure 2.1c). The device could then be removed from the machine, and a profilometer used to verify completion of the etch. The DRIE etches silicon oxide at a very slow rate, (~ 20 nm / minute), making the BOX layer a good hard etch stop.

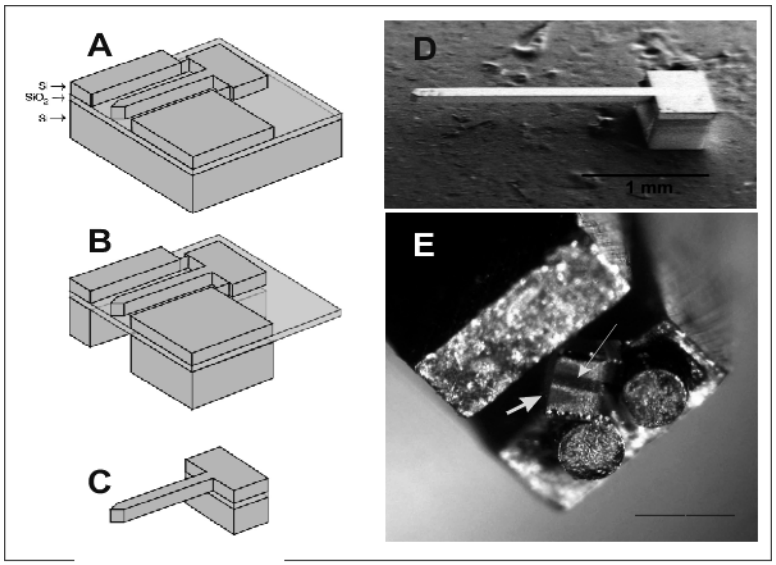

Figure 2.2. Schematic of SOI probe fabrication and insertion device.
A) The probe shank is etched in the 100 micron thick devices layer. B) The probe tab is etched in the backside "handle" layer. C) Schematic of completed probe broken out of wafer. D) SEM of completed probe. E) Image of probe held in inserter. Two surfaces of the probe tab are in contact the cylindrical pins, and a third alignment axis is the corner of the probe against the lower "tong" of the forcep. Figure adapted from [43].

Resist was then stripped from the device layer, using either an aggressive solvent clean, or an oxygen plasma for several minutes. Resist was then spun on the backside, or handle layer of the wafer. Etching through such a large thickness (400 microns) of bulk silicon often requires a hard (silicon oxide) mask, for it's increased selectivity. A user of the CNF had developed a recipe for spinning very thick films of photoresist, however, and this method was chosen for it's simplicity (Greg Borek, personal communication). Highly viscious resists such as Shipley S1075 which can provide the > 8 micron thickness necessary for this etch suffer from serious particle contamination problems when spun at 3000 or 4000 rpm. An alternative is to use Shipley S1045, a less viscous resist with identical photochemical properties, and spin at a much slower speed. Also critical was a dynamic deposit, pouring resist directly from the bottle while the wafer is spinning slowly. This minimizes the likelihood of

particle contamination while the puddle of resist is resting on the wafer. The final recipe contained 3 spins: 400 rpm for 5 seconds, 800 rpm for 5 seconds, and 1500 rpm for 30 seconds. The resist is poured directly onto the wafer during the first spin, coating ¾ of the wafer diameter. This recipe results in particle free films of thickness approximately 9 μm. Soft baking at 115 C for at least 2 minutes is then required. Exposure times for thick resist are quite long, the preceding film typically requiring 12 – 15 seconds at 27 mJ / cm^2. Additionally, the pattern must be aligned to the features etched in the other side of the wafer. A contact aligner equipped with infra-red optics, or some other backside alignment scheme for opaque substrates is required (Figure 2.1d). Upon development (this can be long, on the order of 3 or 4 minutes, for thick resist) the edge bead is again cleared, and the handle layer etched through to the BOX layer.

2.1.2 *Device insertion*

An illustration of the interconnection between the forceps of the insertion device and probe is seen in Figure 2.3. Probes are designed with their tab sections freely projecting from the edge of a wafer, such that the insertion device forceps can be placed around the device, closed on the device tab (breaking it free), and pulled away from the cleaved wafer. The automated inserter controls both insertion speed and penetration depth. The forceps and precision drive table were mounted on a stereotactic device, allowing accurate placement of devices. Devices were inserted 2 mm into the brain such that the bottom of the holding tabs rested on the brain surface. For a detailed account of the surgery and insertion procedure, see Appendix A.

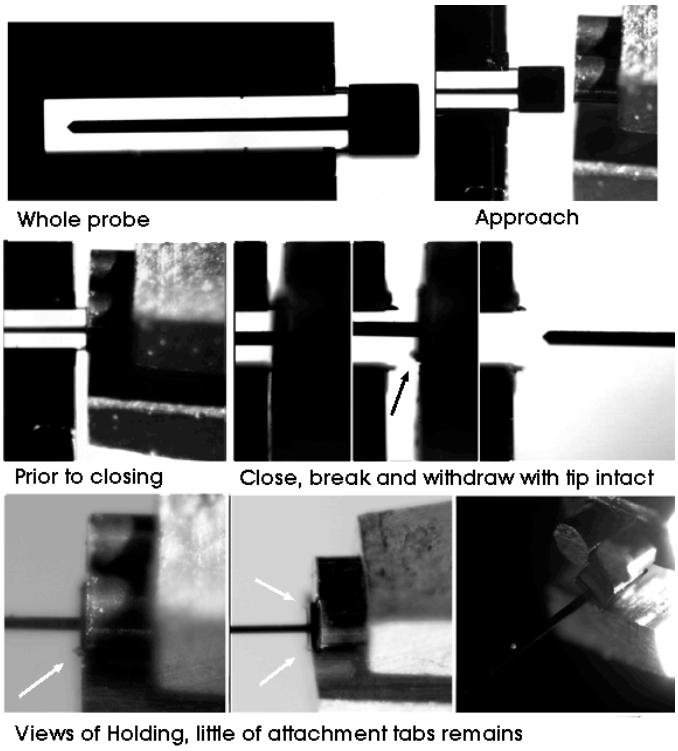

Figure 2.3. Illustration of probe interconnection and alignment
A completed probe has it's tab section protruding from a "comb" of devices. Inserter forceps are brought around the tab, then close on the device, breaking it free from the wafer. The probe is then aligned to this inserter via the pins and opposing tong.

2.2 Characterization of the immune response

The brain response to probes of different geometry and surface topology were examined using immunohistochemistry [91]. Probes were fabricated using the SOI process having a shank width of 100 microns and thicknesses of 25 and 100 microns. Probes fabricated earlier using the KOH etching technique and having a trapezoidal cross section were also used for comparison. In addition, thin (15 micron) probes with rounded corners were obtained from the Center for Neural Communication Technology (CNCT, University of Michigan, Ann Arbor). The devices are seen in Figure 2.4.

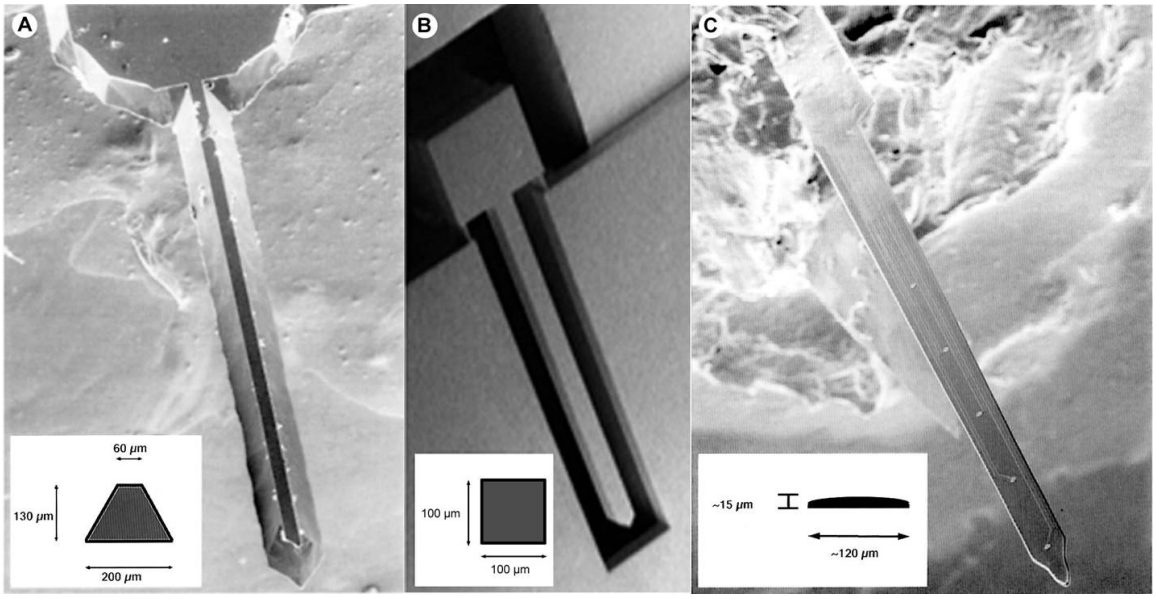

Figure 2.4. SEMs of probes used in analysis of the immune response
Three classes of probe were used in the immune response characterization, having varied cross sectional area and surface roughness. At left, KOH etched probes, center, SOI process probes, and at right, CNCT probes. Figure is taken from [43].

All animals recovered from surgery with no apparent adverse effects and all survived for the duration of the experiment. No behavioral, gross- or micro-pathology including infection were observed. Responses were assessed 1 day, 1, 2, 4, 6, and 12 weeks after insertions.

2.2.1 *Changes in immunoreactivity post-insertion*

See Appendix A for a detailed account of the histological methods used to image the brain response. Immunohistochemical staining for several indicators of reactive tissue were used to characterize the time course and spatial extent of the response, two of which are shown in Figure 2.5, for SOI probes. Glial fibrillary acidic protein (GFAP) immunoreactivity is a standard measure used for assessing reactive gliosis (22, 33, 41, 43, 55). Small, spindle-shaped GFAP-positive cells were presumed

to be astrocytes and were scattered throughout control tissues. These cells were most frequently observed around larger blood vessels.

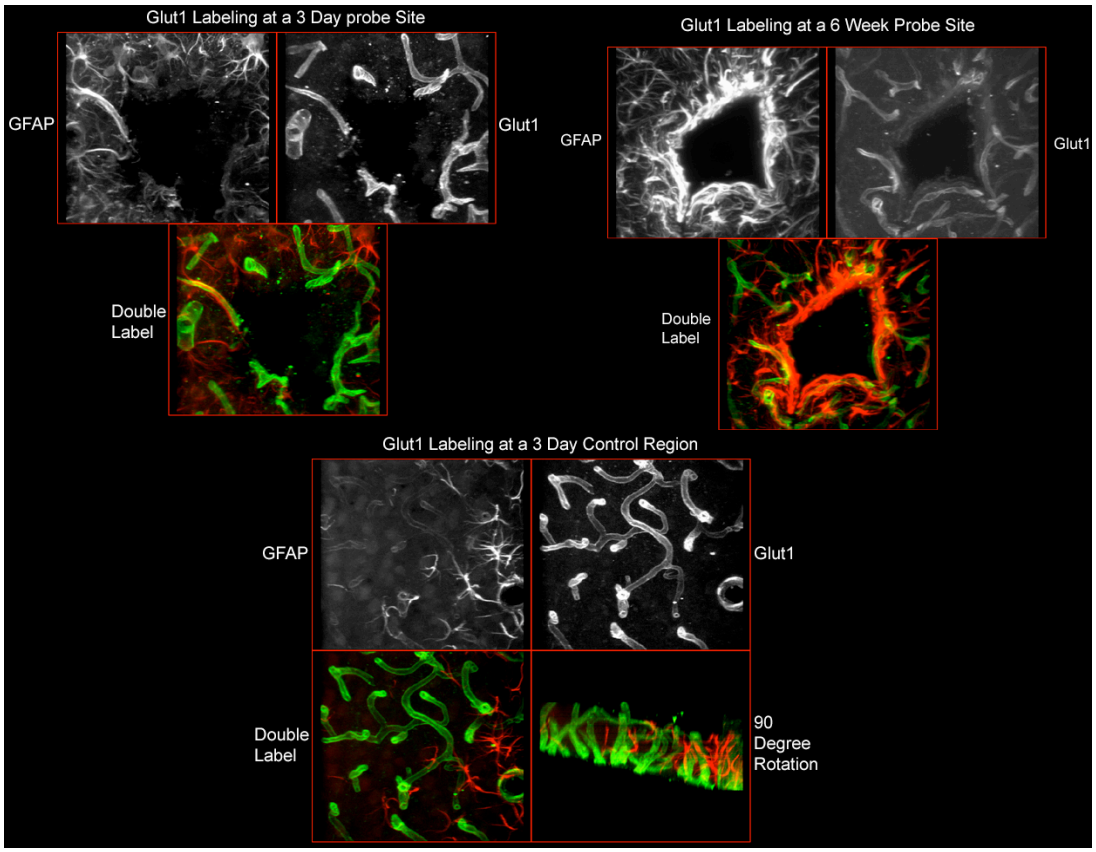

Figure 2.5. Immune response to implanted prosthetics
Immunohistochemical staining shows the brain response. GFAP (red) and Glut1 (green) show structure of surrounding tissue at 3 days (a), 6 weeks (b) and in a control region at 3 days (c). Figure adapted from [73].

At early times post surgery, all insertion sites were characterized by non-uniform regions of increased diffuse fluorescence in a region 100-200 mm immediately around the device insertion sites (Figure 2.5a, GFAP, red). At 1 week, all insertion sites showed an increase in number, size, and fluorescent intensity of GFAP-positive cells. By 2 weeks, the intensity and number of GFAP-positive cells had

increased. At this time the GFAP-positive cells began to become aligned. At 4 weeks, a clear sheath of GFAP-positive astrocytes was observed. The thickness of the sheath at this time varied between 50-100 :m around the perimeter of the insertion site. This compact sheath consists of a mesh of intertwined GFAP-positive processes. By 6 weeks, the sheath was thinner and more compact with fewer cells observed at greater distances from the insertion sites (Figure 2.5b, GFAP, red). The cell and sheath morphologies were similar for all animals. At 12 weeks, GFAP-positive reactivity surrounding the device sites was maintained and similar to that observed at 6 weeks.

2.2.2 *Changes in vasculature post-insertion*

Antibodies to glucose transporter-1 (GLUT-1) were used to describe the brain vasculature. Through-focus projections created from three-dimensional data sets provide adequate sampling of brain tissue in a single image to describe the morphology of entire cells and components of the microvasculature. GLUT-1 immunohistochemistry clearly demonstrated that device insertion causes damage to the microvasculature and some larger blood vessels. During the first week post insertion a series of transient changes are observed in GFAP signals, as described in the above section. We hypothesize that these may be initiated in part by disruption of the blood-brain-barrier and initiation of inflammatory repair responses. Analysis of the microvasculature indicates that angiogenesis occurs with new blood vessels encircling the inserted devices. Some of these blood vessels are imbedded in the narrow band of reactive cells characteristic of the sustained reactive response observed six weeks after device insertion. These data demonstrate that because of the density of the brain microvasculature, insertion of even the smallest devices will disrupt the blood-brain-barrier and initiation of events leading to early reactive responses. We will interpret

these data in terms of a hypothesized biological response in the summary of this chapter.

2.3 Addition of fluid channels for drug delivery

Clearly very complicated, multi-modal mechanisms are underlying the neural response to foreign implants. The transduction mechanisms alerting cells to the presence of the device undoubtedly include biochemical and mechanical pathways. Alleviating the response with surface coatings or by changing the mechanical properties of the device may have an effect, but in addition an active role can be played by the device if it can deliver drugs. We have found that peripheral injection of drugs such as Dexamethasone can reduce immunoreactivity at the insertion site [92]. The incorporation of fluidic microchannels on probe devices would permit the delivery of drugs directly to the insertion site. This localized injection promises to alleviate harmful side effects that peripheral injection causes, especially when large doses are required to ensure that sufficient quantities of the drug penetrate the blood-brain barrier. It also provides a means to deliver drugs which would otherwise be actively eliminated by the barrier. This dynamic adjustment of the local chemical environment will give experimenters a new tool for investigating the biochemical processes underlying the inflammatory response. We now discuss requirements for the microfluidic delivery system, and some important calculations for the performance of the microfluidic channels.

2.3.1 *Flow calculations and design*

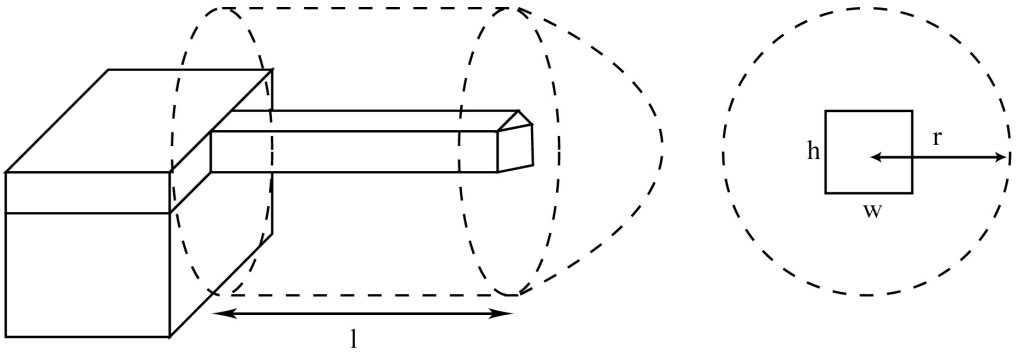

Figure 2.6. Volume of tissue involved in the reactive response
An estimate of the volume of tissue involved in the reactive response. A cylindrical volume about the shank with a hemispherical cap is taken as the reactive region.

First, a rough estimate of the required dose and corresponding flow rate is required. The volume of reactive area of the long term response is taken to be a cylinder of approximately 150 micron radius about the center of the probe shank, estimated from images such as Figure 2.6. If we model the probe as seen in Figure 2.6, we have a volume

$$V = \left(\pi r^2 - wh\right)l + \frac{2}{3}\pi r^3$$

where r = radius, w = width, and h = height. For a reactive response extending 150 microns in radius, a probe of width and height 100 microns, and a 2 mm long shank, we have

$$V = 130nL$$

Modulations in biological response are readily achieved with micromolar concentrations. For sustained release into this limited volume, then, picoliter per second delivery rates might suffice. However, to ensure that flow is laminar even for larger flow rates that could be used during transient injection, we take a 100 pL/s as an upper bound on the flow rate. In experiments by other investigators [44], this volume

of neuromodulator was injected acutely and was found to elicit an immediate change in neural firing.

The fabrication methods readily available for fabrication of fluidic probes place limits on the geometry of fluid channels that can be incorporated on the device. In general, channels can be most easily fabricated with rectangular cross-section, and having a much larger width than height (~ 20:1). For the sacrificial layer techniques used in this work, the channels were approximately 20 microns wide, and 1 micron tall. Outlet ports for channels fabricated using these techniques can either be on the top surface of the channel, or a cut through the channel, with an opening the size of the channel cross-section. To calculate the properties of flow in our channels, we model our channel as shown in Figure 2.7. The analysis follows that of Gravesen, with additional contributions from Prof. R. V. E. Lovelace [93].

The first quantity of interest for describing our fluid flow is the Reynold's number, a measure of flow turbulence. The Reynold's number is given by

$$\mathrm{Re} = \frac{UD_h\rho}{\mu}$$

where U is the flow velocity, D_h is the hydraulic diameter, ρ is the fluid density, and μ is the fluid dynamic viscosity. If the channel cross sectional area is given by A, we take the hydraulic diameter to be

$$D_h = \frac{4A}{wettedperimeter} \cong 5\mu m$$

for channels that are 3 μm tall and 20 μm wide. The threshold Reynold's number (above which the flow is considered turbulent) depends on the ratio of channel length to hydraulic diameter. The channels on our devices are typically several hundred microns long, making $L/D_h \sim 100$, in which case the threshold Reynold's number is taken to be ~ 2300. Since our outlet area is approximately 25 μm^2, and our upper

bound on volume flow rate is on the order of 100 pL/s, our flow velocity will be given by U = Q/A ≅ 4 μm/s. Given these parameters, we calculate a Reynold's number of 2 x 10^{-5}, well below the threshold. This is the normal case for microfluidic channels, where the small hydraulic diameter is a governing factor in forcing the flow to be laminar for modest flow rates. We have the additional requirement of small volume flow rates, forcing our Re even further below threshold.

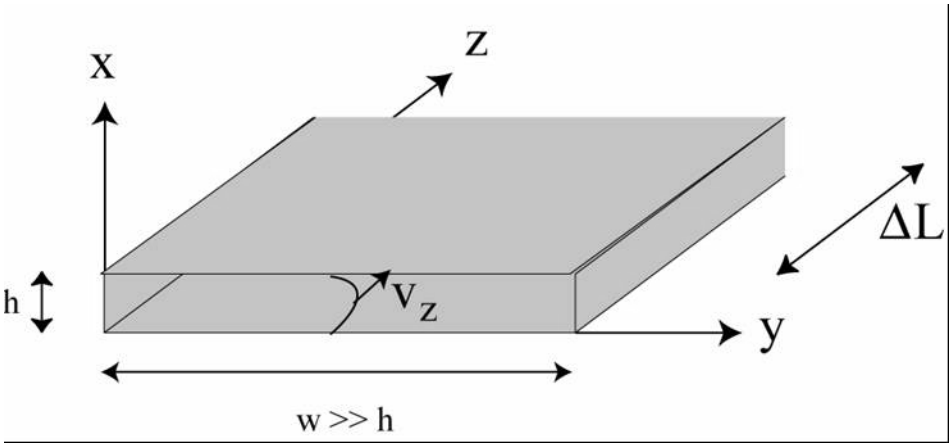

Figure 2.7. Model of fluid flow in microfabricated channels.
Constraints of microfabrication result in channels of much greater width than height. Viscous losses in the narrow dimension dominate, and the velocity profile is taken to be parabolic in the vertical dimension.

Knowing that the flow in our channels is laminar, we would like to calculate the hydraulic impedance of our channels, and relate applied excess pressure to flow rate. We model our channel as seen in Figure 2.7. If we assume that viscous losses in the narrow (x) dimension dominate, then from Poisieulle theory [94] we deduce a parabolic flow velocity in the z direction. Using the x and y axes described in Figure 2.7, and letting our channel have width w and height h, we describe our velocity profile in the z direction, V_z, as

$$V_z = \frac{x}{h}(1 - \frac{x}{h})K$$

where K is a constant having the dimensions of velocity. If we then apply the Poisieulle equation

$$\eta \nabla^2 V_z = \frac{\partial P}{\partial z}$$

where η denotes viscosity and P pressure, to our velocity profile, we have

$$\eta \frac{2}{h} K = \frac{\Delta P}{\Delta z}.$$

We would like to relate pressure changes over length to volume flow rate, Q. We know that the flow rate for our velocity profile is given by

$$Q = \int_S \vec{v} \bullet d\vec{a} \cong w \int_0^h V_z dx \cong Kw \int_0^h \frac{x}{h}(1 - \frac{x}{h}) dx$$

$$\cong \frac{whK}{6}$$

Eliminating K using the previous two equations gives us our result:

$$Q \approx \frac{wh^3 \Delta P}{12 \eta \Delta L}$$

A very useful analogy can be made between this equation and Ohm's law. For this type of flow, the relationship between pressure, volume flow rate, and hydraulic resistance is analogous to that between voltage, current, and resistance in Ohm's law. Making this analogy, we can relate pressure to flow rate using a "hydraulic Ohm's law", in which V=IR is replaced by $Q = R_h \Delta P$. Applying this to the above equation, for a length of channel ΔL, we deduce the hydraulic impedance for our rectangular channels

$$R_{channel} = \frac{12 \eta \Delta L}{wh^3}$$

We will use this relationship, and hydraulic impedances calculated for other channels, to estimate flow rates in channels of different geometry. Another important geometry for our fabrication is a short cylindrical hole, which will be discussed the following section. A similar analysis to the above, for flow through a hole of radius r, yields a hydraulic impedance of

$$R_{hole} = \frac{8\eta\Delta L}{\pi r^4}$$

2.3.2 *Sacrificial oxide channels*

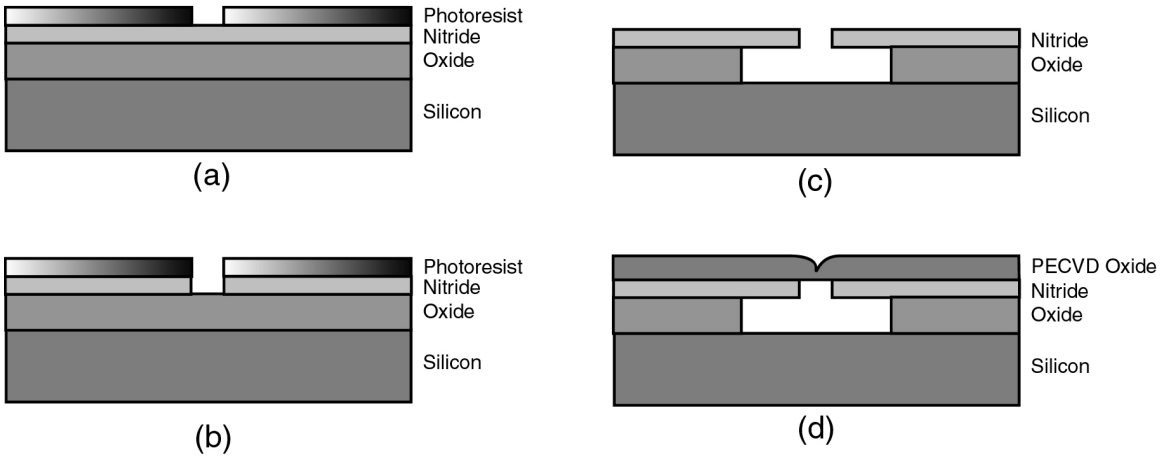

Figure 2.8. Fabrication process for nitride capped microfluidic channels Processing begins with deposition of a sacrificial layer of silicon oxide, 1 to 3 mm thick, following by thin (200 nm) layer of silicon nitride. Small via holes are patterned in photoresist on the nitride (a). An RIE etch of the nitride created small access holes to the oxide (b). Resist is stripped, and in (c) the results of a hydrofluoric acid wet etch is shown. The HF acid etches the oxide at a much greater rate than the nitride, resulting the in etch profile seen in (c). Finally, the holes are closed up with a deposition of PECVD oxide.

The first method used to incorporate microfluidic channels in the probe process utilized an unpatterned sacrificial layer of silicon oxide capped with silicon nitride. This process was developed by members of the Craighead group, and many thanks are due to their pioneering work, especially Drs. S. Turner and M. Foquet. The channels are fabricated before deep etching of the probe structure (Figure 2.8). Processing begins with growth of 1.5 μm of thermal oxide on the SOI wafer. A thin layer of low pressure chemical vapor deposited (LPCVD) Silicon nitride, approximately 200 nm thick, is then grown on the oxide. Small via holes are then etched into the nitride layer, using a photoresist mask and a CF_4 plasma RIE. The holes serves as ports for a hydrofluoric (HF) acid wet etch to access the oxide layer, and isotropically etch it

away. By stringing together via holes at a reasonable distance (~ 10 μm), the etch from neighboring via holes joins up, and a contiguous channel is formed (Figure 2.9). Once these have been formed, the via holes are "plugged up" with either a deposition of plasma enhanced chemical vapor deposition (PECVD) oxide, or by spinning over them with a polymer, such as polyimide. The holes used for probe devices were typically 2 μm in diameter (Figure 2.10). After deposition of 3 microns of PECVD oxide, the holes were closed to between 200 – 500 nm. Even this thick layer of PECVD oxide, due to the anisotropic nature of it's growth, did not completely fill the holes, and either a thermal (conformal) growth of oxide, or a thick spun-on polymer coating would be required. Once the channels have been fabricated and sealed, thick resist can be spun on the surface, and the deep etching of the bulk probe structure proceeds.

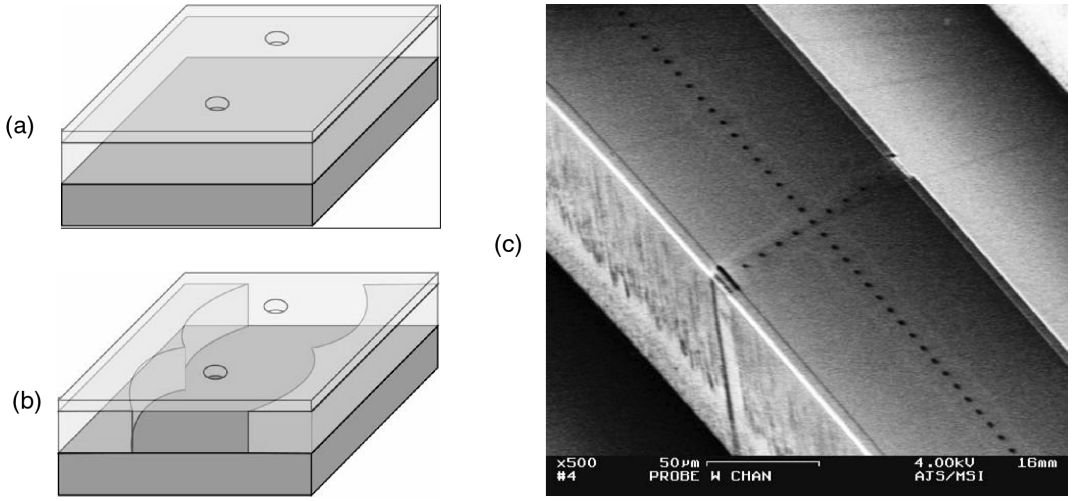

Figure 2.9. 3D Schematic and SEM of nitride capped channels
Holes are etched in the capping nitride layer, exposing the oxide layer (a). (b) An HF wet etch selectively and isotropically etches the oxide layer. Nearby holes create contiguous channels. (c) SEM of nitride channels on a probe shank, which has been etched down to the BOX layer of an SOI substrate.

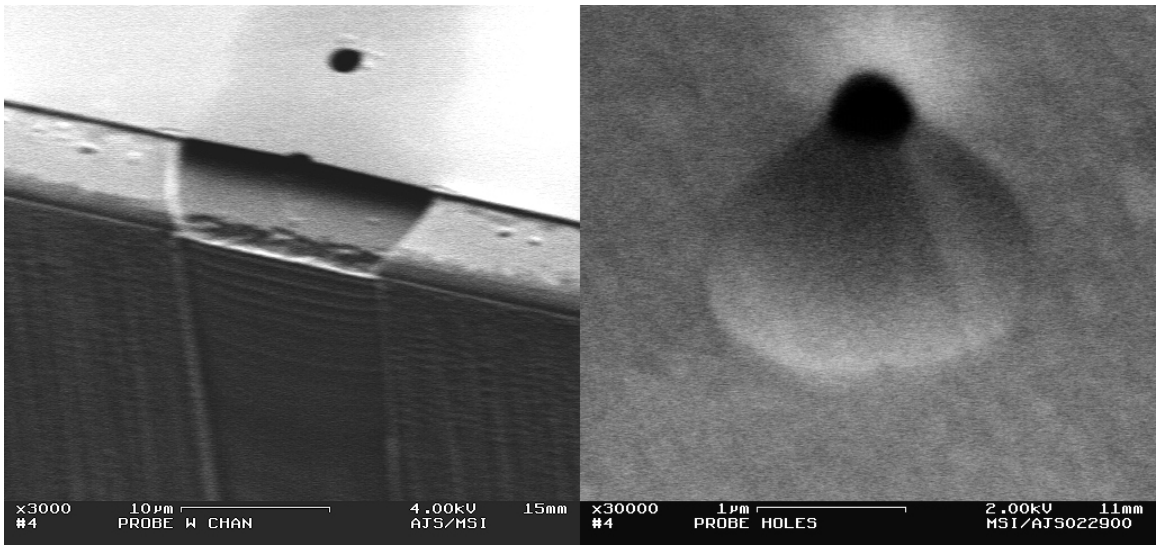

Figure 2.10. Completed channel and sealing of holes with PECVD oxide
Channel created with nitride capping layer, before deposition of PECVD oxide (left), and closeup of via hole after deposition of 3 μm of PECVD oxide. The hole diameter is approximately 200 nm.

This mechanism can be costly to fabricate using contact masks, as the method requires access holes to be spaced close enough that the HF etch joins neighboring holes together, creating a channel. Typically this means having holes spaced roughly every ten microns. Creating a mask with this many holes can be troublesome, requiring large numbers of flashes. However, because the via holes are spaced along the entire channel, channels of arbitrary length can be created. Sacrifical layer techniques that have vias only at the end points of the channel are restricted in length by the diffusion of etch solution into the channel to clear away the sacrificial layer.

In order to calculate the excess pressure required to inject fluid through our multi-port channel, we turn to the model in Figure 2.11. We calculate the hydraulic impedance of the shown resistor network, and then solve for total volume flow rate as a function of excess pressure at the channel entrance. From this calculation, we expect delivery at a reasonable upper limit, 0.25 μL / hour, with an excess pressure of 15 mbar.

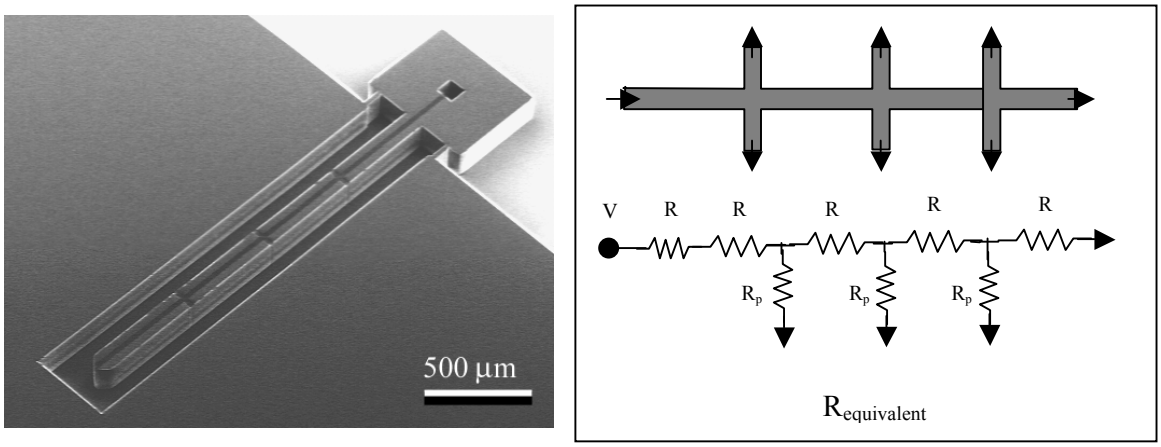

Figure 2.11. Channel structure and equivalent resistor model
Probe having nitride capped channels (left). The channel has side outlet ports at three positions along the shank, as well as at the tip, and a 100 µm cubed test reservoir built into the tab section. The resistor network at right models the hydraulics of the channel geometry, and is used to calculate flow rate for a given excess pressure at the channel input.

2.3.3 *Sprinkler head probe design*

For drug delivery at discrete points along the side, or at the end of the probe, the type of outlets formed in the process above are adequate. However, if a more uniform distribution of released agent across the shank is desired, the via holes present an interesting alternative. By removing the side and end outlet ports, and leaving the channel enclosed, we have a geometry in which the only release areas for the drug is through the via holes. In this configuration, demonstrated in Figure 2.12, we have a "sprinkler head" design, with many small holes along the channel. This design has the advantage that it is a by-product of fabrication process, and that it may produce a more even distribution of drug release.

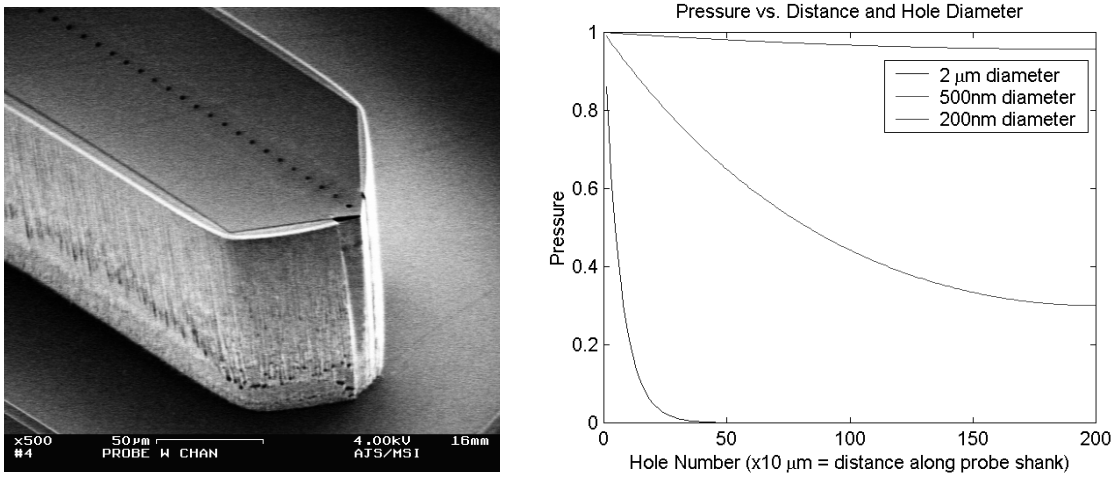

Figure 2.12. Drug delivery using "sprinkler head" design
Probe having unclosed via holes. Assuming the device was modified to remove the side and tip outlet ports, leaving only the via holes in the channel roof, we calculate the pressure drop along the channel as a function of via hole diameter. For the unsealed holes of 2 mm diameter, pressure is completely dropped after ~ 30 holes (300 μm), while for 200 nm holes, the pressure has only dropped to 95% of the input pressure at the end of the probe (2 mm).

An important calculation, then, is the pressure drop as a function of position along the channel. If the via holes in the channel top are too large, all of the excess pressure will be lost at the beginning of the shank, and the remote end of the probe will be inadequately supplied. Narrowing the hole creates a more even pressure profile. In order to calculate this pressure, we use our hydraulic impedances for a rectangular channel and a hole in the following circuit model. Referring to Figure 2.13, we let V_1 be the excess pressure at the input, R_L is the rectangular channel impedance found above, R_H is the via hole impedance, also listed in the calculations of section 2.3.2, and the pressure at each of the 200 holes spanning the 2 mm probe shank is denoted by the voltages $V_2 \ldots V_{201}$. Each R_H leads to the open brain tissue, and is considered a ground. This model comprises a system of 200 equations, found using Kirkoff's law at each node, and 200 unknowns, the pressures $V_2 \ldots V_{201}$.

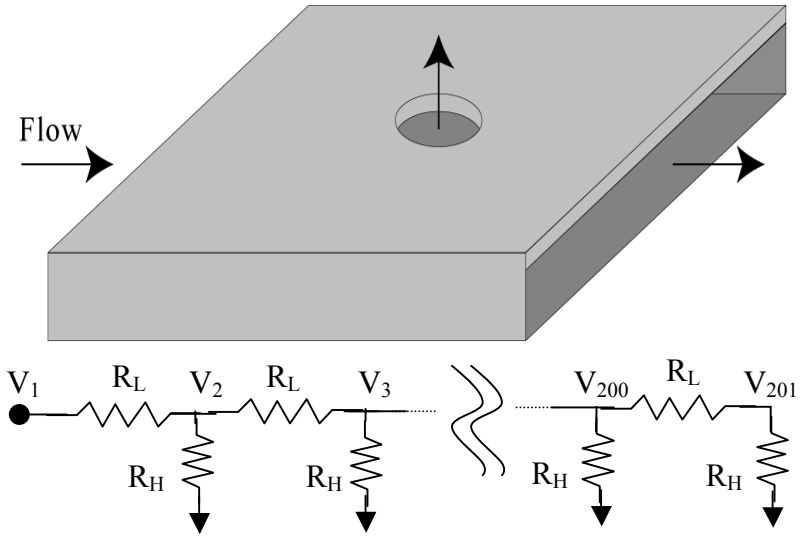

Figure 2.13. Modeling fluid flow from via holes
Schematic of flow through via hole in top of channel (above), and equivalent hydraulic impedance circuit (below).

This system of equations can easily be put in matrix form, and solved numerically. The pressure profile as a function of hole number, and hence distance along the probe, is shown in Figure 2.13. What we find is that for unclosed holes of 200 μm diameter, nearly all of the pressure is dropped across the first 30 holes, or 300 microns of the probe shank. For holes narrowed to 200 nm, we find that the pressure at the end of the shank is 95% of that at the input. In this configuration, the difference in flow rates of fluid out of the holes across the probe shank would be negligible, whereas the larger hole diameter would result in saturation near the probe base and starvation and the probe tip. Repeating our calculation of pressure required to produce a volume flow rate of 0.25 μL / hour, we find that for the small diameter holes we require 150 mbar.

2.3.4 *Channel integrity verification*

Although optical verification of the wet etch having completed was possible at the CNF, confirmation that the channels were indeed continuous and open was required. To do so, a micropipette was filled with Rhodamine fluorescent dye, and

used to place fluid at the entrance to the probe reservoir. Capillary forces at the entrance to these fluid channels are immense, and as such, the main constraint of the experiment was to supply fluid to the channel entrance without spilling it onto the probe shank. Figure 2.14 shows the result of the experiment.

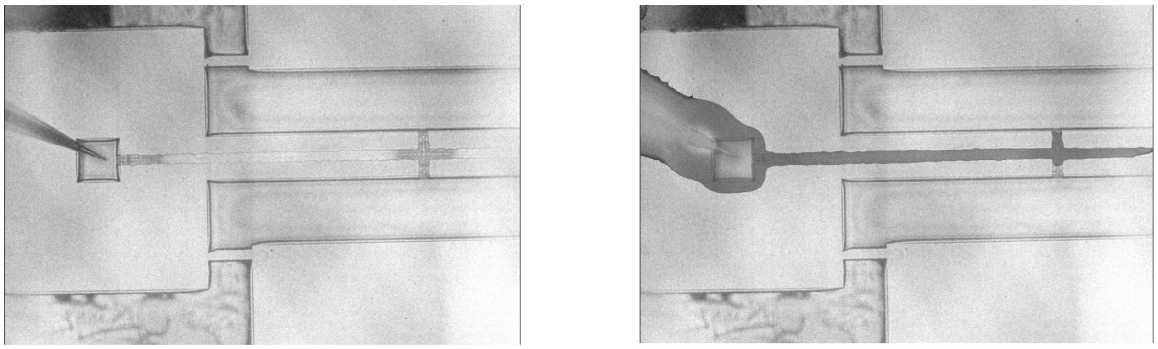

a) b)

Figure 2.14. Fluid flow in probe channels
Overlay of bright field and fluorescent images during test of microchannels. Bright field image of probe and micropipette in reservoir (a). In (b), the tip of the pipette was broken against the edge of the reservoir, and the released dye is seen flowing through the channel. The dye was in ethanol solution, and a meniscus was seen to evaporate from the channel after the experiment.

While this test simply verifies that the channels are structurally sound and are contiguous to fluid flow, more recently the channels have been tested *in vivo*. In Chapter 5 we present some initial results of delivering the neuronal marker Transferrin to the rat cortex through fluidic channels on a probe.

2.3.5 *Polysilicon channels*

Two major limitations of the nitride capped channel fabrication are the need to fabricate large numbers of holes, and the difficulty in completely sealing them. One solution to this problem is to use a patterned sacrificial oxide layer, as opposed to a complete thin film. In addition, moving to a polysilicon capping layer preserves the selectivity of the wet etch, but provides the option of a thicker capping layer. The

fabrication process for probes with polysilicon channels is shown in Figure 1.15. Two other changes in the probe fabrication process are notable.

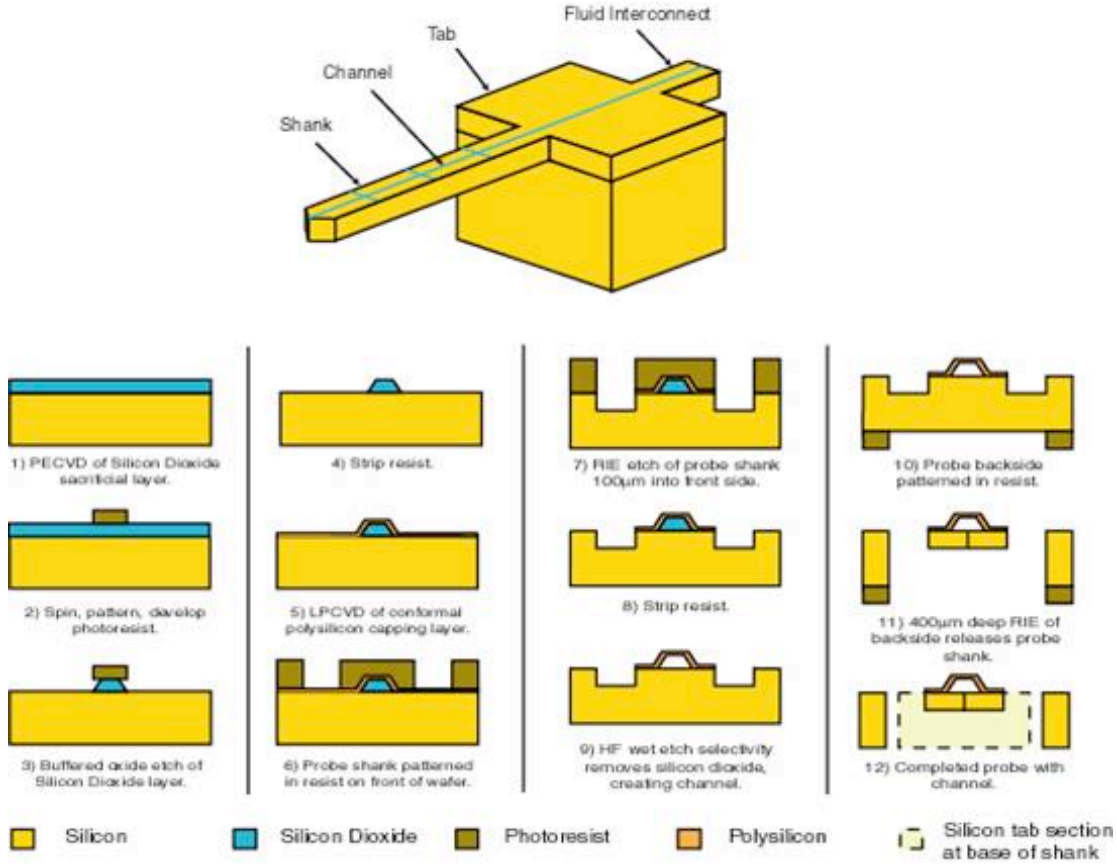

Figure 2.15. Fabrication of probes with polysilicon channels and fluid interconnects
Polysilicon capped channel fabrication process, and interconnection scheme.

The probe geometry has been updated to include a protrusion from the rear of the probe tab. This protrusion is the result of experimentation with interfacing to the probe channels. The interface between the fluid channels and an external supply is one of the great challenges of chronically implanted devices such as these. The need to be continually connected to, or periodically connected to, the fluid channel is a difficult problem. In addition, the bare substrate for probe fabrication is now bare silicon wafers, not SOI wafers. Although the buried oxide layer in SOI wafers provided a

hard stop for the deep etch, the expense of and difficulty obtaining SOI wafers with 100 micron thick device layers forced the exploration of new fabrication methods. It was found that with periodic measurement of etch depth, and careful characterization of etch rate, probes of thickness 100 μm ± 20 micron could be created simply using two deep etches without the oxide hard stop. This is illustrated in Figure 2.15, where the buried oxide layer is missing. Probes with polysilicon channels fabricated in this manner are seen in Figure 2.16.

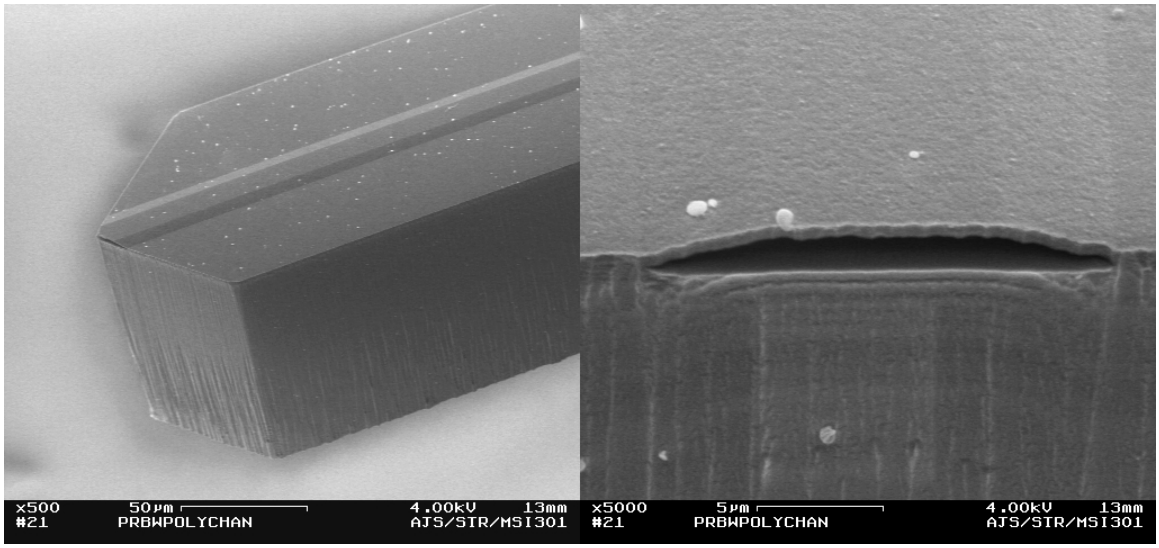

Figure 2.16. Probes with polysilicon channels
Tip of shank (left) and side port opening (right) of polysilicon microfluidic channels on probes.

2.4 Summary of Neuroprosthetic Studies

We have developed fabrication processes for probes of varied shank geometry, along with a method of aligned, controlled insertion for these devices. Initial probes were fabricated using a two step deep etching process, where the probe shank was etched in the device layer of an SOI wafer, and a larger tab section at the base of the shank was provided by the thicker handle layer of the wafer. This cubic tab section

was gripped on three sides, providing alignment of the probe axis with a microprocessor controlled insertion device.

Bare silicon probes of varying shank geometry were fabricated using this process and inserted in the brain of rats. The shank width was varied photolithographically, and the shank height was varied by using SOI wafers of various device layer thickness. Similar reactive responses were observed following insertion of all devices; however, the volume of tissue involved at early times (~one week) was proportional to the cross-sectional area of the devices. Responses observed after 4 weeks were similar for all devices. Thus, the continued presence of devices promotes formation of a sheath composed partly of reactive astrocytes and microglia. Both GFAP-positive and -negative cells were adherent to all devices. These data indicate that device insertion promotes two responses – an early response that is proportional to device size and a prolonged response that is independent of device size, geometry, and surface roughness (Figure 2.17). The early response may be associated with the amount of damage generated during insertion. The prolonged response may be due to tissue-device interactions.

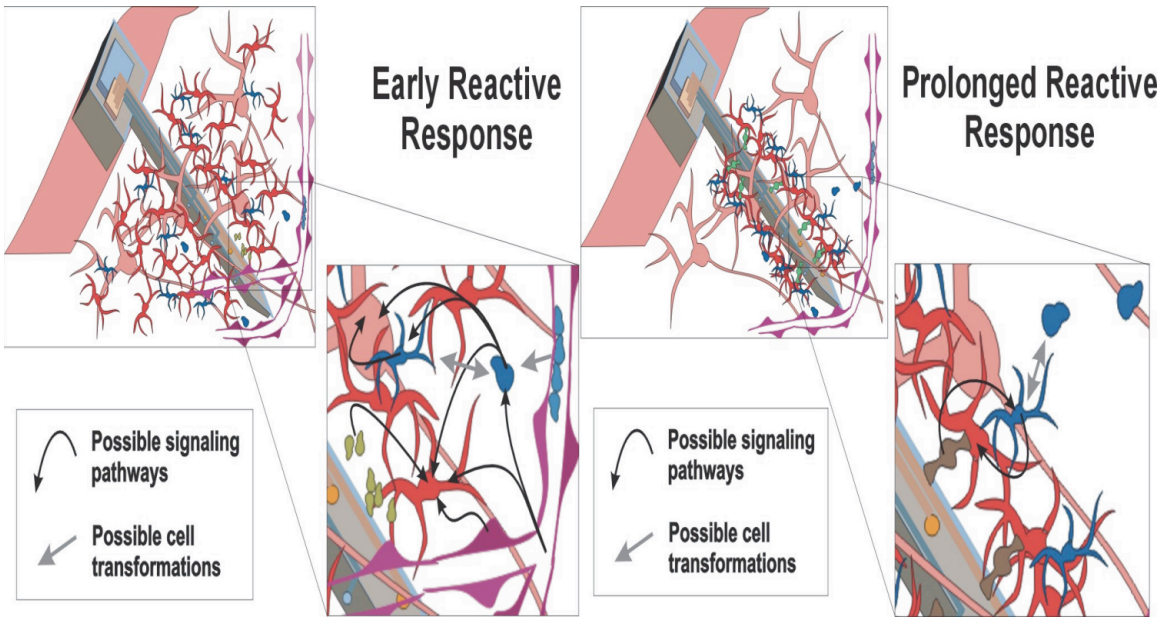

Figure 2.17. Hypothesized two-phased brain immune response
Probe-tissue reactions are depicted schematically during the early (left) and late (right) reactive responses. Figure adapted from [43].

In order to find methods to further elucidate and eventually alleviate this encapsulating immune response, we tested various methods for fabricating probes with fluid channels for drug delivery. We performed calculations to show that the volume of tissue that needs to be affected is approximately 130nL, and that a small excess pressure (10s or 100s of millibar) is enough to deliver adequate doses of biologically active molecules to this volume.

We fabricated probes with fluid channels by using a sacrificial layer of silicon oxide underneath silicon nitride, or by using a patterned sacrificial layer of silicon oxide underneath polysilicon. The outlets for the fluid were either at multiple points along the shank, or a series of openings in the ceiling of the fluid channel. We verified the integrity of the fluid channels by observation of the capillary induction of fluorescent dye into the channels. The calculations of fluid flow rate dependence on

channel geometry have been verified using a more detailed analytical model, and the fluid channels have been used to modify the biochemical environment in animals [95].

CHAPTER 3: SUBSTRATE ELECTRODE ARRAYS FOR PATTERNED NEURONAL CELL CULTURE

Neuronal cell networks have been reconstructed on planar microelectrode arrays (MEAs) from dissociated primary hippocampal pyramidal neurons. Microcontact printing (μCP) and a photoresist liftoff method were used to selectively localize poly-L-lysine (PLL) to specific locations on the surface of the array in order to organize cells into grid-shaped networks and to localize cells and cell networks near electrode tips. Several different network architectures were successful: less structured, dense networks consisting of 10-15 μm wide grids of cells produced large amounts of spontaneous activity, while more structured, less dense networks consisting of cell bodies confined to 15 μm wide nodes with intervening 2-3 μm wide lanes for process outgrowth produced less spontaneous activity. Multiple simultaneous recordings were performed to determine the spatial location of electrical activity, and single units were successfully isolated. This combination of techniques will enable multi-site recordings from single units in low-density cell cultures, allowing for the monitoring of activity throughout development.

3.1 Background, History, and Limitations of Current Methods

Whereas microfabricated devices used to record from the mammalian brain have the advantage of recording from structures in their natural morphology, the huge numbers and spatial distribution of the neurons, coupled with the immune encapsulation problem, makes collecting data very difficult. An alternate approach is to extract the same neurons at an embryonic stage, and cultivate smaller networks of them *in vitro*. This greatly simplifies the networks and morphology, reducing it to a planar geometry. Microfabrication techniques can also provide a solution to the

neural-electronic interface, in the form of substrate microelectrode arrays (MEAs). MEAs have been used for more than two decades to stimulate and record extracellular electrical activity from electrogenic cell networks [10, 96-100] and hippocampal slices [101, 102]. Although extracellular recordings suffer from lower signal-to-noise ratios (SNRs), the reduced invasiveness (which allows for recordings over weeks and months) and multielectrode capabilities (>100 separate, simultaneous channels) are very advantageous for network studies [103]. Early work in this area primarily used randomly structured cell networks, but many labs have moved towards directed organization of cell networks into specific architectures. Research in chemical patterning for cell cultures indicated that chemical cues can provide a strong influence on cell attachment and outgrowth [104]. In addition, the use of chemical cues also procures the advantage of directly influencing cell functionality. Extracellular matrix (ECM) proteins are involved in a wide range of cell functions. Thus, selective localization of relevant biomolecules on surfaces provides the opportunity for controlling an array of cellular processes (including regulation of gene transcription) which in turn will affect network structure and functionality.

Patterning surfaces with chemical cues for organizing cell networks has been accomplished for years with non-biological self-assembled monolayers (SAMs) and biological proteins and peptides [105-109]. Microcontact printing (μCP) is a soft lithography technique that can localize patterns of biologically active proteins onto surfaces very quickly (1 second) [110, 111]. μCP is ideally suited for placing patterns of proteins and polypeptides onto electronic devices such as planar microelectrode arrays [112-114]. Proteins such as laminin and cell-attachment polymers such as poly-L-lysine (PLL) and poly(ethyleneimine) (PEI) have been patterned on surfaces [114-117].

3.2 Materials and Methods

3.2.1 *Microelectrode Array Fabrication*

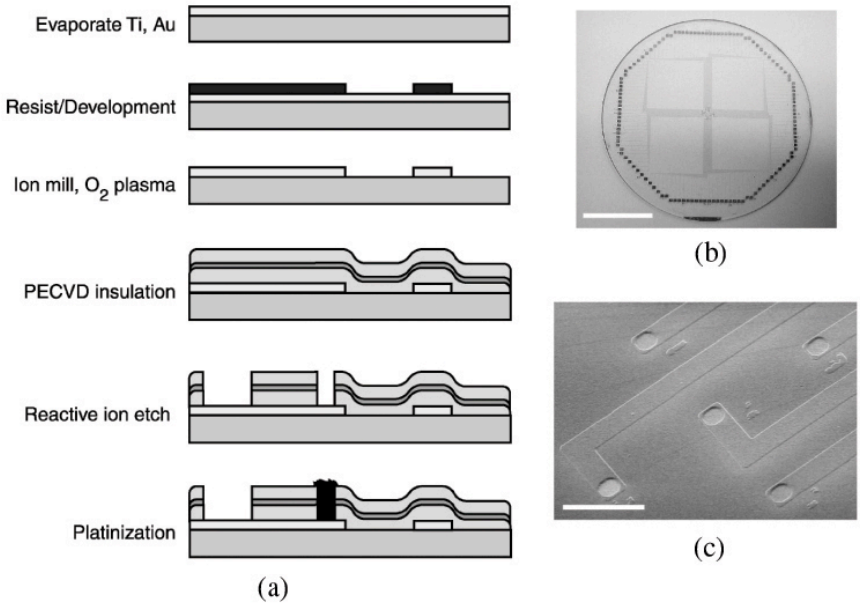

Figure 3.1 Substrate multielectrode fabrication process.
(a) Microelectrode array fabrication process and (b) completed device. Scale bar = 25 mm. (c) Scanning electron micrograph of a set of microelectrodes. Scale bar = 25 μm. Figure taken from James et. al. [3].

Fused silica wafers were obtained from CVD Electronics and subjected to a full RCA clean consisting of an ammonium hydroxide/hydrogen peroxide immersion to remove organic particulates, and a hydrochloric acid/hydrogen peroxide immersion to remove metal particulates. Wafers were rinsed thoroughly with filtered water in between steps and with a final rinse until the water resistivity reached 16 MΩ-cm^2. Wafers were spun dry at an elevated temperature. An adhesion layer of titanium (5-10 nm) and then gold (250-500 nm) were evaporated onto the cleaned substrates. Photoresist was spun and exposed with a 420nm UV contact aligner and developed, leaving a mask to define the gold traces. An argon ion mill was used to remove gold

and titanium from the unmasked regions of the wafer. Substrates were subjected to fifteen seconds of an oxygen plasma to help facilitate the removal of the resist, and then sonicated in acetone for 15 minutes. After a final rinse with isopropanol and deionized water, substrates were subjected to a one-minute O_2 plasma treatment to prepare the surface for deposition of the insulation. Gold traces on our substrates were insulated with ~ 1000 nm of a PECVD oxide/nitride/oxide triple stack [118] (Figure 3.1). This insulation suffered less delamination than PECVD nitride alone due to complementary compressive and tensile stresses in the films canceling out. Contacts to the gold wires were made using a photoresist mask and reactive ion etches in CF_4 for nitride and CHF_3/O_2 for oxide. The resist mask was removed with a fifteen second oxygen plasma and a subsequent incubation in acetone for thirty minutes.

3.2.2 *Microelectrode Characterization*

Microelectrodes were platinized to increase the signal-to-noise ratio of our recordings (Figure 3.2). Commercially available platinization solution was obtained from LabChem Inc (# LC18680-7). The electrodes were held at the cathode and a reference platinum electrode was held in the bulk solution. Electrode arrays were platinized by passing a DC current of 4-5 nA/μm^2 through the electrodes for approximately thirty to ninety seconds [119] (Figure 3.2). The impedance of our microelectrodes, Z_e, was measured over the range of 100 to 5000 Hz with a lock-in amplifier and fit to a power law. The impedance of a metal electrode/electrolyte interface is given by $Z_e \propto f^m$, with typical m values between -0.4 and -0.9 [120].

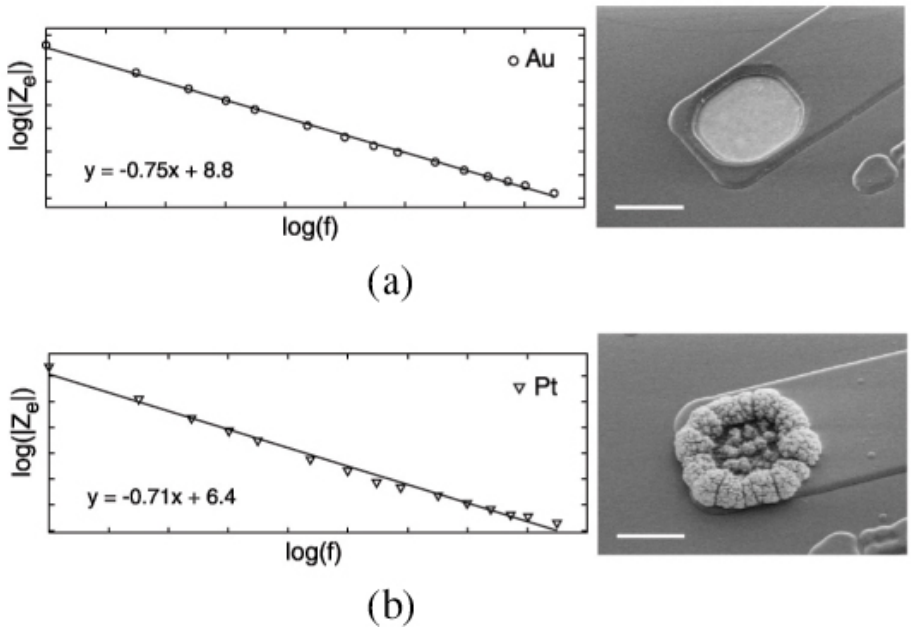

Figure 3.2. Characterization of electrode impedance.
The average impedance magnitudes and linear fits for (a) gold microelectrodes (n =12, r 2 = 0.947) and (b) platinized microelectrodes (n = 9, r 2 = 0.870) as a function of frequency (0.1 – 5 kHz). Images on the right are scanning electron micrographs of (top) a gold recording site and (bottom) a platinized site. Scale bars = 5 mm. Figure taken from James et. al. [3].

The impedance of the microelectrode is important in that it influences the amount of extracellular potential (V_{in}) that reaches the recording apparatus (Figure 3.3), and because the resistive portion of the impedance contributes to the background Johnson noise according to Nyquist's theorem [121]:

$$N_{rms} = \sqrt{4kT\int_{f_1}^{f_2}\left[real(Z_e) + R_{spread}\right]df} \quad \text{with } real(Z_e) = R_0 f^m$$

with the electrode/electrolyte interfacial impedance Z_e, and R_{spread}, a function of solution resistivity and electrode diameter [119]. The real portion of Z_e of the bare gold electrodes was fit using a linear regression with the parameters $R_o = 9.8 \times 10^8$ and m = -0.97 (n=12, $r^2 = 0.61$), while platinized electrodes were fit with parameters

R_o=3.8 x10^5 and m = -0.64 (n=9, r^2 = 0.85). Including an estimated value of R_{spread} of 58 kΩ and 23 kΩ for gold electrodes and platinized electrodes, respectively, yields estimated root-mean-square thermal noise predictions of 7.8 μV and 1.4 μV. After platinization, arrays are subjected to a one minute plasma discharge (Harrick Scientific plasma cleaner/sterilizer) and soaked in ultra-pure Milli-Q water for one to two days with frequent changes.

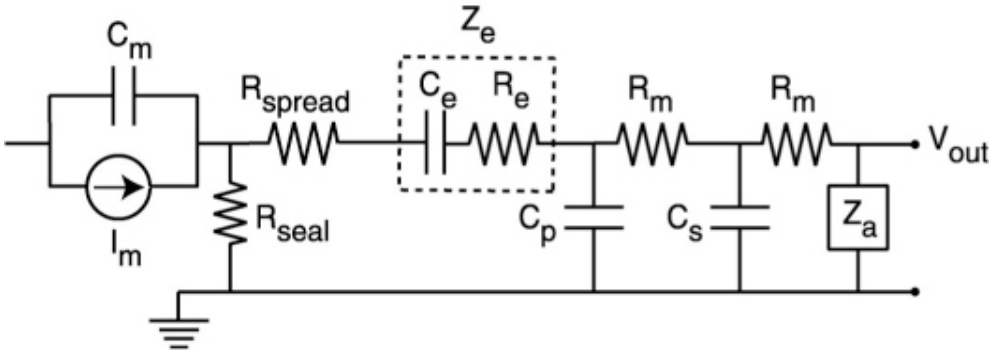

Figure 3.3. Equivalent circuit model of extracellular neural recording
Circuit diagram depicting important parameters for extracellular recording: I_m, membrane current from the cell; C_m, membrane capacitance; R_{spread}, spreading resistance; Z_e, microelectrode impedance; R_m, resistance of microelectrode traces; Z_a, amplifier input impedance; V_{out}, detected signal. Capacitive losses are C_p, through the insulation; C_c, between microelectrode traces; C_s, shunt capacitance in cabling. Figure taken from James et. al. [3].

The primary loss in our setup is the capacitive coupling, C_p, from electrode traces through the insulation to the conducting culture medium (Figure 3.3). We measured the capacitive coupling to be ~ 2 pF/mm, with a typical setup consisting of approximately 30 mm of electrode trace coupled to the medium. This measured capacitive coupling yields a through-insulation impedance of at least several MΩs at 1 kHz, while the electrical crosstalk between nearest neighbor electrode traces was measured to be roughly 70 MΩ at 1 kHz. Long-term stability of the insulation in physiological conditions has not been quantified.

3.2.3 *Surface Patterning*

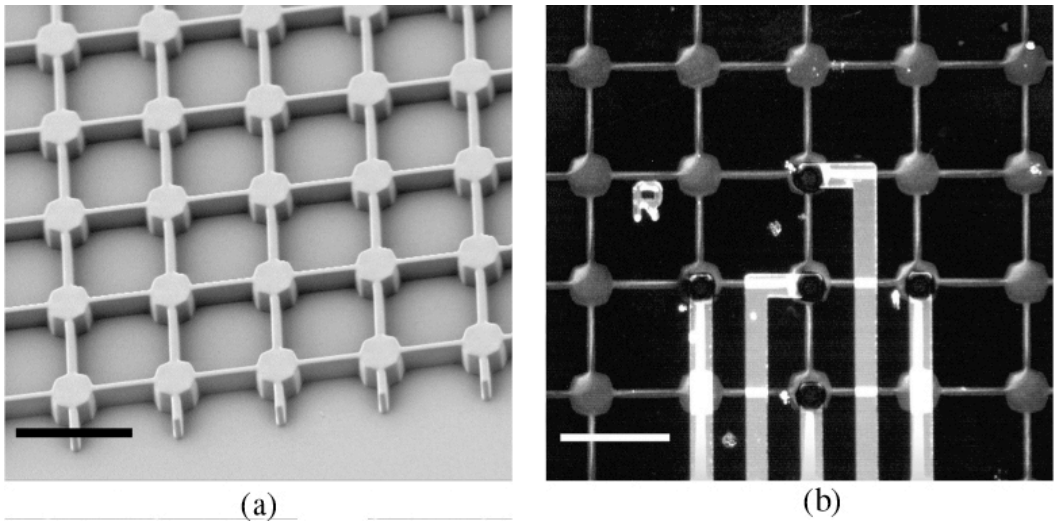

Figure 3.4. Microcontact Printing of Poly-L-Lysine on a multielectrode array. a) SEM of a PDMS stamp and b) the pattern of FITC-labeled PLL produced by aligning the stamp's features to the recording sites. Scale bars = 50 mm. Figure taken from James et. al. [3].

μCP was used to transfer PLL into patterns on electrode arrays. Masters [Figure 3.4] were fabricated as detailed elsewhere [122]. Fluorescein isothiocyanate (FITC) labeled PLL (Sigma P#) was dissolved at 1 mg/ml in borate buffer, filter sterilized through 0.22 μm syringe filters, and applied to plasma-treated PDMS stamps for 10-30 minutes. Stamps were blown dry with a nitrogen stream. The PDMS stamps were cured on optical flats to allow for relatively flat stamps that could be fastened to a microscope stage. Using a custom-made alignment tool [112], PLL coated stamps were aligned to and brought into contact with electrode arrays for 5-10 minutes under a pressure of 100g/cm^2. Stamped electrode arrays were rinsed in buffer and Milli-Q water, and then dried with a dry nitrogen stream. The thickness of PLL transferred to substrates with μCP is ~0.5-0.6 nm as determined by AFM analysis.

3.2.4 *Photolithographic Liftoff Patterning*

Substrates were photolithographically patterned with PLL in a liftoff method similar to that of Lom et. al [107]. Electroplated electrode arrays were coated with HMDS and 1.2 μm of photoresist. Arrays were then exposed with UV through a mask and developed. A one minute oxygen plasma was used to clean the exposed areas of the array to improve the protein adsorption to the surface of the array. The arrays were then incubated in a 1 mg/ml solution of PLL in borate buffer overnight at room temperature. Substrates were then sonicated in acetone for 30 minutes, and a final gentle application of a cotton swab doused with acetone helped to remove remaining photoresist residue that can be visualized in fluorescence. Unfortunately, the platinum black tips of electrodes are removed in the process, increasing the impedance of the electrodes, but cell adherence to the PLL pattern was often compromised when this residue was not removed. Arrays were then rinsed in isopropanol and soaked in Milli-Q water with several changes for 1-3 days to help remove any solvent from the insulation film and the platinum black tips. AFM analysis shows that a layer of ~1.2 nm of PLL adsorbs to the substrate (data not shown).

3.2.5 *Cell Culturing*

Primary cultures of hippocampal neurons were prepared from prenatal Sprague Dawley rats (18 days gestation) using previously described methods [123]. Briefly, embryos were recovered by c-sections under CO_2 anesthesia. Individual neurons were isolated by treating the dissected hippocampi with trypsin and trituration in Hepes-buffered calcium-magnesium free Hank's Balanced Salt solution (pH 7.3). Microelectrode array surfaces were patterned with PLL by stamping or liftoff as described above. A culture chamber was made by drilling a 25mm hole in a 60mm tissue culture dish. Culture chambers were attached to the electrode surface with a

thin layer of PDMS and cured in an oven at 60^{o}C for 15-20 min. The culture chamber was sterilized by an overnight incubation in 0.1% gentamycin in Hank's buffer and rinsed twice with Hank's buffer before plating the cells. The neurons were plated at a density of 1.00–1.50 x 10^5 cells per well, in minimal essential media (MEM) supplemented with 10% horse serum and 0.1% pyruvate. Horse serum containing neuronal plating media was replaced with serum free (N2.1) or neurobasal media at least two hours after the initial plating. Two different methods were used for long-term maintenance of cultures. Co-cultures [123] were created using a coverslip containing an astrocytic monolayer inverted above the neuronal culture in serum free (N2.1) media. In the second method, neuronal plating media was replaced with serum-free neurobasal media (Gibco), supplemented with B27 (Gibco) and 0.5mM L-glutamine (Fluka Biocemika) [124]. Cultures were maintained at 37ºC, 5% CO_2 for more than two weeks with feedings twice a week by replacing half of the media with fresh media.

3.2.6 *Electrophysiology*

A research light microscope with a custom-made resistively heated stage served as the foundation of the recording apparatus. During experiments, the electrode wafer with attached well was removed from incubation, placed in the fitted stage, and connected to the amplifier system for recording. Gravity perfusion of recording media (HEPES, held at 35-37° C) provided gradual replacement of the culture medium and was continued throughout recording. The reference for extracellular recording was a silver/silver chloride reference wire placed in the bath. Careful consideration of grounding, elimination of ground loops and noisy devices yielded acceptable noise levels of about 5-7 μV rms.

The signal from the recording sites was amplified (10k) and band-pass filtered (0.3-5 kHz, 40 dB/decade falloff) using an A & M Systems Model 1800 amplifier. Recording site impedance was confirmed during measurement with a 0.1 μA, 1 kHz sine wave generated by an A & M Systems Model 1700 amplifier. Typical *in vitro* impedances of electrodes ($|Z_e|+ R_{seal} + R_{spread}$) in cell culture were from 0.3-1.0 MΩ. The amplified signal was sent to an oscilloscope and a personal computer for digitization (National Instruments NI-DAQ PCI-MIO 16E, 20kHz), using a custom scripted user interface (Mathworks' MATLAB software). Preliminary images were taken from an inverted microscope with a digital camera to inspect for likely active recording sites. *In vitro* images were taken using immersion objectives on the electrophysiological microscope with a high-sensitivity CCD camera.

We used a combination of manual and K-means clustering on multi-channel waveforms to group spikes into clusters representing putative single units [125]. Spikes were detected offline using a window discriminator algorithm. The multi-channel spike waveforms were extracted, and a principle components analysis was carried out on a concatenation of the waves from each electrode. A scatter-plot of the projection of each concatenated waveform onto the first two principle components was used to identify clusters of similar multi-channel spike shapes. A spike near the center of each cluster was selected, and the K-means clustering algorithm used to cluster the spikes starting with these initial selections. A final manual clustering was used to correct obvious misclassifications and remove outliers.

3.2.7 *Immunocytochemistry*

After electrophysiological recordings, neurons were fixed with 4% paraformaldehyde at 37^{o}C for 10 minutes and processed for immunocytochemistry using standard procedures [126]. Briefly, samples were permeabilized with 0.2%

triton in Hepes Hank's buffer for 10 min at room temperature (RT) and incubated in 6% bovine serum albumin (30 minutes at RT) to block nonspecific staining, and incubated in primary (60 minutes at 37^{o}C) and secondary (40 minutes at 37^{o}C) antibodies in Hank's buffered saline. After final washing, the samples were mounted under a coverslip using mounting media (1:1 Hepes Hanks/glycerol containing n-propyl gallate). All neuronal processes were labeled using a polyclonal antibody against neuron-specific tubulin subunit, β III tubulin(1:10,000) (BabCo/Covance #PRB-435P). Dendrites were labeled using a mouse monoclonal antibody against microtubule associated protein, MAP2 (1:2000) (Sigma #M4403). Secondary antibodies were conjugated to Texas Red (1:200) (Molecular Probes) or Cy5 (1:200) (Jackson ImmunoRes). Fluorescent images were obtained using a Noran confocal scanning laser system on an inverted Olympus microscope. All data are presented as through focus projections.

After culturing, cellular material and debris were removed by incubating the electrode arrays in household bleach for 30 minutes [96] and a subsequent water rinse. If residue proved difficult to remove, a fifteen minute to several hour treatment in Nanostrip (a stabilized formulation of sulfuric acid and hydrogen peroxide) proved successful at removing debris and especially PDMS residue left by petri wells after removal. New culture chambers were applied with each culture.

3.3 Results and Analysis

3.3.1 *Recordings*

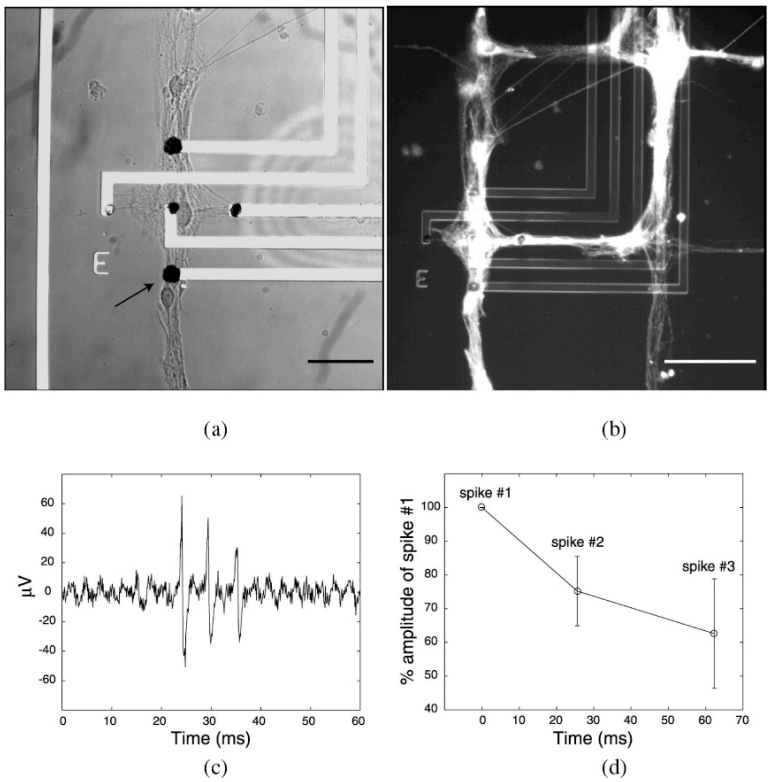

Figure 3.5. Images and spontaneous activity of a cell network on an MEA
(a) Phase contrast image of a cell network on a MEA. Scale bar = 50 mm. (b) Fluorescence image of the same network stained with Rhodamine 123. Grid dimensions are 20 mm wide PLL lines and 180 mm spaces. Scale bar = 50 mm. (c) Spontaneous activity recorded from the microelectrode indicated by the arrow in (a). (d) Plot of the average attenuation of spike amplitude during 14 spontaneous spike bursts. Figure taken from James et. al. [3].

Spontaneous and KCl evoked activity were recorded from the MEAs (Figure 3.5). Extracellular spikes were typically between 50-250 mV peak-to-peak with a background noise around 10-20 mV peak-to-peak, stemming from Johnson noise, amplifier noise, and biological noise in the form of membrane currents. Our constructed networks often demonstrated several episodes of activity-dependent action potential attenuation during bursts of activity [127]. In this phenomenon, action

potentials in cell bodies and axons of neurons maintain consistent amplitude during spike-trains, while marked attenuation progressively occurs in dendrites. Different distributions of ion channels within cell compartments and frequency- and voltage-dependent inactivation of sodium channels have been described as the main culprits [128, 129]. This attenuation has been observed in many spike trains from our cell networks, indicating that the currents responsible for the extracellular potentials contain substantial dendritic contributions (Figure 3.5c,d). For the network shown in Figure 3.5, there were 14 instances of spike bursts during a one minute recording session. The average amplitude attenuation in spike trains was 25 ± 10 % from the first spike to the second spike, and 38 ± 16 % from the first spike to the third spike. The time interval between the first and second spike (25 ± 25 ms) and the first and third spike (62 ± 63 ms) was averaged from the 14 cases. As shown in several circuit models [130, 131], changes in ion channel density will affect the extracellular potential. So we simulated a decrease in sodium ion channel density (gNa = mNa gNa,0) and the results are shown in Fig. 3.6. The initial sodium ion channel concentration (mNa = 1) produces a 160 mV peak-to-peak extracellular spike. When we reduce the density of sodium ion channels to 80% and 70%, we find that the extracellular spike that is 80% and 64% of the initial spike amplitude. The effect is nonlinear in that at 60% of the original sodium channel density, the extracellular potential is nearly abolished (0.78%) for this particular simulation. As such, the activity-dependent depletion of sodium channels may contribute to the bursting behavior we detected in several experiments. In addition, the time delay between the stimulation current and the onset of the extracellular potential increases as the density of sodium channels is reduced.

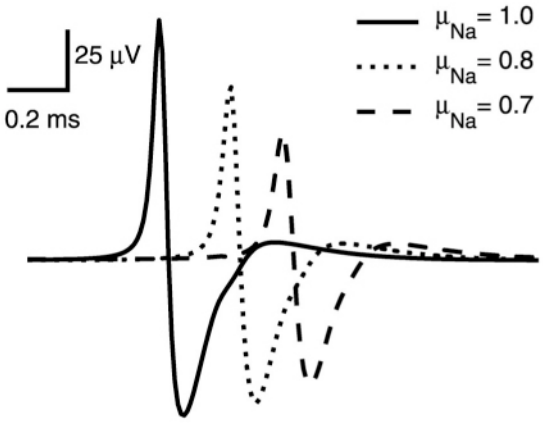

Figure 3.6. Simulation of spike amplitude changes with different densities of sodium channels.
Simulations of a membrane with different densities of voltage-gated sodium channels. The onset of the extracellular spike is delayed in time as mNa is reduced. Figure taken from James et. al. [3].

A five channel recording of elicited activity (addition of KCl to culture medium) from patterned cells at 16 days *in vitro* (DIV) is seen in Figure 7. The PLL pattern in this experiment consisted of a photolithographically defined grid of 25 mm wide lines spaced by 100 mm. Cell bodies attached to and remained on the pattern, while neurites were less confined and grew off the pattern after several days. The clustering results are presented in Figure 8. Three distinguishable types of spikes are readily apparent, and the cluster firing times are depicted at the bottom of Fig. 8. The background noise (N_{rms}) on microelectrodes J2, J4, and J5 was 7.2, 5.5 and 4.6 mV, respectively. The infrequency of spikes led to very few cases of signal overlap, simplifying unit identification for comparison with imaging. In addition, the spacing of microelectrodes and the action potential propagation are such that spikes from a single neuron seldom appear on more than three recording sites. In certain instances, spikes were detected on more than one microelectrode. It's possible that these are cases of multiple cells with common input that fire coincidentally, but from visual

inspection we attribute this particular coincident activity to single cells coupled to multiple microelectrodes at different locations.

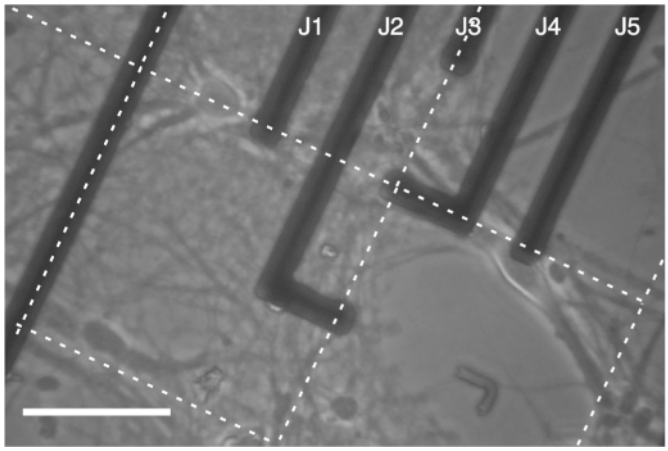

Figure 3.7. Five channel recording from patterned neurons.
(a) Phase contrast image of neurons growing on a MEA. The dashed grid indicates the central position of the PLL grid (25 mm wide lines and 75 mm wide spaces). Scale bar = 50 mm. Figure taken from James et. al. [3].

In cases of coincident activity, the microelectrode with the larger background noise had spikes with larger amplitudes than the other microelectrode, presumably due to an increased sealing resistance. We examined the conduction velocity of prominent spikes from clusters A and C. The average conduction velocity from J4 to J2 in cluster A was calculated to be 0.23 ± 0.06 m/s (n = 57). The peak-to-peak value of the spikes on J2 and J4 in this cluster was 66.3 ± 9.0 mV and 31.8 ± 4.6 mV, respectively. For cluster C, the spikes traveling from J4 to J5 had an average conduction velocity of 0.29 ± 0.042 m/s (n = 9). The peak-to-peak value of the spikes on J4 and J5 in cluster C was 79.2 ± 7.8 mV and 38.4 ± 8.5 mV, respectively. Differences in the spike amplitudes on different channels can be caused by a number of factors such as variations in sealing resistance or ion channel density.

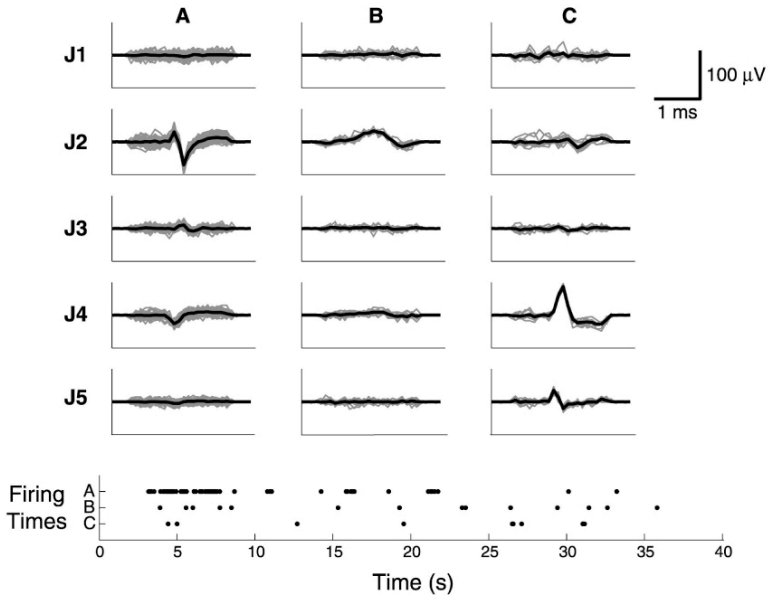

Figure 3.8. Results of multi-channel clustering
Similar multi-channel spikes grouped into three clusters: A (57 spikes), B (14 spikes), and C (9 spikes). Individual spikes (dashed lines) are superposed and plotted in the assigned cluster on each channel with the average waveform (solid lines). A rasterplot of the firing times of clusters A, B, and C shown at the bottom. Figure taken from James et. al. [3].

Depending on the dimensions of the patterned PLL on the microelectrode array, the number of cells found near microelectrodes varied significantly. Pyramidal neuron cell bodies often conformed well to the patterns produced with both μCP and the lift-off method, while neurites tended to stray from the guidance cues after 4-7 days *in vitro*. Quantitatively, PLL grids with large duty cycles (large ratio of PLL width to bare insulator width) were easily traversed by neurites, while smaller duty cycle grids were more successful at confining neurite growth (compare confinement in Figure 3.5a,b to 3.7).

3.3.2 *Modeling*

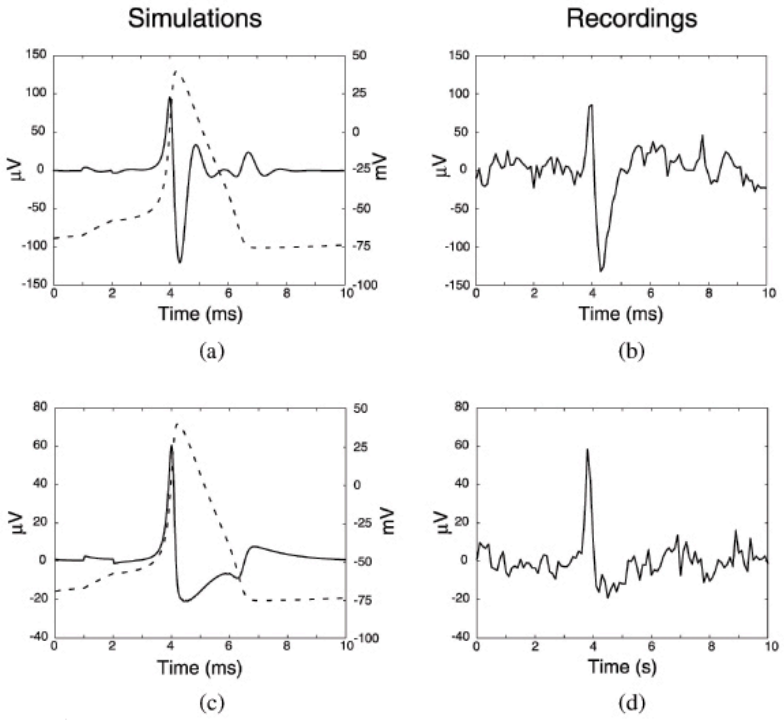

Figure 3.9. Comparison of measured and simulated extracellular potentials Simulated membrane potentials (dashed lines in a, c) and corresponding extracellular potentials (solid lines in a, c). Parameters used are (a) Rseal=1 M W, Cp=500 pF, |Ze|=0.5 M W; (c) Rseal = 0.1 M W, Cp=300 pF, |Ze|=0.5 M W. Examples of recorded extracellular potentials (b, d). Figure taken from James et. al. [3].

Extracellular potentials can vary dramatically in shape, and investigators have found potentials that resemble the first, second, and third derivatives of the intracellular potential [131, 132]. Grattarola and Martinoia illustrated a single compartment circuit model built upon the original Hodgkin-Huxley formulation that demonstrates the effect of parameters such as sealing impedance, parasitic capacitance, and electrode impedance on the detected extracellular waveform. By varying these parameters, we were able to simulate extracellular waveforms that resemble the waveforms recorded (Figure 3.9). The fundamental equation solved numerically in MATLAB was:

$$C_m \frac{dV_m}{dt} = I_{stim} - \sum_i g_i(V_m, t) \cdot (V_m - V_{0i})$$

with the membrane capacitance C_m (1 μF/cm^2), membrane potential V_m, stimulation current I_{stim}, voltage and time dependent ion channel conductance $g_i(V_m,t)$, and ion equilibrium potential V_{0i}. In our simulations, we considered ions i = Na, K, as well as a constant g_L leakage conductance. Equations for $g_i(V_m, t)$ were of the same form as those used by Hodgkin and Huxley [133]. The membrane current found from this solution was then input into the circuit described previously to calculate the extracellular potential. The area of membrane assumed coupled to the electrode was 100 μm^2, and values for Z_e were based on the impedance measurements described earlier. Variation of the circuit parameters produced spikes of differing shape and amplitude that resembled those observed *in vitro*. For qualitative comparison, a simulated membrane potential and extracellular spike are shown in Figure 3.9 with an example of a recorded waveform. In addition, varying the maximum conductance of ion channels will also alter the extracellular waveform, and given that different specializations (soma, dendrites, axon) within neurons contain different densities of ion channels, the extracellular waveform may indicate the area of a cell that is coupled to a particular electrode [134].

3.4 Summary of Electrode Arrays for Patterned Cell Culture

We have developed a method of fabricating planar devices with multiple closely spaced platinum recording sites for extracellular monitoring of cultured cells. These recording sites were found to have good electrical properties for neural recording. In addition, we created patterns of guidance proteins in controlled geometries on the surface of the multielectrode array, aligned to the recording sites, using microcontact printing and photolithographic techniques.

Dissociated neuronal cells were cultured on the devices, and found to follow the constructed patterns. The spontaneous and chemically evoked activity of these cells was observed on the extracellular electrodes, although the yield of active cultures was very low. Immunocytochemistry was used to compare cell morphology and electrophysiological recording. In order to understand the variance of spike shapes recorded, we simulated the neuron-electrode interface with an equivalent circuit model. These experiments show promise for the use of substrate multielectrode arrays with chemical patterns. They will aid in designing cultured networks with known, simpler topology, and perhaps even give the experimenter control over synaptic connectivity. The non-invasiveness of the extracellular recording sites and the ability to have several sites spaced near or under a single neuron makes these devices very well suited for developmental studies of constructed simple networks.

CHAPTER 4: MULTIELECTRODES FOR *IN VIVO* MULTINEURON ELECTROPHYSIOLOGY

The ability to reconstruct, *in vitro*, very small networks of real neurons will result in profound new ways to study the role of biochemistry in neural development and computation. The fact that these networks are reconstructed, however, means that the original architecture of the network is lost. The extraordinary computation performed by the hippocampus, and even smaller sensory networks, can provide us with great insights into the general principles of natural nervous system operation. To this end, we require the ability to record from networks of neurons *in vivo*, an experimentally difficult problem. As described in the introduction, there are optical and electrophysiological approaches to solving this problem. Optical techniques involve imaging neurons stained with a dye that indicates action potential firing via some mechanism. The limitations of current optical methods, the majority of which use voltage or calcium sensitive dyes, lie in their temporal resolution (many tens of milliseconds) and their dynamic range [60].

Electrophysiological techniques for multiunit recording either involve multiple standard glass pipettes, for simultaneous intracellular recording, or multiple extracellular recording devices. Independent maneuvering of more than three or four intracellular pipettes is unfeasible due to constraints of space about the preparation, limitations in time and stability of each pipette. Intracellular techniques damage the cell, and limit the recording time to an hour or two at most. For this reason, many investigators have turned to using multiple extracellular electrodes. Doing so sacrifices any knowledge of slow or DC behavior, such as postsynaptic potentials, because of the AC coupling of extracellular devices. In addition, the data analysis required to extract single unit firing times from multiunit, multielectrode data is extensive.

Microfabrication techniques have brought new inspiration to extracellular multielectrodes, however, with their great potential to increase the quality, quantity, and geometry of recording sites. In addition, new materials science methods may provide integrated, improved transduction methods, including using carbon nanotubes to measure local ion concentration.

4.1 Fabrication Methods

The foundation for fabrication of multielectrodes for *in vivo* use exists in the literature [62, 135-138]. Details specific to the metallization and passivation steps in the process we have used were largely carried out by Dr. C. James [139] and M. Meyer (Cornell, Applied Physics undergraduate thesis) in developing the substrate MEAs used in the previous chapter. Several notable extensions to the process were developed in order to create *in vivo* multielectrodes. The process is a combination of the probe process and substrate MEA processes. Specifically, it involves the patterning of conductor traces used in the substrate MEAs, and the deep-RIE structure formation used in the neuroprosthetic devices. The process flow is illustrated in Figure 4.1.

Processing begins with bare Silicon four inch substrates. Devices consisted chiefly of a single metallization layer insulated by silicon nitride, with through-wafer trenches etched by deep reactive ion etching (DRIE). Thin (350 micron) double side polished four-inch Silicon wafers were cleaned using standard basic and acidic baths, followed by de-ionized water rinses. A pyrogenic steam oxidation was used to grow 1.3 microns of silicon oxide on both sides of the wafer. Gold was then patterned either using a resist mask an ion milling, or with liftoff. The following section addresses some differences between the two methods, and the liftoff procedure follows here. Wafers were then prepared for gold liftoff.

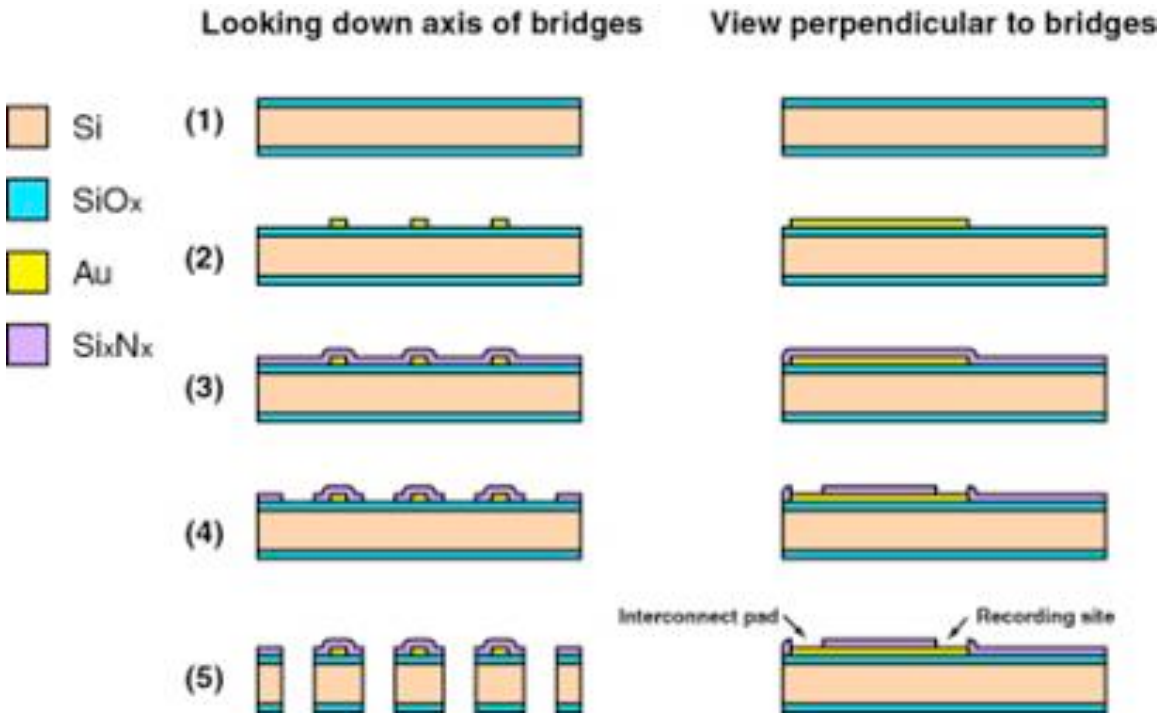

Figure 4.1 Fabrication of multielectrodes for in vivo recording
Thermal evaporation of 1.3 mm of oxide onto bare Silicon wafer (1). Patterning of Au traces on oxide film, (2). Passivation of Au traces with an insulating PECVD film or stack, (3). RIE through passivation to Au in specific locations, forming recording sites and interconnect pads (4). RIE through thermal oxide, and DRIE through Silicon substrate, releasing devices, (5).

After vapor priming with HMDS (hexamethyldisilazane) to promote adhesion, a 2 micron thick photoresist masking layer (Shipley S1818, 4000 rpm, 40 s) was then spun onto the wafer. A contact aligner (Karl Suss MA6) was used to expose the resist, and an image reversal was carried out. An ammonia bake followed by flood exposure and development in Shipley MF321 developer resulted in a resist profile suitable for liftoff. A 10 nm thick adhesion layer of Ti was e-beam evaporated onto the substrate, followed by 250 nm of Au from a thermal boat. Wafers were soaked overnight in a Shipley 1165 resist strip bath, followed by a 15 minute acetone bath with ultrasonic agitation. After a brief (1 minute) oxygen plasma descum, the wafers were then placed in a plasma enhanced chemical vapor deposition (PECVD) system for deposition of

the insulating nitride. A 900 nm thick film of silicon nitride was deposited. Photoresist was spun on the nitride layer and exposed with an optically aligned mask having recording site and contact pad features. Unmasked insulating nitride was etched away (exposing the gold) using a standard anisotropic CF_4 (Carbon Tetrafluoride) plasma RIE. The resist was stripped, and the process repeated with thick resist (Shipley S1045, 1500 rpm, 30 s) and a mask having large trench features that form the bulk structure of the device. The same anisotropic CF_4 plasma etch recipe was then used to remove the base oxide layer in the trenches, exposing the bulk silicon. Finally, an inductively coupled, inhibitor driven anisoptropic deep etcher was used to etch these trenches through the wafer, stopping at the backside oxide. Individual devices could then be broken out of the wafer.

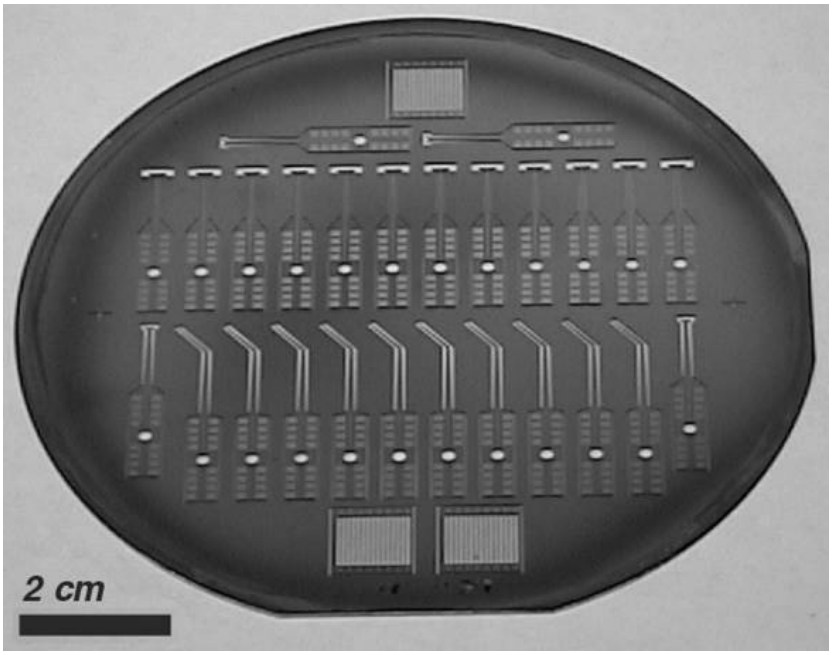

Figure 4.2. Completed wafer having multielectrode traces and through wafer holes
Miniaturization of the interconnect permits a higher density of devices on the wafer and better yields.

4.1.1 *Gold patterning – liftoff*

The fabrication process for the substrate MEAs utilized an ion mill to pattern the gold metallization layer. While this method has the advantage of needing only a resist mask, it had some drawbacks which were remedied by the move to liftoff. Patterning the gold with an ion mill was time consuming in that it required each wafer to be processed individually, and the pump down time required before each mill was ~ 40 minutes. In addition, without the correct neutralizer settings, the ion mill tended to burn the resist mask at the edges of resist lines (Figure 4.3a). In many cases this resist was difficult or even impossible to remove, using either solvent or an oxygen plasma. An adequate recipe was obtained from Dr. F. Albert, which required active adjustment of the neutralizer current during the ion mill such that the beam current was zero whilst the shutter is open. After this, the resist was never badly burnt, and could be removed with an aggressive solvent. Typically, a 15 minute sonicated acetone bath, followed by two 15 minute acetone rinses completely removed the resist.

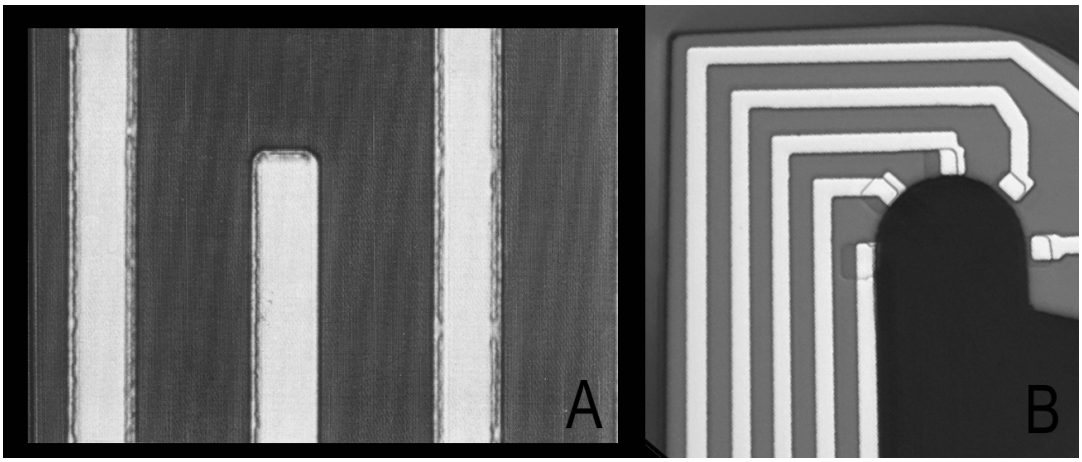

Figure 4.3. Comparison of gold patterning techniques
Gold traces patterned using a) ion milling without active neutralizer current balancing and b) liftoff. The traces in a) have a burnt resist residue at the edge, which was impossible to remove using standard solvents in ultrasonic bath or an oxygen plasma. The traces in b) have no resist residue.

Using liftoff, however, enabled several wafers to be processed in parallel (typically three four-inch wafers, as this is the limit placed by the evaporator chuck). In addition, it leaves no possibility for burnt resist residue (Figure 4.3b). The image reversal step needed to create an adequate resist profile for liftoff requires a 30 min oven prime and an an 80 minute ammonia bake, time costs that are easily made up for by the parallel processing of wafers. Resist adhesion was on some occasions a problem with the large clear field masks used for liftoff, and care must be taken that the mask is thoroughly rinsed with de-ionized water and isopropyl alchohol after processing in 1165 resist strip (to remove the solvent-surfactant solution). In addition, the HMDS vapor oven prime of the wafers is helpful in removing water that may have adsorbed into the thick thermal oxide layer. Spin priming with HMDS is inadequate.

4.1.2 *Insulation issues with deep etching*

The composition of the passivating layer has several consequences for device electrical and mechanical characteristics. Although polymer insulation such as polyimide is an attractive option for it's ease of application (it can be spun on), and in some cases it can be photopatternable, the DRIE chamber is susceptible to contamination, and exposing polymers other then photoresist (even just sidewalls) to the plasma is unacceptable. For this reason, the insulating layer used was a PECVD one. Initial devices were made using PECVD silicon nitride. A 60 minute deposition results in an approximately 900 nm thick film. The calculations of Sakurai [140] predict this film will have trace to bath and trace to trace parasitic impedances of at least tens of MΩ at 1 kHz, and as such is adequate. The nitride film has a dielectric coefficient of approximately 7, and thus is a better electrical insulator than oxide, with a coefficient of only about 3.

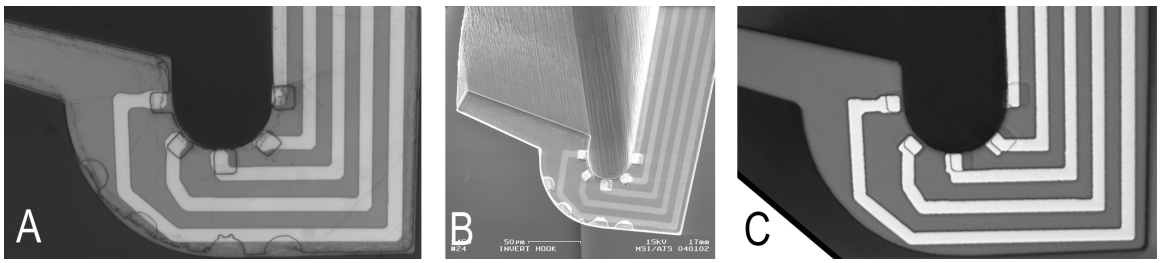

Figure 4.4. Cancelation of passivation stresses using a triple stack.
Completed device in part a) shows cracked silicon nitride passivation layer (circular "bite marks" along bottom edge of device, reaching inward to lowermost gold trace). These marks appear during the deep etch, and are usually near the edge of a deep etched trench. Part b) is an SEM of the same device, after removal of resist mask. The "bite marks" are seen to be cracked and flaked off nitride, exposing the gold below (as evident by exposed areas being as bright as intentionally exposed gold recording sites). In c) we have a completed device fabricated using a triple stack insulating layer, with no defects.

However, as is seen in Figure 4.4a, the silicon nitride film was found to be prone to cracking at the edges of trenches after the deep etch. These defects are presumed due to stresses in the film. In addition, the nitride film deposited by the IPE PECVD has been reported (Dr. P. Infante, CNF, personal communication) to have poor adhesion properties. Although the film typically appears continuous after deposition, with some cases of flaking off over large gold areas (bonding or interconnect pads), after deep etching the film has many cracks near edges of trenches. These marks appear after deep etching, while the film is underneath the resist mask. Upon stripping of the resist mask and SEM imaging of the device, it was found that the nitride was coming off (Figure 4.4b). In addition, electroplating devices with defects showing platinum black growing in areas where defects had appeared, confirming that the defects were indeed a flaking off of the insulating layer. Traces far away from trench edges were unaffected, however, so these early devices yielded many functional devices.

In order to alleviate these problems, however, the latest generation of devices were fabricated using a triple stack of 200 nm of oxide, 400 nm of nitride, and 200 nm of oxide, all deposited using the PECVD. This triple stack is designed to have canceling stresses [62] and because it is composed of multiple films it will have mismatched pinhole defects, reducing the chance of a pinhole through the entire insulation. Figure 4.4c shows completed devices using this film, and we note the edges no longer exhibit cracking. Measurement of the electrical characteristics for the nitride film yielded a trace to trace impedance of ~ 10 MΩ, indicating adequate insulation. A similar measurement for the triple stack insulation resulted in a trace to trace parasitic coupling of ~ 6 MΩ.

4.1.3 *Two step RIE thinning*

The DRIE probe etch process results in devices that have thickness equal to that of the wafer. These devices are rigid and quite strong, useful when there is adequate room in the preparation and they are required to be stable over large distances (several mm). However, this thickness may prove a hindrance in smaller preparations. In this case, the fabrication process can be modified to thin certain areas of the device, usually the shank/recording site areas. This can be achieved simply by using an initial DRIE of the backside of the wafer. The backside is resist masked, and a DRIE timed to thin the wafer to the desired thickness in the appropriate areas. The most important factors in this processing were to provide alignment marks on the backside such that the front side features can be correctly positioned (again requiring a backside contact alignment tool), and that special care be taken when patterning the backside not to dirty the front side of the wafer by placing it face down on contaminated hot-plates or spinner chucks. Figure 4.5 illustrates a “spatula” linear multielectrode made with the thinning process.

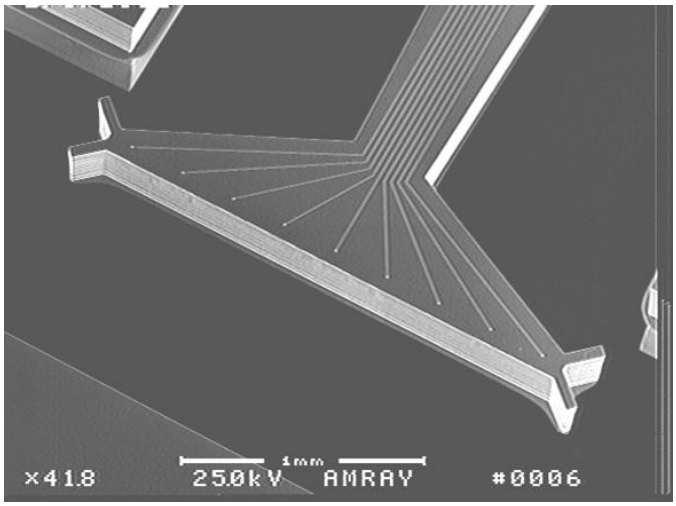

Figure 4.5. A thin multielectrode fabricating using dual DRIEs.
Two DRIEs were used to produce this device, having shank thickness of about 100 microns. The cross section of the bulk wafer and the depth of the two etches can be seen at the upper left corner of the image.

4.2 Initial results

Once devices have successfully been fabricated, the nontrivial problem of interfacing their conductor traces to external macroscopic amplification and digitizing equipment must be addressed. The first devices fabricated consisted simply of a regular 3 by 3 array of recording sites. The interconnection scheme for these devices was that of normal prototype electronics: ultrasonic wire-bonding of fine gauge wire between interconnect pads and a normal chip carrier. The chip carrier provides a small rectangular chip mounting area surrounded by gold pads which connect to the pins of a standard dual inline pin (DIP) package. This package was cut in two at the midline with a diamond saw to enable the probe end of the multielectrode to be inserted into a biological specimen (Figure 4.6). This DIP package could then be plugged into a standard female dip socket, with a wiring harness connecting to the input stage of several four channel extracellular amplifiers (A&M Systems Model 1700). A schematic and photograph of the apparatus is seen in Figure 4.7.

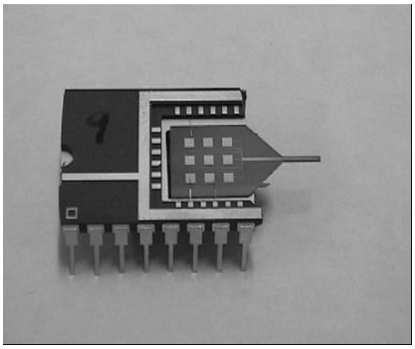

Figure 4.6. First generation electrode
Interconnection scheme for test electrodes consisted of a cut chip carrier, with wire bonded traces. SEM of rectangular array of recording sites (right).

The disadvantage of this interconnect scheme lies in the requirement that each trace of each chip needed to be individually wire bonded, a time consuming process.

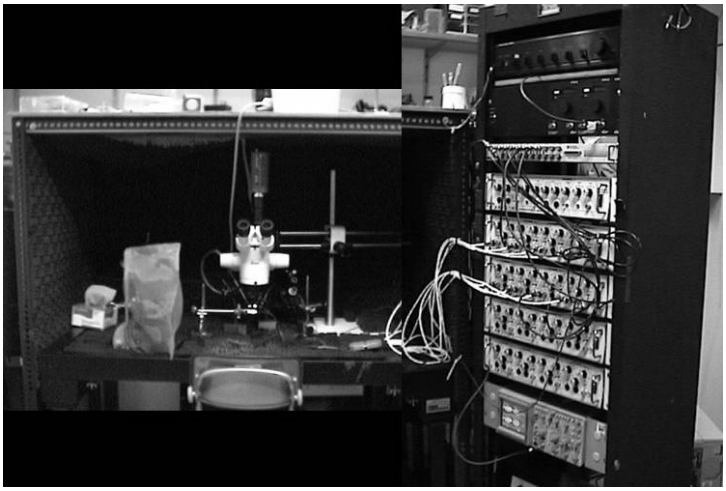

Figure 4.7. Schematic of neural recording apparatus
Apparatus consists of microscope, multielectrode in manipulator, voltage amplifier, oscilloscope, and PC. Note the number of wires in the harness, just for 8 channels.

4.2.1 *Cricket and larva initial tests*

These rectangular arrays were tested for proof-of-principle in two preparations. The device was initially inserted into the cricket brain, and a recording of spontaneous biolelectric activity made. Bursts of multiunit activity were recorded from a single channel, verifying device electrical integrity.

Larva of the stalk-eyed fly *Cyrtodiopsys wallei* were then used as a second test preparation. The larva have several motor nerves that project in a fan shaped pattern from the brain. The larva can be dissected into a "fillet" preparation, in which these motor nerves are spread in a horizontal fashion. The regular array was brought under the motor nerves, with the hope of recording spatially distributed activity. The preparation had to be maintained in bath, however, and no method of sealing the nerves to the array recording sites could be developed. Device operation was verified by poking the array into sheets of muscle below the motor nerves, at which points large muscle spikes were recorded on four sites of the array (a single four channel amplifier was available). However, the inability to record spikes from motor nerves through bath but in close proximity to the electrode array demonstrated the need for a geometry that can be readily sealed to neural tissue.

4.3 Conduction sampling devices

4.3.1 *"Spatula" linear array—shunting by device surface*

The most common method of achieving adequate sealing of an electrode to a nerve whilst insulating the electrode from the bath is by lifting the nerve out of the bath with the electrode, and covering the exposed nerve with petroleum jelly. The petroleum jelly is insulating, and provides adequate isolation of electrode and bath, whilst preventing the exposed nerve from drying out. In order to utilize this method of

insulation in a multielectrode, the linear array or “spatula” seen in Figure 4.5 was fabricated. The first generation “spatula” did not have the v-shaped guides at either end, and as a result the nerve tended to simply slide down to the neck of the device. The device used for the recording, however, contained the v-shaped guides into which the nerve cord could be threaded, and hence aligned across the nine evenly spaced recording sites.

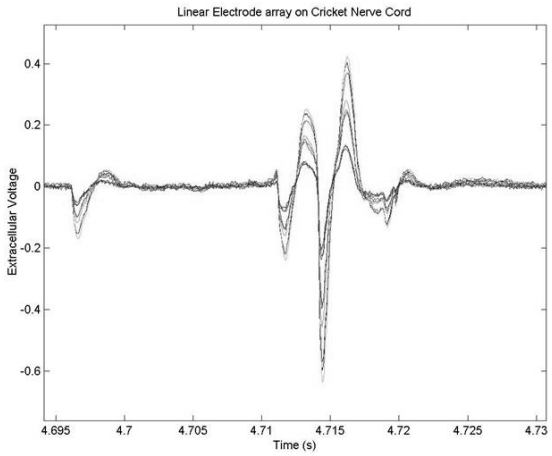

Figure 4.8. Recording from the cricket nerve cord with the linear “spatula” array The array consisted of nine linearly spaced recording sites, each 200 microns apart, spanning ~ 2 mm. The channel number is indicated by color. Note the lack of noticeable propagation delay.

This form of isolation was carried out, using the “spatula” array, on a cricket ventral nerve cord preparation. Briefly, the cricket abdomen was dissected ventrally to expose an adequate length of abdominal nerve cord. The animal was anesthetized with CO_2, pinned ventral side up, and a rectangular patch of cuticle approximately 2 x 2 mm was carefully removed from the midline and rostral-caudal center of the abdomen. Fat and muscle tissue were then picked away from the nerve cord just beneath the cuticle surface. The nerve cord was then draped over the spatula, through the V-guides. The nerve cord was then gently lifted above the abdomen. Due to surface tension, this lifts a sheet of saline solution below the spatula. A careful dab with a twisted lab wipe

adsorbs this sheet, leaving only the two lengths of cord at each end of the spatula connecting the spatula to the bath. Petroleum jelly is then applied to the entire recording area, underneath and above the spatula. This method of isolation produces the largest signal to noise ratio recordings, due to the high impedance return path for current from the firing neurons. Configurations in which a quantity of saline connects the recording device and the bulk bath produce much lower amplitude, biphasic or triphasic spikes, while well isolated ones produce large amplitude, monophasic spikes. This can be understood in terms of the sealing impedance in the equivalent circuit model of Chapter 3.

Even with adequate isolation, however, this experiment demonstrated an inherent problem with continuous planar arrays used to record in this manner, illustrated in Figure 4.8. We note that the signal from each channel is virtually simultaneous, and simply appears to be scaled versions of the same waveform. With a spacing of 200 microns between recording sites, we expect to see delays between channels of approximately 1 or 2 samples, and over the complete device 10 to 20 samples, or 1 to 2 ms. However, close examination of the trace reveals almost zero lag between the first and last channels! The geometry of the device is such that over the recording length, the nerve cord is entirely insulated. This creates a shunting effect, akin to myelination, in which high impedance insulation about the nerve cord induces the action potential to travel much faster, in effect “popping” from deinsulated “node of Ranvier” to the next. In addition, any amount of residual saline on the surface of the device will act to shunt recording sites, making them isopotential. As a result of this experiment, more design was needed to develop devices in which recording sites could be adequately isolated from each other yet permit the nerve cord to be in bath between sites, either via a different geometry, mechanical squeezing out of residual saline, or some surface chemical modification.

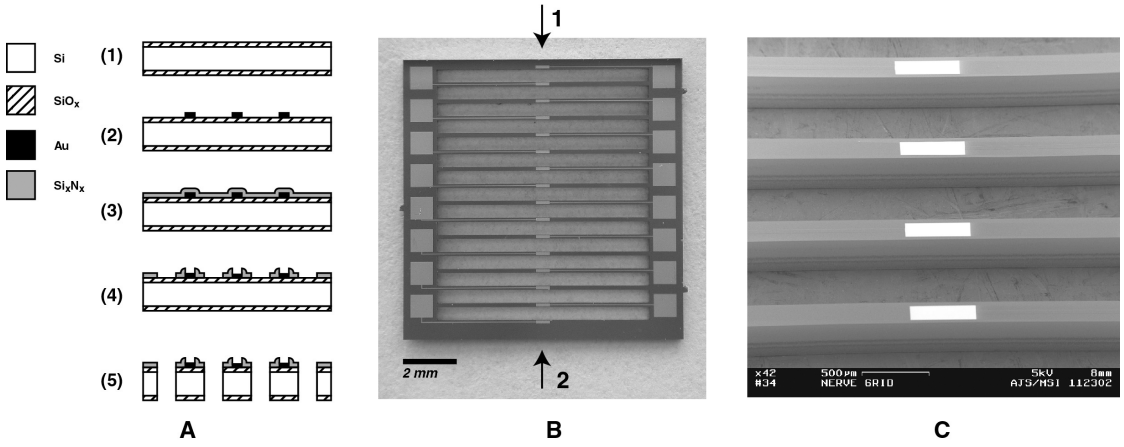

Figure 4.9. Geometry of the bridge array multielectrode
The baseline conduction velocity based sorting device, designed for the cricket ventral nerve cord. Consisting of sixteen narrow bridges, it permitted isolation of recording sites from each other, and a substrate ground plane.

4.3.2 *Grid design, construction, and characterization*

In order to verify that the fabrication technology could produce devices that meet the above criteria, a simple, baseline measurement device was designed. The goals of this device were to prevent having a contiguous surface between recording sites, and to verify that this makes possible recordings with both a large signal to noise ratio *and* proper conduction characteristics. The multielectrode designed to meet these requirements, which we call the "grid" multielectrode, consists of sixteen narrow silicon bridges, 150 microns wide and 350 microns tall, spaced evenly over a centimeter, with passive rectangular gold recording sites on the top surface (Figure 4.9) [141]. The nerve cord was placed perpendicularly across the bridges. In this geometry, the nerve spans a 350 micron deep, 450 micron wide trench between each recording site, permitting adequate isolation of recording sites from each other and a platinum ground plane. The recording sites are 500 microns wide (in the direction perpendicular to the nerve cord) and span 100 microns, giving a total area of 50,000 square microns. Each device was glued to a 0.5 inch square piece of 0.003" thick

platinum sheet, to act as a ground plane, which was in turn mounted on a glass slide. Eight-conductor flat flex cable of pitch 1 mm was glued at either side of the device, and conducting epoxy used to connect cable leads to interconnect pads. The signal was amplified (x1000) and band-pass filtered (100Hz low-pass, 5kHz high-pass, A-M Systems Model 1700) before being sent to a PC for digitization. Each channel was acquired (20kHz sampling rate, National Instruments MIO-16E-1) directly into Matlab (Mathworks Inc.) where analysis was done offline using custom scripts. Once the fabrication was complete, we measured the electrode recording sites to have an impedance of 12.6 ± 3.0 kΩ (n = 16) at 1 kHz.

4.4 Background and biology of the cricket cercal system

The preparation with which we are testing our grid device, the cricket cercal system, is one of the most fascinating neurobiological systems discovered to date. It is one of the few systems in which complicated neural integration can be observed in a system of tractable size [56, 142]. As described in Figure 1.2, the cricket cercal system provides the animal with detailed information about the motion of air [55, 143]. It does this through the movement of biomechanically tuned tactile hairs [144]. There are approximately 1200 of these hairs, located on two conical appendages (the cerci) that protrude caudally and at right angles to each other from the abdomen. The hairs are grouped into classes of different length and orientation of movement. The hairs are tuned in frequency by their length, longer hairs transducing low frequency near field wind motion, shorter hairs higher frequencies. In addition, the base of each hair rests in a cuticular socket, which restricts its movement a) to the horizontal plane, and b) to a single wind direction within the plane. In this manner, the cerci and mechanosensory hairs form a “filter set” for wind direction and frequency, from which higher level neurons can construct more complicated dynamical sensitivities. Primary afferent

neurons project from the base of each mechanosensory hair to the terminal ganglion (Figure 1.2) [55]. In the terminal ganglion these primary afferents synapse onto the dendrites of local and projecting interneurons [70-72, 144, 145]. Some of these interneurons are the giant fibers, which project all the way from the terminal ganglion to the thoracic ganglion, a distance that can be 1 cm, and some to even higher centers (e.g. the brain). These are the large axons we predominantly record from in the ventral nerve cord with the multielectrode array (because they are the largest in diameter, and hence spike amplitude).

The connection between the afferents and the giant interneurons is an intriguing feat of integration. The volume inside the terminal ganglion that the afferents project to is determined by their directional sensitivity. That is to say, the terminal ganglion is composed of different regions of axons of different wind direction sensitivity. Thus, a map of wind direction is formed inside the terminal ganglion (Figure 1.2). A giant interneuron can then introduce its dendrites into this map with different synaptic strengths, and build up sensitivity to any direction. The directional sensitivity of the giant interneurons has been predicted, in fact, from the anatomy in this manner [142, 145-149]. The great excitement about this system comes from the ability to directly observe how the shape and structure of a neuron's dendritic arbors determine its firing behavior. The giant interneurons are thought to be important for evasive behavior (escape response) and mate detection (hence the large diameter and fast conduction times). A total of about 22 giant fibers are found (11 in each nerve cord). The system has been studied extensively, as it is such a wonderful model of neural integration and information processing. These studies were all done on single units, however, and it has been experimentally impossible to record from more than a single giant simultaneously. In this system it seems highly likely, due to the presence of local interneurons, that there may be some covariance in the spike trains of the

giants. This would mean that neurons are "working together" to transmit information in their relative spike times, and not just working independently to transmit some amount of information per neuron, that is then summed at higher centers. It has been impossible to look for this type of multiunit encoding due to lack of experimental data, motivating our multielectrodes.

4.4.1 *Anatomy*

As we have discussed, the morphology of many of the ~ 12 giant wind motion sensitive interneurons is known. The species we have cultivated, however, *Gryllus bimaculatus*, is less common, and as such we carried out an Osmium Tetroxide stain to confirm the size and position of the giant fibers in the nerve cord (Figure 4.10).

Figure 4.10. Morphology of cricket ventral nerve cord.
Consisting of two hemi-cords, the axons of the large giant wind motion sensitive fibers are seen as large clear areas. The identity of known giant interneurons are superposed as per the nomenclature of Jacobs and Murphey (see text).

The Hodgkin-Huxley formulation of spike propagation, using simple ionic conductances, predicts that the conduction velocity and amplitude of extracellular spikes will be proporational to axon cross-sectional area. This can intuitively be seen in an analogy to standard conductive metal wires: large diameter wires will inject more current into the surrounding media, and have lower axial impedance. Using these facts we can garner additional qualitative information about which neurons are producing which extracellular spike. An image of a 10 micron section of stained nerve cord tissue is seen in Figure 4.10. Superposed are the hypothesized identities of known giant interneurons, following the nomenclature of Jacobs and Murphey [150].

To make comparisons of measured spike amplitude and conduction velocity to axon diameter, we measure their area from the image in Figure 4.10 Areas of axons, measured from Figure 4.10, for the left and right nerve cord, are presented in Table 4.1. We will use these data at a later point in hypothesizing neuron identity. At this point, however, we can already see a theoretical hurdle for spike sorting using conduction velocity. We note that in the right hemi-cord axons of area 286 and 287 square microns were measured. This would equate to a difference in conduction velocity of 0.3 %. In the literature, however, the accepted biological variance in spike conduction velocity from a neuron is about 1 %. Given this, these neurons would be impossible to resolve using conduction velocity information alone.

Table 4.1: Measured diameters of giant fibers.

Cell	Left Hemi-Cord Area (square microns)	Right Hemi-Cord Area (square microns)
LGI	**950**	**944**
MGI	**649**	**699**
unknown	**409**	**332**
unknown	**397**	**287**
unknown	**388**	**286**
unknown	**295**	**277**
unknown	**206**	**273**

4.4.2 *Cricket dissection*

The length of nerve cord we wish to record from with the grid multielectrode requires a more extensive dissection. We again use the cricket ventral nerve cord as our model nerve bundle. Overall, the goal is to have approximately 1 cm of free nerve cord connected to the intact cerci (Figure 4.11). Late instar (two molts from adult) immature crickets were selected. Animals were anesthetized with CO_2, decapitated, and the legs were removed. The preparation was pinned to a Sylgard dish, ventral surface upward. An incision was made in the cuticle connecting the thoracic and abdominal ventral surfaces. The thoracic underplate was then lifted and cut away. Two rostral-caudal incisions were made in the abdominal cuticle, extending from the opening in the thorax to approximately 3 mm before the base of the cerci.

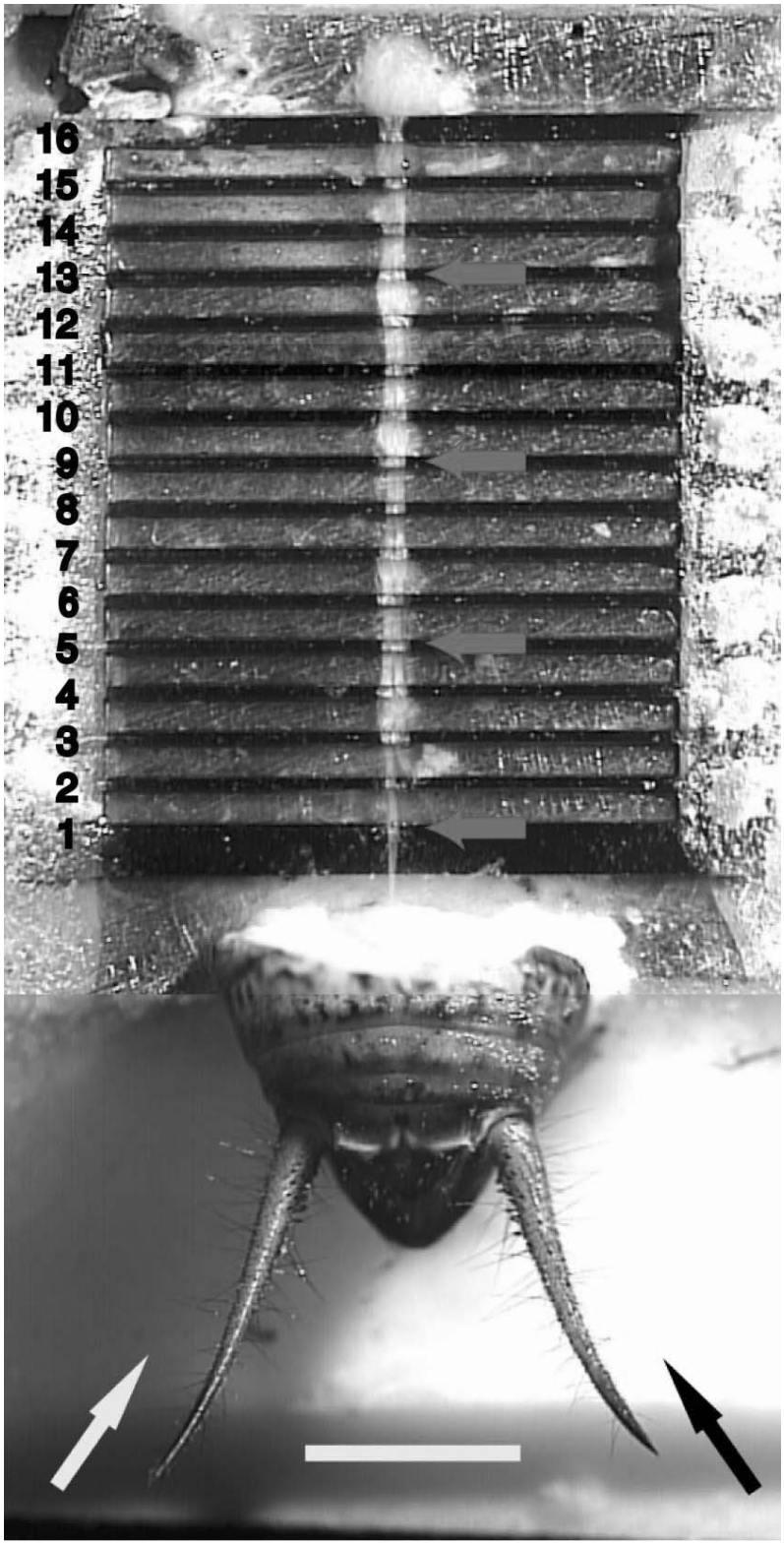

Figure 4.11. Cricket cercal system and ventral nerve cord on the bridge array
The dissection leaves a conical cap of cuticle, having intact cerci. The ventral nerve cord projects from this cuticular cap across the sixteen channel array.

This resulted in a thin flap of cuticle, whose rostral end could be gripped in a pair of forceps and peeled back. Tissue connected to the internal surface of the cuticular flap was gently scraped off of the cuticle as it was peeled back. The flap was then cut away. Connectives to the thoracic and abdominal ganglia were then careful cut, moving caudally from the thoracic ganglia, until the nerve cord was entirely free of connective nerve and tissue. The nerve cord was then moved to one side of the open abdominal cavity. The gut was located, gripped at a caudal location, and pulled free of the preparation. A circular cut around the abdomen was then made, approximately 3 mm from the end of the abdomen, connecting the first two incisions. This leaves the nerve cord and a dome shaped piece of cuticle with intact cercis free for mounting on the multielectrode (Figure 4.11). One of the two connectives of the nerve was cut to reduce biological noise.

4.5 Recordings from the cercal system with the grid array

The dissection was carried out, and the nerve cord draped across the grid recording sites (Figure 4.11). Action potentials from the giant fibers of the cercal system were elicited with a pipette, which was used to manually deliver “puffs” of air across the tactile hairs. A 40 second recording was made (Figure 4.12), during which the pipette was aimed in one direction for the first half of the recording (Figure 4.12, black arrow), and in another (Figure 4.12, white arrow) for the remaining 20 seconds. Activity seen in Figure 4.12a before t = 4 seconds corresponds to the first stimulation direction, and after t = 5.75 seconds to the latter. Puffs were presented at roughly 4-6 Hz, and bursts of spikes were seen, stimulus locked, to appear on all channels. Laminarity of airflow was not controlled, and interference from the substrate was no doubt present.

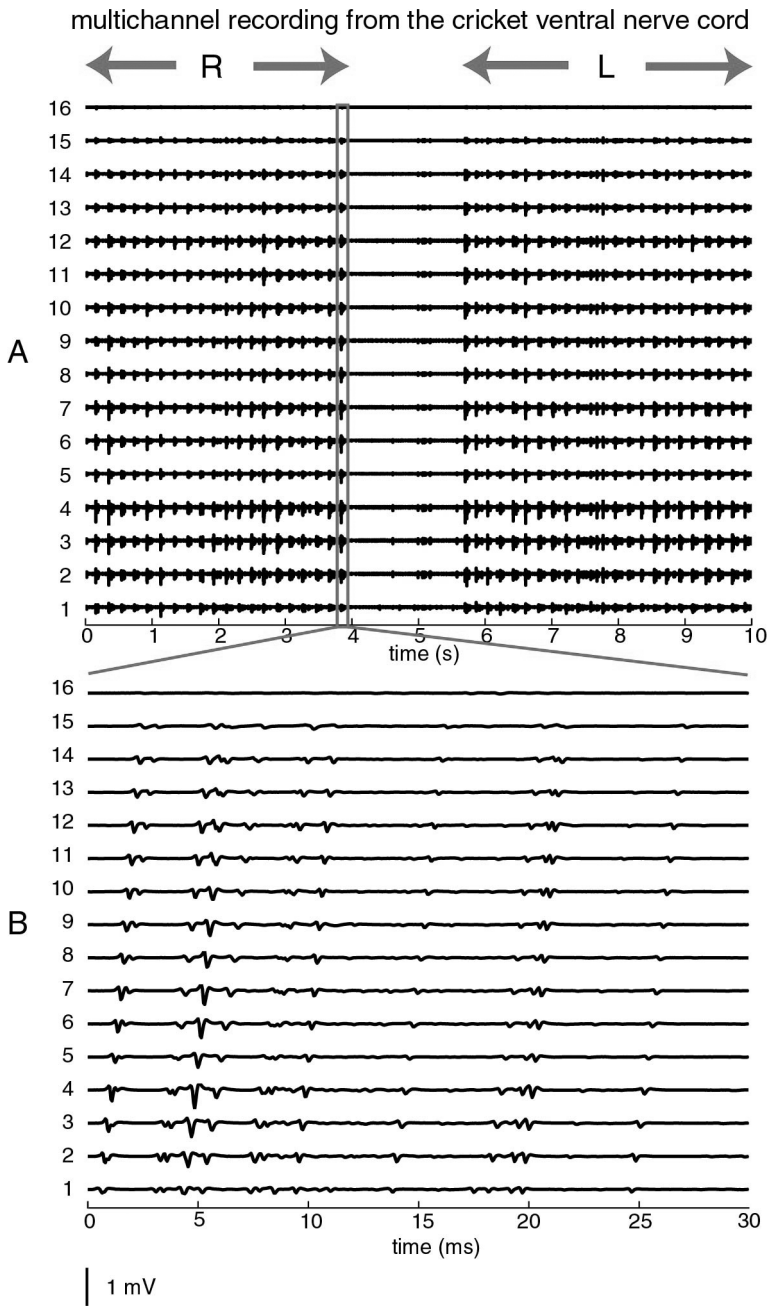

Figure 4.12. Recordings from the cricket ventral nerve cord with the bridge array

Bursts of activity elicited with a puffer pipette from below right and below left (A). Time expansion of the highlighted burst is shown in (B). Note in (B) that spikes of varied amplitude and conduction velocity are visible, and in some cases, spikes that appear to be individuals on one channel are clearly separated into two spikes on earlier (or later) channels.

4.6 Spike Sorting

Having made multielectrode recordings, the task becomes extracting multineuron firing times from multichannel data. This problem is combinatorial in nature, and is complicated by the nonstationarity of spike shapes. Neurons have a refractory period, limiting the maximum rate at which they can fire, but aside from this any combination of neurons can fire at any time. This means that as the number of neurons increases, the probability of having overlapping spikes increases. Deconvolution of data in which three or more neurons overlap with arbitrary phase has not been generally solved in the literature for biological systems. Although this problem is one that it seems blind source separation and higher order statistical methods from signal processing should be adequate to tackle, that has not yet been the case. Often these methods require the signals to be statistically independent. This is rarely the case. If the biologically relevant time scale is short, one can expect overlaps to be frequent. For instance, in the cercal system, if the wind stimulus of interest is a wasp wing-beat lasting a few milliseconds, and several neurons whose extracellular spike waveform lasts 0.5 millisecond fire, one can expect many overlaps to occur. Because the spikes are carrying information about such a short lived event, you can expect the first 10 milliseconds post-stimulus to be extremely crowded with activity.

An extensive literature exists on various methods to approach this problem; for a review see Lewicki [125]. A descriptive example of neural data showing spikes from two putative units with different timing is seen in Figure 4.13. The earliest and simplest spike sorting methods used an amplitude threshold to discriminate between spikes. Obviously, errors due to spikes from different neurons having equal amplitude, and from bursting neurons whose spike amplitude varies are unavoidable using this

technique. In addition, errors occur during overlaps as these can drastically change spike amplitude (Figure 4.13).

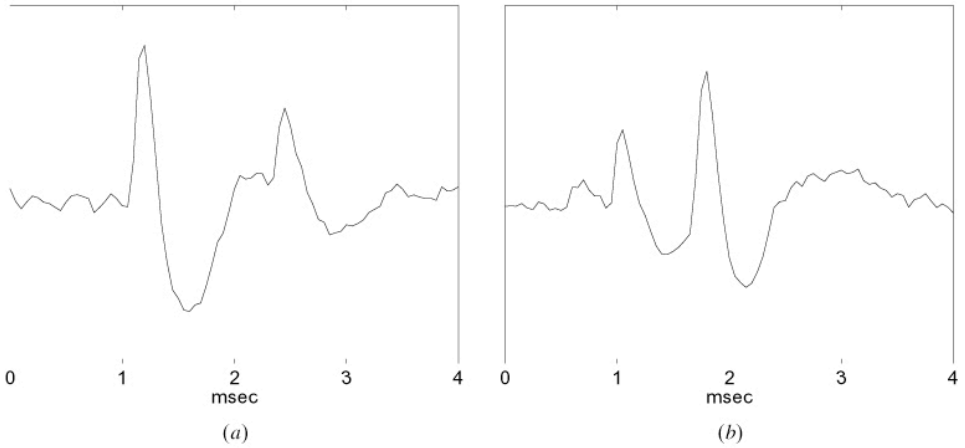

Figure 5. The peak level of the neuron of interest can change dramatically depending on the location and size of adjacent spikes.

Figure 4.13. Example of neural spikes, and an overlap
The peak amplitude of a spike can change dramatically when overlapping with adjacent spikes. Taken from Lewicki, 1998 [125].

As more computing power became available, more features of the spike were used: width, negative peak amplitude, etc. With modern computers it is possible to classify spikes using their entire waveform (several tens of samples). This led to the most common class of spike sorting algorithm, template matching [67, 151, 152]. These methods begin by constructing templates for the spike of each neuron (assuming they are stationary) from "clean" examples. These templates are then used to identify occurrences of each spike. The process requires two phases, a template creation phase, during which clean spikes are detected and classified, and an identification phase, during which units are identified using the templates. The template creation phase involves determining how many neurons are present, and is usually done using "clustering" algorithms. These algorithms detect clusters of similar

spikes in some feature space. We chose template matching using manual or k-means clustering for our analysis [125], the details of which are discussed in a later section.

Other methods include wavelet transformation and independent component analysis (ICA). Wavelet transform methods have shown a more efficient basis in which to classify spikes, but have not yet offered a solution to the problem of overlapping spikes [153]. ICA is an entirely different method that does not rely on templates, and instead assumes a linear mixture of N sources recorded on N recording sites [154]. The problem is then to find the mixing matrix, usually found using a mutual information algorithm, that can relate N unknown sources to recorded multichannel data. The algorithm has found success in optical array and EEG recordings, and has the advantage that overlaps are immediately resolved, and the independent components that come out of the algorithm are directly interpreted as neural spike trains. The difficulties with the algorithm come from the requirement that one must have at least as many recording sites as neurons, and that spikes must be recorded simultaneously (e.g. with no propagation delay) on all sites.

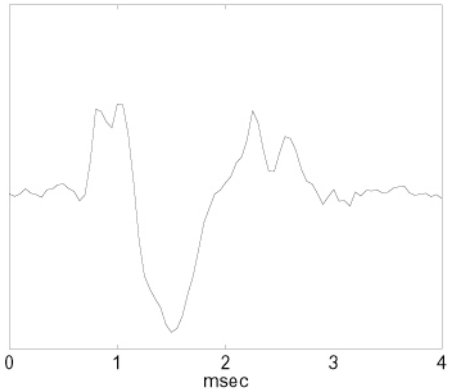

Figure 4.14. Spikes with a high degree of overlap
Spikes overlapping to this degree are difficult to correctly identify. The problem is even further magnified for greater than two units. From Lewicki, 1998 [125]. Template matching algorithms would have to ignore the spike during clustering, then correctly identify the two overlapping spikes, and then very accurately reproduce the spike timing, or subtract one of the spikes at an almost exact (subsample) timing precision.

The work by Gozani and Miller, using a template matching algorithm, has shown the best success in resolving overlapped units with real biological data [67]. Their algorithm created templates, and then iteratively subtracted identified spikes from the recording. Although the algorithm was published and could resolve the four largest giant fibers recorded on 8 sites, multiunit biological results were never published. They used linear filters based on each template that maximally respond to the desired neuron and reject the other templates and a noise sample. Several problems occur with this method. The biggest problem was that filters designed for slow, low amplitude spikes still produce large output when convolved with large amplitude spikes (Dr. J. P. Miller, personal communication). In addition, very close or simultaneous spikes present a problem for identification (Figure 4.14), and subtraction of a spike at an incorrect time point introduces more error to the waveform. Lewicki used a k-tree search algorithm to efficiently find a set of spikes and phases that could produce multineuron spike waveforms, but this suffered the problem that multiple combinations of spikes and phases could produce a match [125]. Some parsimonious algorithms can be used to minimize this problem, however.

4.7 Analysis of Cricket Data

4.7.1 *Spike detection and extraction methods*

The first step in spike train analysis is the detection of spikes. Spikes can often be detected with a simple amplitude threshold. In cases where the signal to noise ratio (SNR) is not adequate to detect low amplitude spikes, more complicated filters can be used. Convolution of the voltage record with a “Mexican hat” filter, which has a window size approximately the same length as a neural spike, produces a more sensitive detector. Another filter that has proven very good at detecting spikes under

nearly 0 dB SNR conditions is a non-linear energy operator (NEO) [155-157]. If we denote the operator as ψ, and the input waveform is x(t), the operator has the form

$$\psi(x(t)) = \left(\frac{dx(t)}{dt}\right)^2 - x(t)\left(\frac{d^2x(t)}{dt^2}\right).$$

The benefit of this filter is that its output is proportional not just to the square of the amplitude of the signal, but also to the square of the frequency of the signal. Thus it picks out low amplitude neural spikes due to their high frequency content (Figure 4.15). The output of the NEO is filtered with a Hanning window, to smooth the waveform, before being passed to a peak detection algorithm. All sixteen channels of the grid recording were filtered with the NEO, peaks were detected in the output, and the result stored in a Matlab data structure.

At this stage, since we are looking for clean examples of spikes from which to construct templates, we decided to note the length of time spent above threshold as an indicator of spike cleanliness.

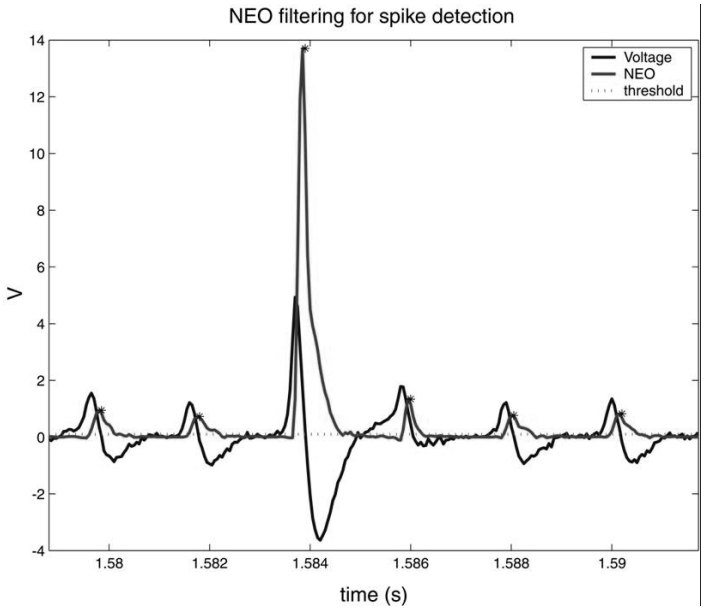

Figure 4.15. Spike detection using a NEO operator
Readily thresholdable monophasic peaks result from filtering with the NEO operator. Especially useful in cases of low SNR.

Spikes that occur near each other in time produce superposed peaks in the NEO filter output, and these peak superpositions tend to remain above threshold for a longer time than those due to single clean spikes. The peak times were taken as the potential spike time, and the length of time spent above threshold on each channel noted for use as a measure of spike cleanliness. Each potential spike time was recursively compared with those on the next channel, and cases where spikes consistently propagated within 0.5 ms from channel to channel across a user definable subset of the channels were extracted. The standard deviation of the width of the NEO peaks of each spike (variations in width from channel to channel) was computed, and spikes of large variation were discarded. Large variation in width of the NEO peak across channels usually corresponded to a faster or slower adjacent spike colliding with the current spike, elongating its waveform. Isolated spikes propagated from channel to channel with very little change in width of their filter output. Thus, spikes with a relatively large standard deviation were discarded. The remaining clean spikes which have peaks that propagate across all the selected channels with reasonable delays are then extracted (Figure 4.16). Figure 4.16 shows the first six spikes extracted from the cricket grid data shown in Figure 4.12. Because of the relatively large amount of time it takes for spikes to propagate across the grid (up to 5 ms or more), these long waveforms tended to contain adjacent spikes. In order to minimize noise in the classification, the waveform outside the immediate spike was multiplied with linear ramps to zero to remove other activity. This produces the clean spike waveforms seen in Figure 4.16., which is an example of a “catalog” of potential spike waveforms.

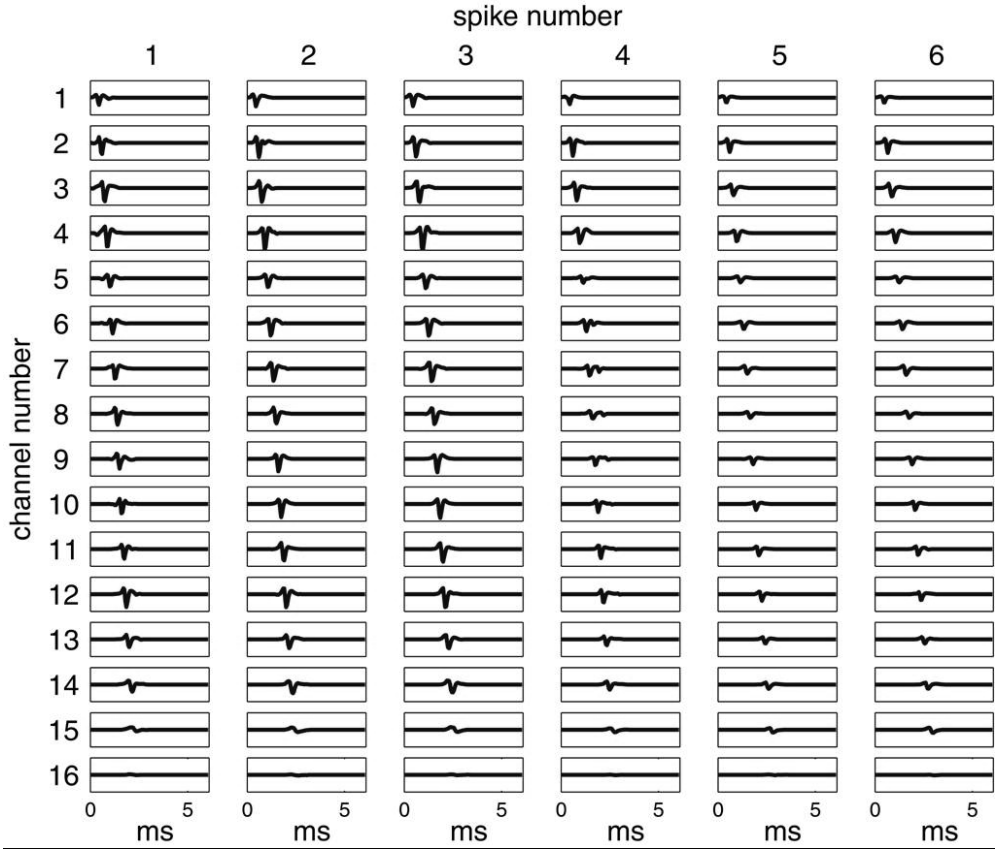

Figure 4.16. An example spike catalog
The first six spikes of the spike catalog constructed for the cricket ventral nerve on the bridge array experiment. Entire catalog consisted of ~1000 spikes. Note that spike #4 actually contains a coincidence of two spikes. This spike would either be discarded due to large deviation in NEO filter width, or occur as an outlier in the cluster analysis.

4.7.2 *Spike classification*

Having constructed a catalog of observed spikes, the next task is to determine the number of neurons present, and which spikes are due to which neuron. As discussed, a plethora of methods exist, for both single and multichannel waveforms. The most general methods classify spikes based on their entire waveform, whereas other methods may only use some salient features: positive peak amplitude, negative peak amplitude, width, etc. Whatever the feature set, each spike must be scored in some manner, and spikes with similar scores grouped as those originating from the

same neuron. The processing power available in a modern PC makes it possible to classify spikes based on their entire waveform in relatively short time. However, the question of how to incorporate multichannel information into the classification remains. One technique used by many investigators is to form a high dimensional space of spike features across all the electrodes, and then manually circle clusters of similar spikes in several 2D projections of the data [158, 159]. After helpful discussions with Dr. M. Levene, we decided the simplest method for our analysis would be to form a larger waveform that contains information from all the channels, and perform a clustering on these concatenated data (Figure 4.17). As Figure 4.17 shows, the result is a longer waveform that contains the spike on the first recording site, followed by the spike on the second recording site, etc. A window in time that is long enough to accommodate the slowest spike is determined during the spike extraction phase, and this length of time is extracted from each channel, ensuring that all conduction information is preserved when forming the concatenated waveform. This method has the advantage that it preserves all the information about changes in waveform shape across channels, as well as differences in conduction velocity. The disadvantage is that the concatenated 16 channels waveforms are very long (~1000 points) and analysis of more than a few thousand spikes begins to take hours.

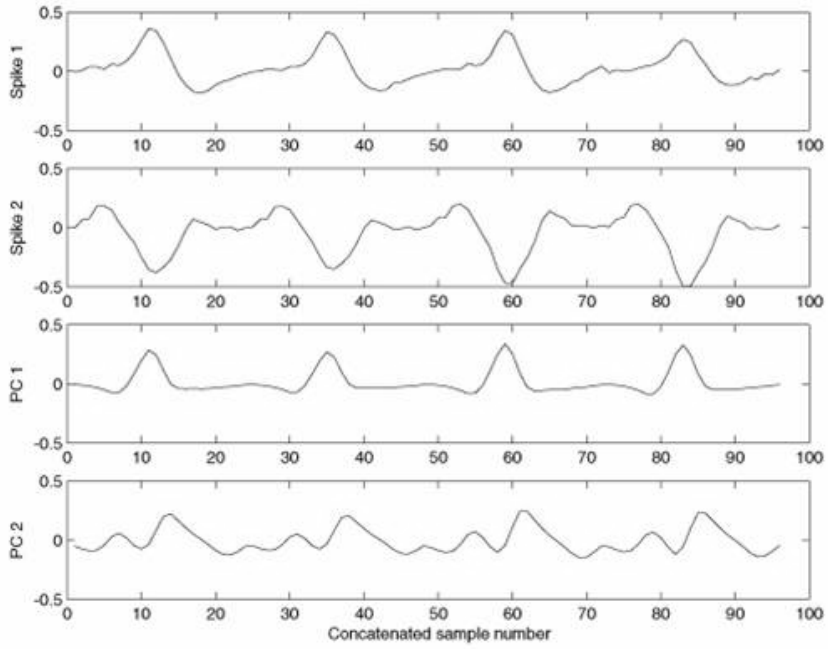

Figure 4.17. PCA on concatenated spike waveforms
The waveforms from each channel in a multichannel spike are concatenated to form a single waveform for a single spike recorded on multiple channels (top two traces). PCA is then carried out on the catalog of concatenated waveforms. Two example concatenated four channel spikes are seen in the top two panels, and the first two principle components derived from PCA on the entire data set are shown in the lower two panels.

Once the concatenated waveforms have been computed (Figure 4.17), we need an appropriate method to "score" spikes. Principal component analysis (PCA) is a popular statistical method, and one that we chose to apply to our concatenated waves. PCA finds the eigenvectors of the covariance matrix of the data. In this case, the columns of our data matrix consist of our concatenated spike waveforms. The computed eigenvectors, called the principal components, define a space in which the axes point in directions of maximum variation of the data. The earlier principle components account for most of the variation in the data, and later ones perform small

corrections on the spike waveform (Figure 4.17). The PC vectors provide a good basis in which to discriminate between sets of similar spikes.

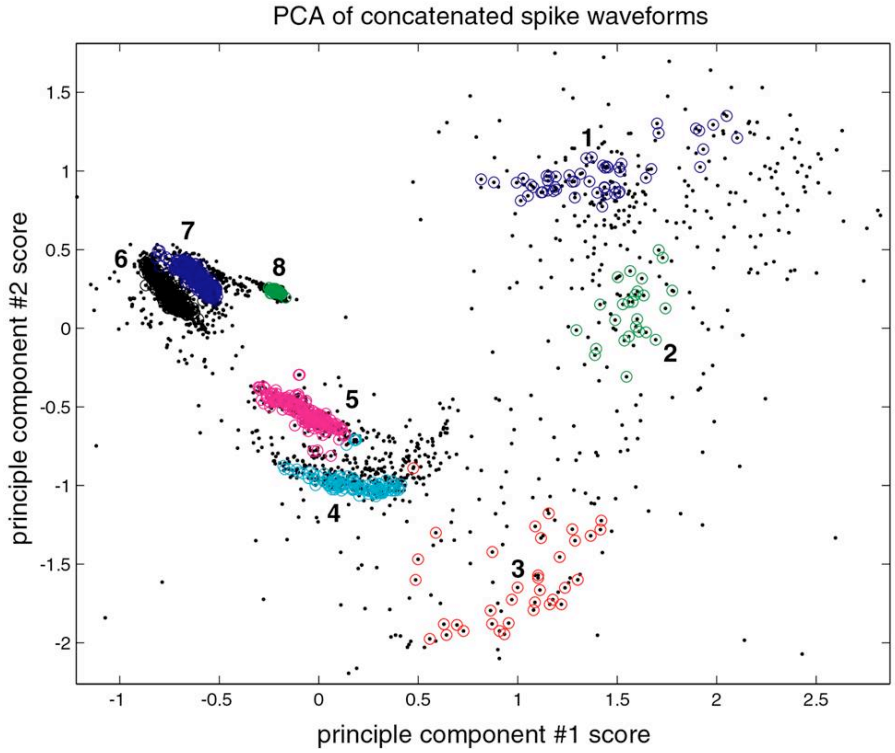

Figure 4.18. Results of clustering concatenated spike waveforms from the cricket data
A scatter plot of spike scores on the first two principle components, for spikes detected in the 40 second wind puff recording on the bridge array. Eight clusters are readily visible. Note that this is a projection of the two most significant PC components, and that the points may be distant from each other in other dimensions.

Once principle component vectors have been calculated for a given set of spikes, each spikes' score (dot product) with each PC vector is computed (Figure 4.18). A scatter plot of the scores for the cricket grid data, corresponding to the catalog of spikes of which the first six are seen in Figure 4.16, is seen in Figure 4.18 (total ~2500 spikes). Each point on the plot is the score of a concatenated spike waveform from the catalog. If we make the assumption that the spike shape and conduction velocity of each neuron are roughly stationary, then the number of dense clusters in

our scatter plot corresponds to the number of neurons present in the recordings, and each cluster represents spikes from a single neuron. This assumption is a reasonable one for non-bursting neurons, whose spike shape and conduction velocity are generally thought to vary by about 1%. The problem then becomes determining how many clusters (and hence neurons) are present, and which cluster to assign each spike to. A number of methods exist for this. Put another way, the overall goal is this: given a set of data points in which there are several dense "clouds" of closely spaced points separated by less dense regions, how do we decide how many "clusters" to group the data into, and with what cutoff criteria do we assign points to each cluster? This procedure is called "cluster cutting". Users can simply draw lines circling each cluster, manually, or an automated algorithm such as K-means clustering can be used [125]. We found the cricket grid data formed several distinct clusters (Figure 4.18), even in a simple 2D projection, and so decided to cluster the data manually. When visualized in 3D, the sparse regions containing clusters 1, 2, 3, were separated in elevation.

A user interface allowing the operator to select and subsequently plot spikes from the scatter plot of principle component scores was written, and used to determine that eight distinguishable clusters of spikes were present. Many of the outlying spikes in the plot are undetected superpositions of spikes, or simply noise artifacts. By manually sifting through regions of the scatter plot, and examining the spikes in that region, it was possible to determine that eight basic spike shapes were present. Spikes at the center of each of the clusters were chosen, and all spikes within a suitable Euclidian distance of these centers were taken as waveforms to be included in the template for that neuron. That is, once the "clouds" of spikes that that came from each putative neuron were identified, a spike at the center of each cloud was chosen, and all spikes within a certain "radius" of that center, were assigned that that cluster. The reason the assignment does not look circular in Figure 4.18 is that the distances were

calculated in the full high dimensional (~1000) space of PCA scores, not just the first two (which Figure 4.18 illustrates). The cutoff distance for spike assignment to each cluster was enlarged until clusters had a reasonable number of spikes, or until the cluster began to appropriate outliers or spikes from a neighbor. The colored circles in Figure 4.18 denote the assignment of a spike to a particular cluster, and those spikes that are uncircled were left out as outliers.

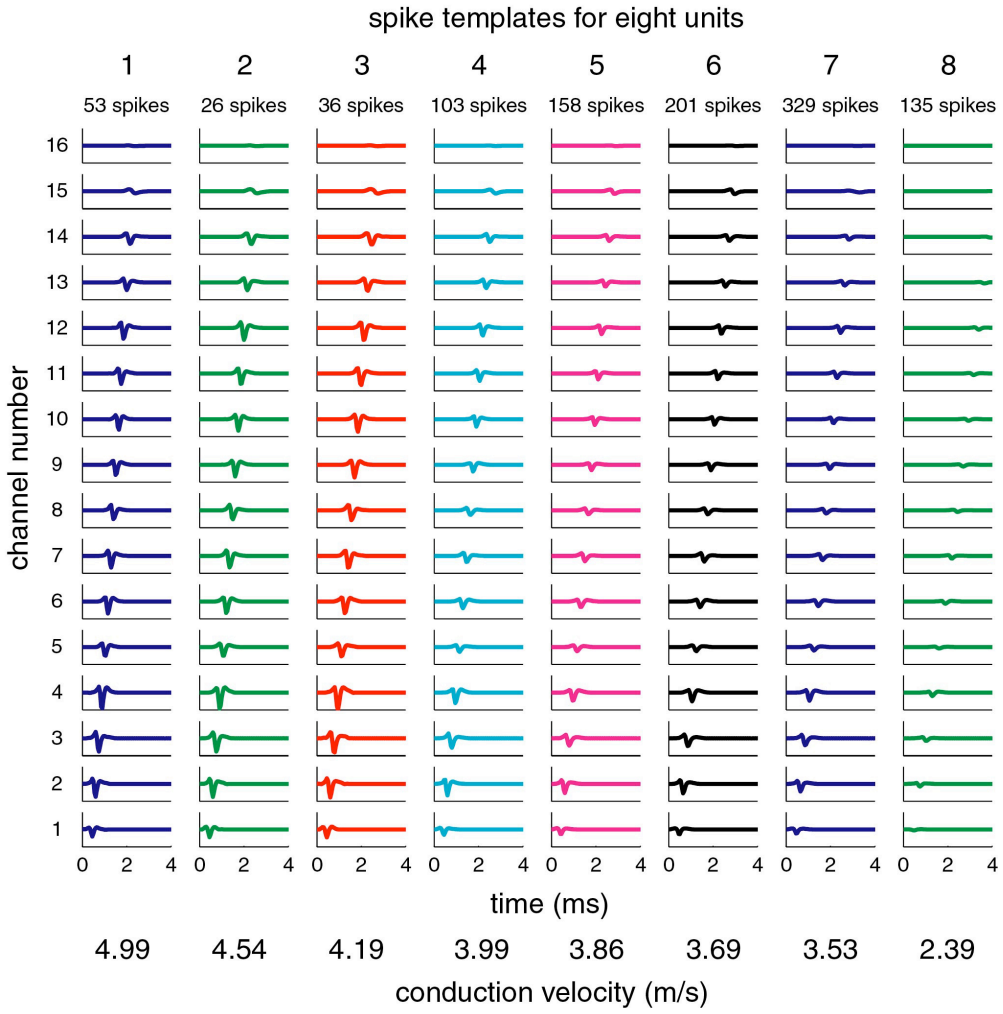

Figure 4.19. Templates for the eight neurons
The results of averaging the spikes in each cluster seen in Figure 4.18. Colors in this figure correspond to colors in Figure 4.18. Note the difference in conduction velocity and amplitude.

4.7.3 *Template creation*

We now have an assignment of individual spikes to clusters, and can form templates from the clusters of similar spikes. The average waveform was computed for each of our eight clusters, and each individual spike time shifted to minimize Chi squared distance from this average, reducing jitter in extracted spike time. The final spike template was the average waveform of these jitter corrected spikes, and the templates computed for the cricket grid data are seen in Figure 4.19. Conduction velocity was computed for each spike using the average time required for the spike to propagate from one channel to the next, and the known separation of recording sites. The mean conduction velocity and associated standard error for each neuron were then computed from the conduction velocities of the spikes in each cluster, and are listed at the bottom of Figure 4.19 and in Table 4.2. The templates have varied conduction velocity and peak amplitude, features that will be critical in resolving spike overlaps, in a manner similar to Gozani and Miller. In addition, they provide information to use in identifying neurons from anatomy. For clarity, the templates were cut off at 4 ms, although the slowest neuron, number eight, arrives at channel 15 after this time. To verify that the low amplitude of the spikes recorded on channels 15 and 16 was a biological and not electrical phenomena, the preparation was reversed on the grid array at the end of the experiment. Similar data propagating in the reverse direction were observed (data not shown), confirming electrical continuity of channels 15 and 16. Dispersion of the spikes due to their varied conduction velocity is readily seen in Figure 4.20, where spikes have been aligned to their peak on the first channel.

Table 4.2: Spike conduction velocity and timing

Template	Conduction Velocity (m/s)	Error	Timing %	N
1	4.99	0.120	83	53
2	4.54	0.056	54	26
3	4.19	0.080	25	36
4	3.99	0.060	42	103
5	3.86	0.033	85	158
6	3.69	0.049	19	201
7	3.53	0.066	59	329
8	2.39	0.045	51	135

The change in stimulus direction was enough to qualitatively determine that four of the clusters of spikes elicited depended on stimulus direction, and that the system was working as intended. Table 4.2 indicates the percentage of spikes for each template that occurred during the first stimulus direction. The remainder will have happened during stimulation in the second direction. Neurons one, three, five and six show strong directional preference, having 83%, 25%, 85%, and 19%, respectively, of their spikes occurring during stimulation in the first direction. Thus excitation of some of the neurons we recorded from changed with wind direction, indicating that not only are these neurons wind-sensitive, but that they have a directional preference, as we expect.

From the anatomy, we note that there are several units with area in the 200 – 400 square micron range. We expect to see two or three units with larger, faster spikes than these. Looking at the spike conduction velocities and number of spikes detected in Figure 4.19, we see that this holds true. There are few examples of the largest, fasted spikes (4.5 and 4.9 m/s), and large numbers of the slower spikes (3 – 4 m/s range). It is possible that some of the templates with large numbers of spikes are actually two units with very similar conduction velocity.

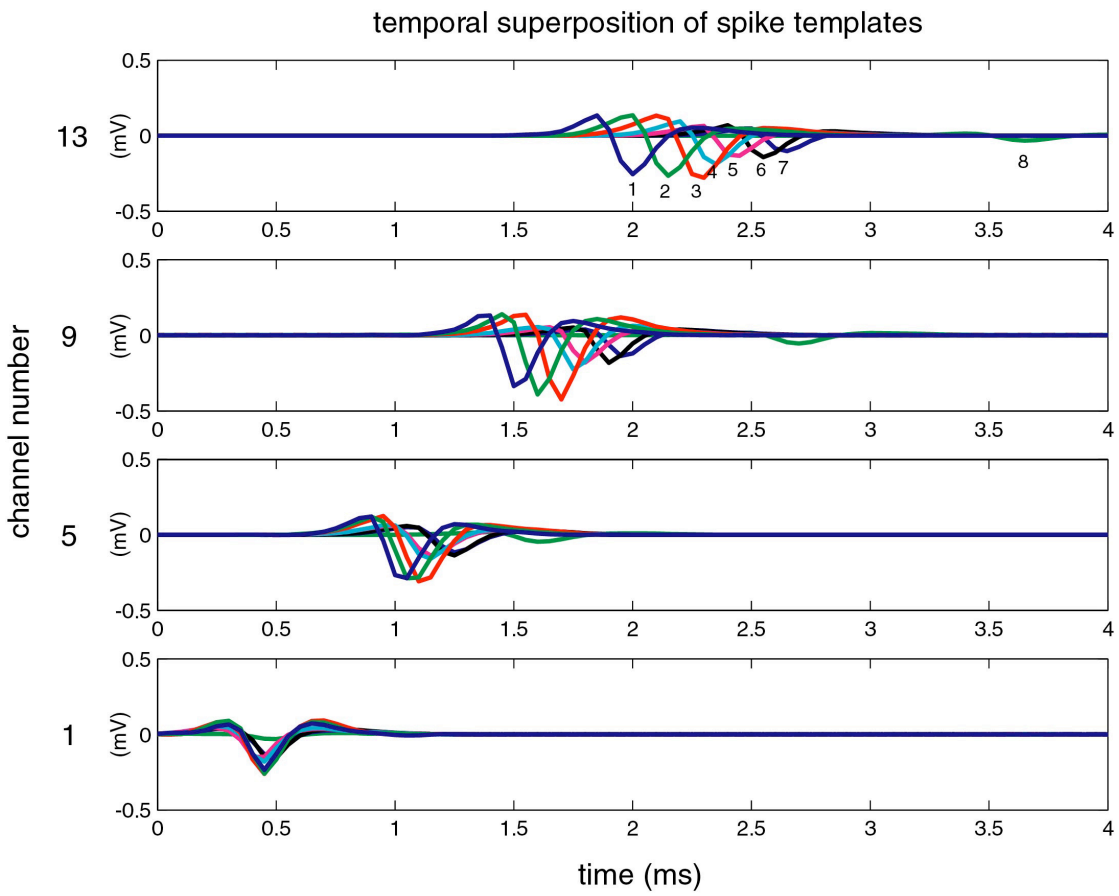

Figure 4.20. Overlay of spike templates
Spikes are aligned by their peak on channel 1. Note the dispersion due to differences in conduction velocity. A subset of the bridge array channels are shown, those indicated by arrows in Figure 4.11.

The noise inherent in the biophysical mechanism of spike conduction results in conduction velocities of a single neuron being consistent only to within about 1%. Examining Table 4.1 shows two axons in the right hemi cord were measured to have areas of 286 and 287 square microns, respectively. This difference of 0.3% would make these axons indistinguishable based solely on information from our conduction measurement multielectrode. The small difference in conduction velocity is illustrated more clearly in Figure 4.20, where all the templates are plotted with their channel 1 spikes aligned in time. Thus, we cannot definitively identify all of the axons in the

cricket preparation *in situ* from measurement of conduction velocity alone. Whatever method or combination of methods we use to identify neurons from extracellular waveforms is going to require rigorous verification via simultaneous intracellular recording, and in a later section we discuss revised versions of the grid array for this purpose.

4.7.4 *Clustering of transfer function ratios*

An elegant technique for clustering spikes that shows promise in resolving spikes of similar shape and conduction velocity has been formulated by D. Rinberg, H. Davidowitz, and N. Tishby, and is currently in press for publication (N. Tishby, personal communication). This method is easy to implement, and we use it here to test whether the clusters in our data that have large numbers of spikes arise from multiple units of similar diameter. The method avoids clustering the spike waveform directly, and instead uses a ratio of transfer functions between neurons and recording sites.

Briefly, we define a linear transfer function that relates the voltage recorded at each multielectrode site to the spike waveform generated by the neuron. The analysis is more easily carried out in the frequency domain. If we denote the frequency spectrum of the spike of the j^{th} neuron $S_j(\omega)$, and the transfer function between this neuron and recording site μ as $H_{\mu}^{j}(\omega)$, then the voltage recorded at site μ is given by:

$$V^{\mu}(\omega) = H_j^{\mu}(\omega) S_j(\omega)$$

If we now take the ratio of the voltage recording at two sites μ and ν, we have

$$T_j^{\mu\nu}(\omega) \equiv \frac{V^{\mu}(\omega)}{V^{\upsilon}(\omega)} = \frac{H_j^{\mu}(\omega) S_j(\omega)}{H_j^{\nu}(\omega) S_j(\omega)} = \frac{H_j^{\mu}(\omega)}{H_j^{\nu}(\omega)}$$

This quantity is the ratio of the transfer functions between neuron j and recording sites μ and ν. Importantly, we note that the spike waveform from the cell has divided out. This means that this quantity is invariant to changes in the spike shape—even spikes

from a single neuron whose shape and/or amplitude vary during a burst will have stationary transfer function ratios. In addition, because we are discriminating based on properties of the transfer function ratio and not the spike waveform, spikes of similar shape and conduction velocity from different neurons may be discriminable.

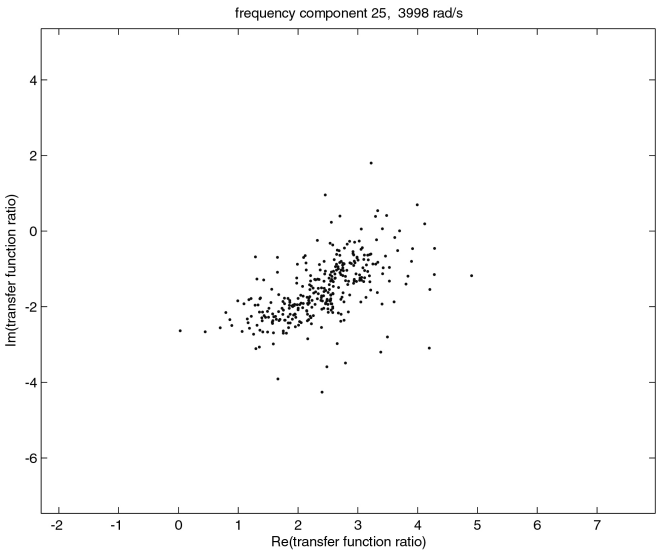

Figure 4.21. Results of clustering transfer function ratios for spikes in cluster 7 A plot of the real versus imaginary parts of spike transfer function ratios at a single frequency. No obvious clustering appears in this ratio of transfer functions for channels 4 and 8, suggesting that these spikes originate from a single axon.

In order to test our hypothesis that the large clusters in our cricket data may contain spikes from multiple neurons with similar size and conduction properties, we carried out this calculation on the 329 spikes in cluster number 7 (Figures 4.19-20). We compute the fast fourier transform of all the spikes, and then divide the spectra from recording sites 4 and 8, to produce our transfer function ratios. These sites were chosen as they are 2 mm apart, approximately equal to the separation used by Rinberg, and have a good signal-to-noise ratio. The transfer function ratio is composed of 122 frequency components, and in Figure 4.21 we plot the real versus imaginary parts of the transfer function ratio at the 25^{th} frequency component, corresponding to $\omega \cong 4000$

rad / s. The other frequency components produced similar plots. The data *do not* split into additional clusters when classified using transfer function ratios, suggesting that all the spikes in this cluster do indeed come from a single neuron. This is an encouraging result, suggesting that we have not confused two similar neurons. We still require definitive verification of these promising data, which we can obtain using simultaneous intracellular recordings.

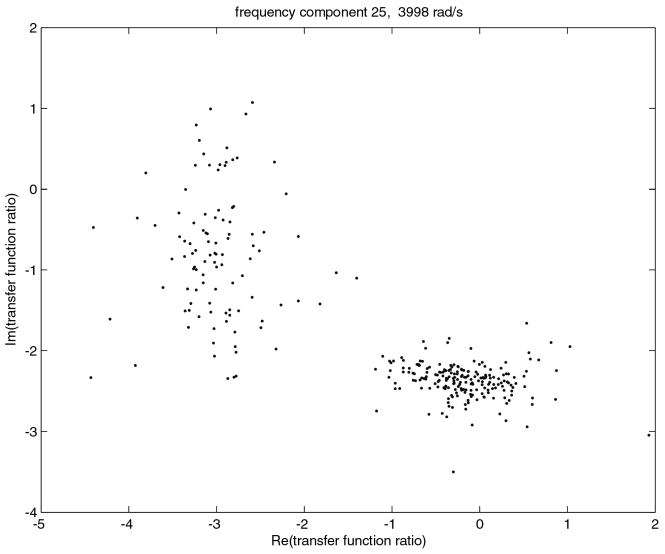

Figure 4.22. Results of clustering transfer function ratios for spikes in clusters 4 and 6
A plot of the real versus imaginary part of the transfer function ratios at a single frequency. Here we plot values for spikes in both clusters 4 and 6. The data form two distinct clusters, showing that the method of analyzing transfer function ratios capably resolves spikes from different neurons. This shows that the technique works, and supports our contention that the spikes in cluster 7 originate from a single neuron.

To verify that our method of clustering transfer function ratios is capable of resolving different spikes, we repeat the calculation for a set of spikes known to contain spikes from two neurons. We extract all the spikes in clusters 4 and 6, which clearly originate from distinct neurons, pool them together, and repeat the computation of transfer function ratios. We compute the ratio of the same channels, 4 and 8, and

plot the real versus imaginary part of the transfer function ratio at the same frequency, ~ 4000 rad/s. The result is seen in Figure 4.22. Two distinct clusters are immediately visible, demonstrating that the transfer function ratio method can clearly resolve different neurons. This control demonstrates that our computation is correct. We can conclude, then, that either all of the spikes in cluster 7 originate from a single neuron, or they originate from two neurons with virtually identical spike shape, conduction velocity, and transfer functions to channels 4 and 8. This similarity seems highly unlikely, and as such we conclude that we have templates for 8 different giant interneurons, a large fraction of the complete wind sensitive ensemble (~12 neurons).

4.7.5 *Accuracy of spike detection using the spike templates as linear filters*

Having addressed the question of neuron identity in our cricket spike templates, we now turn to the second stage of our spike sorting algorithm, using the templates to resolve spike firing times. In order to determine utility of our multielectrode in deconvolving multiunit data, we carry out spike detection on randomly generated spike trains. We generate firing times for each of our 8 neurons either at specific times or using random numbers taken from a Poisson distribution, being careful to eliminate any firing times which are within a user-defined refractory period. The corresponding single neuron spike waveforms are then added to the total 16 channel simulated waveform at each firing time, and as a final test parameter we can add Gaussian white noise.

The spike detection procedure we chose to use in this test is simply linear filtering. We cross-correlate a chosen spike template with the simulated data, take the sum of the cross-correlations for each channel, and threshold the resulting filter output. Each of these cross-correlations produces a positive peak when the spike is overlaid upon itself with zero lag, and the sum of all 16 channels produces an even

larger peak when the spike waveforms have zero lag across all channels. Thus we have a single waveform filter output that is selective for our spike shape and conduction velocity. The method of Miller et. al. [67] extended this technique by normalizing the amount of energy in each frequency component of the filters. We discuss this approach in the chapter summary.

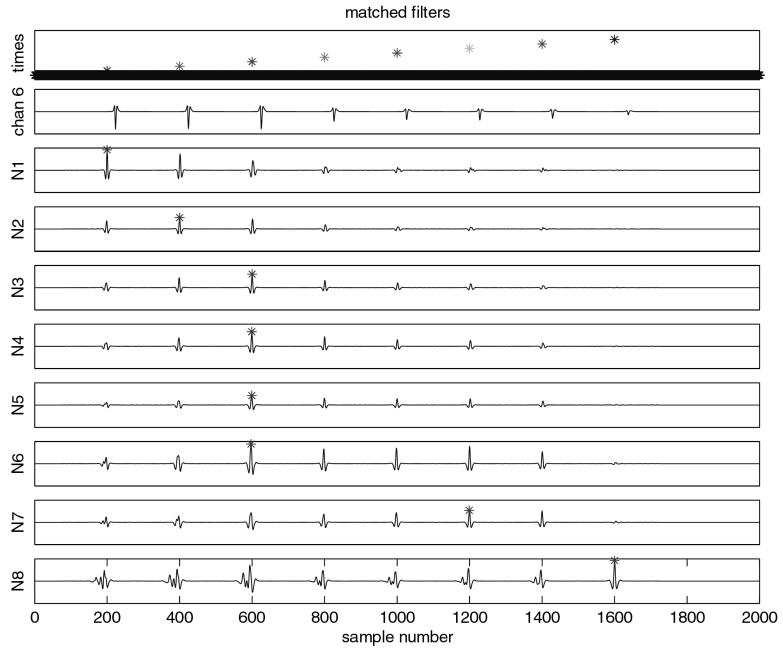

Figure 4.23. Matched filters for spike detection
Testing of matched filters on simulated data containing single isolated spikes. Upper trace, firing times of neurons 1-8, next trace down, channel 6 of the generated waveform, traces N1-N8, the output of the filter for each neuron operated on the full 16 channel data. Note that the filters for neurons 4, 5, and 6 have a maximum response to spikes from neuron 3 (the largest spike), and that the filter for neuron 7 responds most strongly to a spike from neuron 6.

In Figure 4.23 we have generated 16 channel data with each neuron firing a single isolated spike. Only channel 6 of the data is shown, but all 16 were used in computing the filter output. The firing times of each neuron (1-8) are shown as stars in the uppermost trace, channel six of the data is the next trace, and traces N1-8 are the

output of the filter for each neuron operated on the data. The peak of the filter output is denoted by a star. We note that the filters for neurons 4, 5, and 6 respond most strongly to the spike from neuron 3, and the filter for neuron 7 responds most strongly to a spike from neuron 6. What we desire, however, is for each filter to respond maximally to its own spike. The problem arises because although the filters for 4, 5, 6, and 7 are selective for their own slower, smaller spikes, the large amplitude of the incorrect spike outweighs the difference in conduction velocity. That is, even though spike 3 is faster than spike 4, and thus they do not overlap precisely when computing the cross correlation, the large amplitude of spike 3 causes the output of the filter for just the smaller part of the overlap to be greater than the output for spike 4 cross correlated with itself. This is due, in part, to the difference in conduction velocity being very small. As can be seen in Figure 4.20, the difference in conduction velocity is only a few percent.

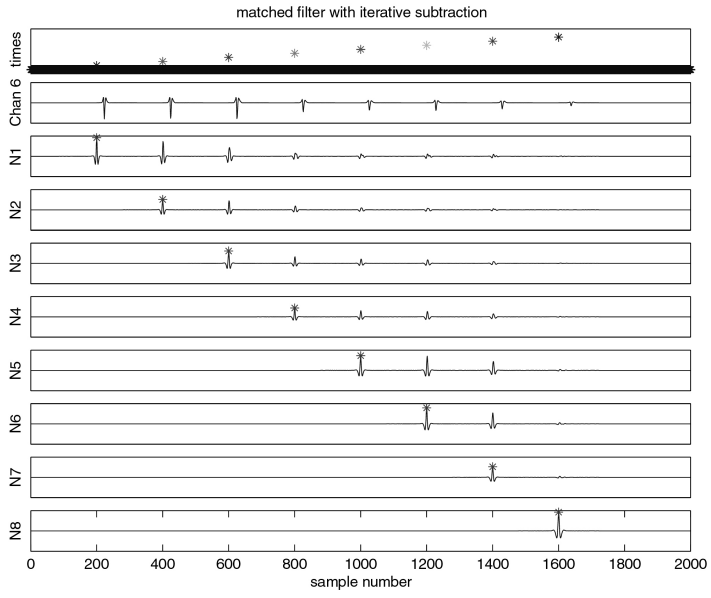

Figure 4.24. Matched filters with iterative subtraction
The result of using matched filters moving from large spikes to small spikes. The largest spike is filtered first, and detected occurrences are subtracted out. This prevents the filters for smaller spikes from incorrectly responding to these large spikes.

We can recover correct identification of all eight neurons by making a simple addition to the algorithm. Beginning with the largest spike, we iteratively subtract detected spikes from the waveform. This removes the large spikes before they are incorrectly detected by the filters for closely neighboring smaller/slower spikes. The result of this is seen in Figure 4.24. The filters are seen to maximally respond to their own spike, in the absence of larger spikes.

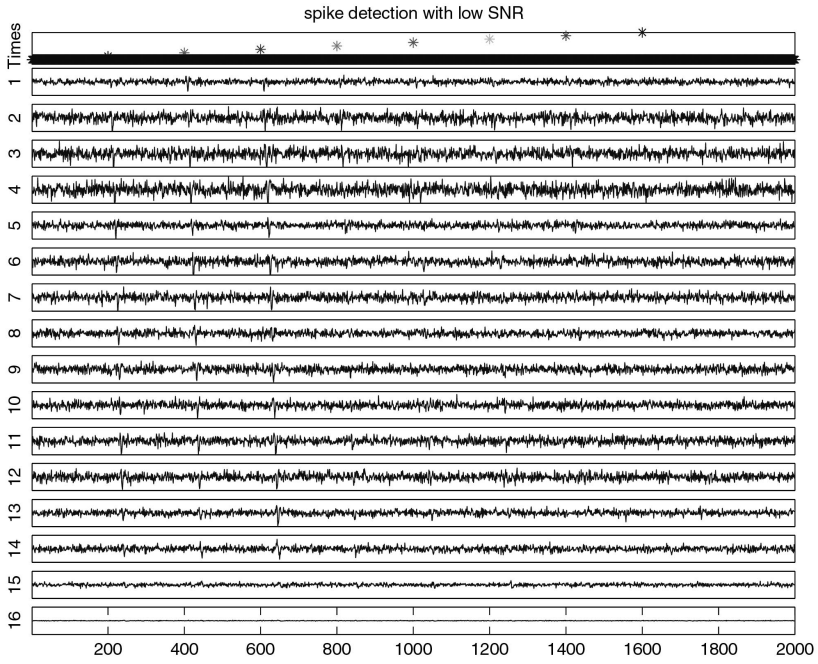

Figure 4.25. Simulated data with very low SNR
Simulated sixteen channel data with a single spike from each neuron and low SNR. Spikes from neurons 1, 2, and 3 are visible above the noise, whereas those from later neurons are not.

We first test the noise performance of the spike detection algorithm. Using the same sequence of isolated spikes, we add Gaussian white noise resulting in an overall signal to noise ratio (SNR) of 0.5. At this level, spikes from neurons 1, 2, and 3 are visible above the noise, but those of the other 5 neurons are not. The simulated data are seen

in Figure 4.25, and the result of applying the iterative matched filters is shown in Figure 4.26.

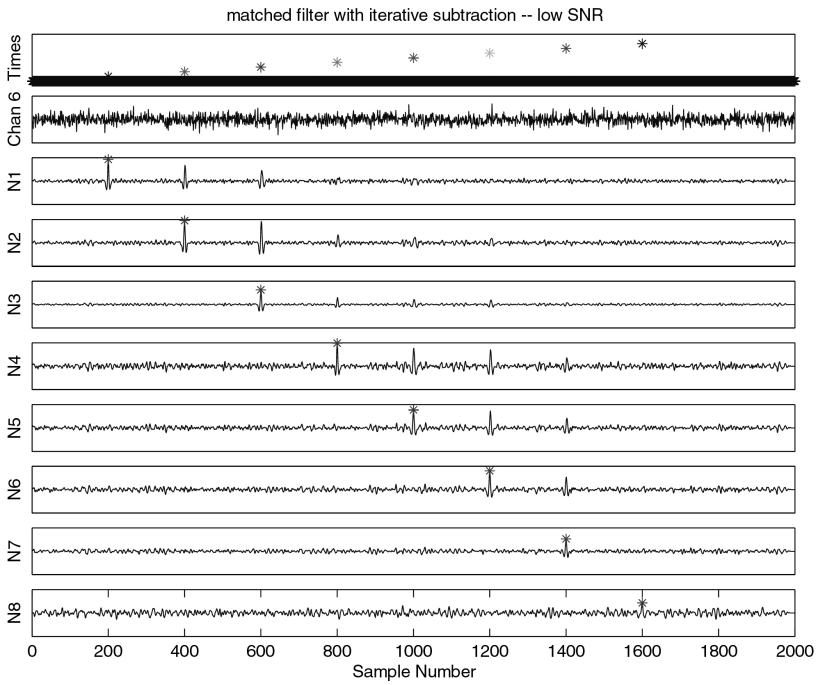

Figure 4.26. Results of matched filtering of data with low SNR
While the filter output is beginning to get noisy, the matched filters are able to detect isolated spikes from even the smallest neuron, in raw data having a SNR of 0.5.

The performance of the detection algorithm on isolated spikes is very good. If the amount of activity in the nerve cord during an experiment was relatively small, this detection algorithm could provide near perfect detection of these eight units. If, for example, one was using a spike-triggered averaging technique, such as that used by Rinberg et. al. [160], the stimulus is a relatively low-level 1/f noise, and the spike trains may be of sufficiently low activity to be very accurately (90%) sorted. One of the problems with this type of analysis, however, is that although 1/f noise may be useful in roughly determining what stimulus a neuron is “looking for”, it is not necessarily the biologically relevant stimulus. It is likely that biologically relevant

stimuli, especially in the case of detecting an approaching predator, are more likely to have short timescales on the order of a few or perhaps tens of milliseconds. We would expect a burst of activity from many neurons during this critical period of stimulation. This period is when the neural system is likely to be realistically "pushed to the limit", performing its most demanding discrimination tasks that have been selected for over millennia. As such, we would like to know the performance of our device in resolving firing times during large amounts of activity. Measurement of the type of activity in the system during naturalistic stimulation is one of the guiding principles of neuroethology.

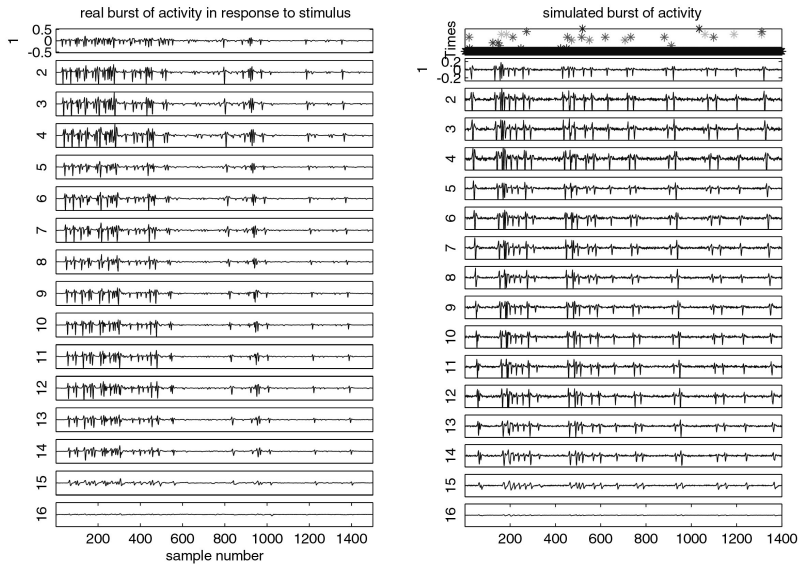

Figure 4.27. Comparison of real and simulated bursts of multiunit activity
The data in the left channel show a single elicited burst of activity in the cricket nerve cord, and the panel at right shows a spike train generated using high (~50-80 hz) Poisson distributed firing rates for the larger neurons and slightly lower (20-40 Hz) rates for the smaller units. The generated data qualitatively resemble the real burst.

Simulated data were generated using random firing times taken from a Poisson distribution, corrected for a 2 ms refractory period. With average firing rates of 50-80 Hz for the larger units and 20-40 Hz for the smaller units, the simulated data showed

good resemblance to the real bursting data, as can be seen in Figure 4.27. A more accurate model would have variable firing rates, with high probability for several neurons during a short time interval, followed by low probability, but the data generated here were seen to have large numbers of overlapping spikes, the most crucial factor in sorting more realistic data.

Table 4.3: Accuracy of spike sorting

n	%	FP %
1	90	5
2	80	5
3	86	2
4	87	19
5	83	87
6	11	108
7	12	56
8	97	1

Data were generated and the sorting algorithm carried out until each neuron had at least 500 spikes. The percentage of correct identifications and false positives are seen in Table 4.3. The sorting accuracy is adequate for the 3 largest and fastest templates, as well as the last (very slow) template. Close examination of the waveform after each step reveals that the problem in identifying neurons 4-7 is twofold. The jumbled

waveform causes imperfect detection of the spike firing time of even the largest neurons, and as a result the subtraction process introduces error in the data waveform. The accumulation of these errors after the subtraction of 3 large waveforms is enough to obscure accurate detection of templates 4-7. Additionally, the templates for neurons 4-7 are very similar in spike amplitude and conduction velocity.

The fact that we can resolve four units with greater than 80% accuracy in data that contains largely overlapping activity is important. Noting that the slowest and smallest neuron was readily recognized suggests that the presence of several units with similar amplitude and conduction velocity is the limiting factor. In a system with fewer or more spread out units, the resolution would be markedly better. Unfortunately, in many systems it is the case that having axons with similar conduction velocity is important, if not crucial, for further comparative processing by the central nervous system (CNS). However, in systems with distinct conduction velocities and lower activity levels, the algorithm can be expected to perform very well.

4.8 Improvements on the conduction measurement devices

The grid design of multielectrode provided a means to have multiple, densely spaced longitudinal recording sites that are adequately isolated from each other and a common ground plane. Resolving four of the giants in the cricket nerve cord with a single monolithic device will greatly aid in further research on the system. The geometry was restrictive, however, in the need to dissect free the nerve cord such that it could be placed directly on the device. The extensive dissection and fragility of the resulting preparation limit the ability to conduct long term experiments, and to apply long term stimuli. The design parameters for next generation devices were to achieve the same density and isolation of recording sites over a similar length of nerve cord,

but to free the device from the substrate, allowing for a more intact preparation. This would also facilitate penetration of cell bodies with an intracellular electrode at the terminal ganglion. A “ladder” shaped multielectrode of much smaller dimension was developed that could simply be slipped underneath the nerve cord, and is discussed in the following section. The bulkiness of the rudimentary interconnect (soldered ribbon cable) between the grid electrode and amplifiers was also a space and reliability issue. The ladder electrode needed to be maneuverable in a standard manipulator whilst all 16 channels were connected to the recording apparatus. A novel interconnect was developed that relieved the need for wire bonding or soldering of each individual device. Finally, the troublesome wiring harness connecting all multielectrode traces to the inputs of rack mounted amplifiers was replaced with a custom designed, miniature, battery powered surface mount amplifier.

4.8.1 *Ladder multielectrode geometry*

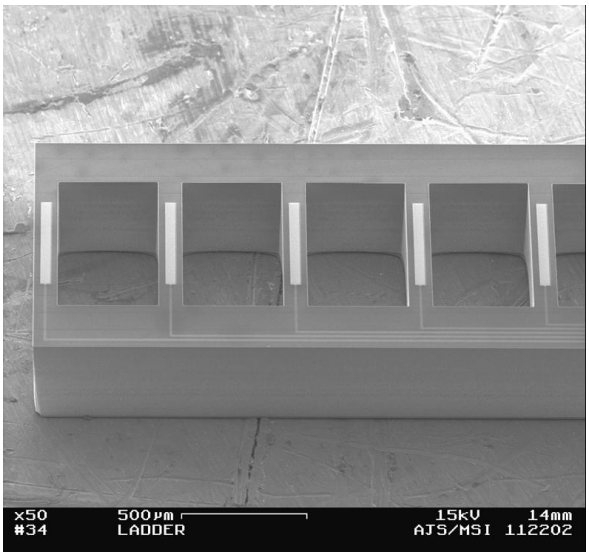

Figure 4.28. “Ladder” multielectrode array
This design of electrode permits measurement of action potential conduction across 16 recording sites spaced 500 microns apart, spanning 8 mm. The device is less than 1 mm wide, and has a box-car structure to ensure the nerve cord is in bath between recording sites.

The device seen in Figure 4.28 and 4.29a is the miniaturized conduction measurement multielectrode. This 'ladder" contains recording sites that are 40 x 400 micron rectangles, spaced by 500 microns. Sixteen such sites span 8 mm, as compared to the full 10 mm of the grid. This small difference was due to finding that rarely was a full cm of nerve cord available without damaging the prep, and that over the last 2 mm of the cord the action potential amplitude was largely attenuated, probably due to thinning of the axons in preparation for entry to the thoracic ganglion. The box-car shape of the ladder is designed such that the nerve cord can be draped across recording sites, while between them it is free to be in saline bath. This alleviates the surface shunting problem, permitting normal action potential propagation, and maintains the health of the nerve cord for longer periods. The ladder is approximately 1 mm wide, permitting it to be maneuvered underneath the nerve cord with the abdominal cavity largely intact. A slit can be cut in the ventral surface of the abdomen, the nerve cord dissected free of fat and muscle tissue, and the "ladder" slid into place.

4.8.2 *Instrumentation – gold bellows interconnect*

While the interconnection schemes used in previous devices, ultrasonic wire bonding or conductive epoxy, were adequate, they were time consuming (each channel of each device had to be manually connected), unreliable (48 solder connections), and unwieldy (chip carrier ~ 1x0.5x0.5 inches, and the grid mounted on a slide ~ 2.5x0.5x0.1 inch). This led to the design of a miniaturized interconnect with the following features: a) standard electrode holder size (7mm diameter rod), b) spring loaded electrical connections, c) automatic alignment of electrode and holder, d) reduced area of interconnect on the wafer. The electrode, holder, and interconnection scheme are illustrated in Figure 4.29. The interconnect area consists of a 4 x 13 mm rectangle (much smaller than previous devices, permitting more devices per wafer).

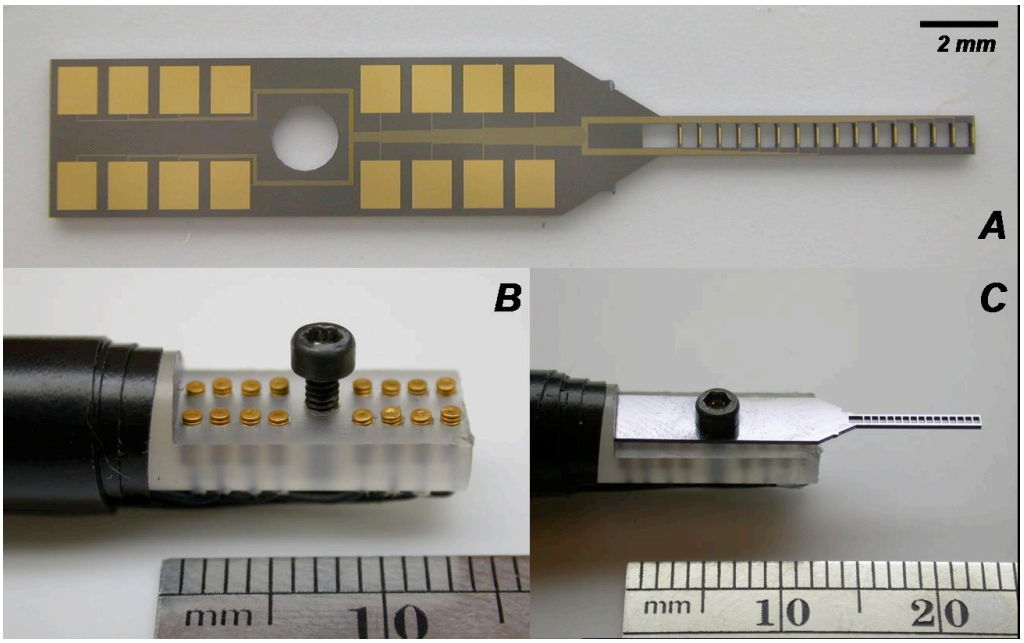

Figure 4.29. Gold bellows interconnection scheme.
A device designed for the second generation interconnect. Contact pads are spaced about a bolt hole (A). The holder consists of a machined flouropolymer rod with gold bellows in counterbored holes and a aligned threaded bolt hole (B). The device is bolted down onto the bellows (C) making contact.

Traces from multielectrode recording sites are run to large gold pads (~1 mm square) inside this rectangle and at precise known offsets from a central bolt hole. Chips are aligned to the holder via the bolt hole and the back edge of the electrode. The electrode holder and interconnect itself consist primarily of a machined fluoropolymer (Kel-F) rod. A flat was machined in the rod, and a M1.6 threaded hole is tapped in the center of the flat. Holes are drilled through the flat at offsets matching the chip layout with a 0.5 mm drill. These holes are then counter-bored 1.8 mm deep with a 1 mm end mill. Miniature Gold electroformed bellows (Servometer Inc., part #2500) soldered to 36 gauge hook-up wire were then placed in the counter-bored holes, with the wire continuing out the 0.5 mm hole. The bellows were 1 mm diameter, 2 mm in length, and thus had their contacts protruding just above the flat surface (Figure 4.29b). Devices could then be placed face down against the flat, aligned by the bolt and

bottom edge, and clamped onto the bellows. This provided reliable sixteen channel connections in a rod the size of a standard single electrode holder. The fine hook-up wires were run the length of the 14 cm rod, and soldered to two 1 mm pitch miniature flax flex cables having eight conductors each. This connection at the far end of the rod was epoxied for mechanical stability, leaving the 12 inch long flat flex cables free from the manipulator for connection. The other end of the flat flex cable was then inserted directly into a locking connector on the custom amplifier discussed below.

4.8.3 *Instrumentation – amplifier*

Initial multi-channel experiments were done using A-M Systems Model 1700 four channel extracellular amplifiers. This required soldering a harness of wires connecting the front panel rack mounted inputs to the multielectrode interconnect. This harness was prone to mechanical stress and to large amounts of electrical noise, passing the unamplified neural signals (tens of microvolts) past the front panel of the amplifiers, outside the Faraday cage. Thus, it was decided to build a miniature pre-amplifier specifically for our multielectrodes that would reduce noise and simplify cabling. In addition, having battery power and such small size would mean the amplifier could be used in the field. The specifications for extracellular amplification are simple. An AC coupled voltage amplifier with gain of 1000 and at least 5 kHz bandwidth is adequate.

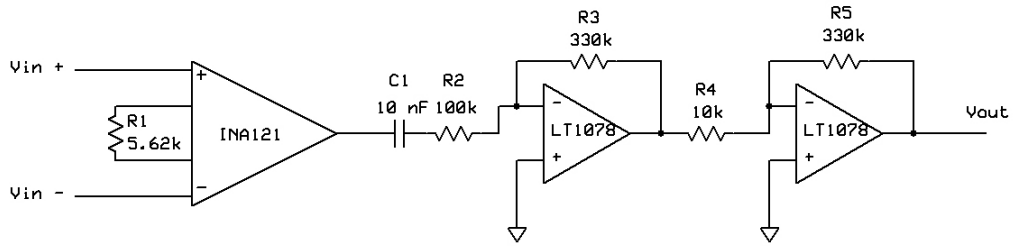

Figure 4.30. Schematic of neural amplifier circuit.
The extracellular amplifier consists of 16 identical channels, each consisting of three stages. The input stage is a Burr-Brown low power precision differential amplifier (INA121). This provides high input impedance, good common mode rejection, and a gain of 10. The second stage is a high pass filter (corner frequency 0.006 Hz) and gain 3.3 amplifier. The final stage utilizes the second half of the LT1078 dual-op amp package to provide another gain of 33.

Dr. Bruce Land provided immense guidance in construction of the amplifier. Each channel consisted of three stages (Figure 4.30). The critical differential input stage was handled with Burr-Brown INA121 low-power FET components. These components have very high input impedance ($5x10^{12}$ ohms || 6 pF), good common mode rejection (112 dB), and draw very little power. This input stage was used to provide a gain of 10x. The output of this was sent through a high pass filter with very low corner frequency (~0.006 Hz) and the first of two halves of an LT1078 op-amp used to provide a gain of 3.3. Finally, the other half of the LT1078 was used to provide a factor 33 gain. This resulted in a total theoretical gain of ~ 1000. The INA121 at a gain of 10 is flat to 1 MHz, and the LT1078s have a gain-bandwidth product of 200kHz. This means the final LT1078 is the bandwidth limiting factor, to about 6 kHz. With signals acquired on the A-M Systems, the low pass filter was usually set to 5 kHz, about the upper limit of useful biological information, so the bandwidth limitation of the custom amplifier in fact provided useful low pass filtering. The completed amplifier channel was measured to have a gain of 1136.

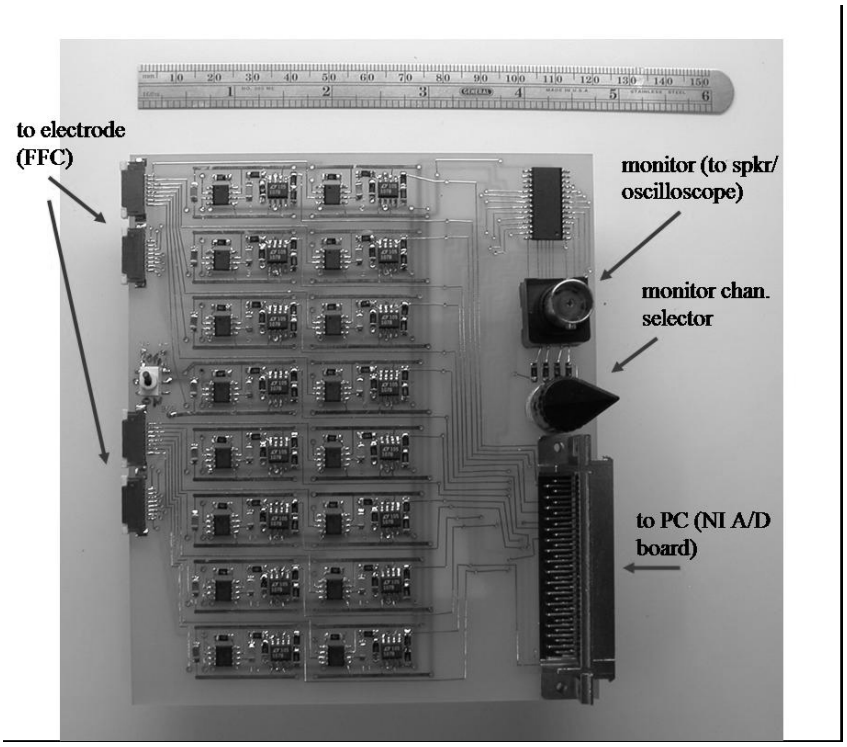

Figure 4.31. Custom surface-mount sixteen channel extracellular amplifer. Amplifier consists of sixteen voltage gain amplifiers, having gain 1000, and a bandwidth of ~5 kHz. Power supply is two 9V batteries (on backside). Input comes from bellows multielectrode in 1 mm pitch micro flat flex cable (left). After amplification, the output is sent both to the analog input channels of a NI 68 pin connector, and a 16:1 multiplexer. The multiplexer address lines are sent to a 16 position selector knob, and the output of the multiplexer is sent to a BNC for observation of the selected channel with audio/oscilloscope.

The multichannel amplifier consisted of sixteen of such channels (Figure 4.31). A printed circuit board (PCB) was designed using free layout software from a commercial prototyping company (ExpressPCB corporation). Surface mount components in the SOIC-8 package were used, in conjunction with SM1206 passive components, enabling the entire sixteen channel interface to occupy a board only 6x4 inches in size. Several additional features were added to the circuit board which simplified the apparatus. Inputs to the amplifier from the multielectrode were surface mount locking connectors, which mate to the flat flex cable from the multielectrode holder. The output of each channel was sent to a 16:1 multiplexer and a connector for

the computer A/D board. The multiplexer is addressed by a 16 position selector knob, such that the knob sends the selected channel output to a BNC for monitoring on a speaker and oscilloscope. This provides a rapid means to observe the activity on each channel. The outputs of each channel are sent to the appropriate pins of a 68 pin connector, to which a 2 meter shielded cable directly connects the amplifier to the computer. This alleviates the need for the signal to pass through a noisy electronics rack, allowing the amplified signal to be fed directly into the computer. It also removes the necessity for a wiring harness, as all 16 channels are carried in the high quality shielded cable. This could be extended to any number of channels, at the limit of the A/D board.

The amplifier was found to have an inputs shorted noise level of 1.6 microvolts. This is in comparison to 25 microvolts for the A-M Systems Model 1700, and 11 microvolts for CMOS circuitry fabricated on-chip in neural electrodes prepared at CNCT [61, 62]. This low noise is achieved by having high quality FET amplifiers in a small footprint amplifier that can be placed inside the electrically shielded Faraday cage, and by powering the devices with 9V batteries, eliminating 60 Hz line noise. The total cost of the amplifier was ~ $300 and it occupies 6x4x1 inches, whereas the A&M Systems amplifiers took up 4 16-inch rack mount spaces, and cost ~ $5000. We note that the custom amplifier does not have individually changeable gains or filter settings.

4.8.4 *Instrumentation – stimulus presentation*

The rudimentary manual puffer stimuli proved adequate for testing of multielectrode operation, but are inadequate more detailed biological investigation. As such, a controlled wind-stimulus generator was necessary. Several such devices have been fabricated by previous investigators using speakers or other drivers, in both free

field and wind-tunnel configurations [56, 66, 147, 161, 162]. In one dimension these wind stimulus generators are relatively simple to fabricate and calibrate. In two dimensions, however, the calibration becomes much more difficult. For our purposes we began with a single 8 inch audio driver, with the option of moving to a two-dimensional setup in a manner similar to Rinberg and Davidowitz [66]. The stimulator consisted of an 8 inch woofer to which was bolted a 15 cm funnel, having an approximately 2.5 cm diameter outlet. This diameter is large enough to ensure even flow over the volume of the cricket cerci. The funnel was sealed to the driver via a Plexiglas™ flange and latex tubing press-fit gasket. The end of the funnel was packed with 2 mm diameter straws to create laminar flow.

The stimulus was calibrated using a solid state microbridge mass airflow meter (Honeywell/Microswitch AWM 2300). The meter was sensitive over ± 1000 sccm, and had a response time of ~ 5 ms, giving a maximum frequency of 200 Hz, which is adequate for cercal stimulation. The maximum forward air velocity was calibrated for a half sinusoid air velocity pulse. Given the diameter of the funnel opening, the stimulator was capable of producing up to 150 cm/s velocities, with logarithmic attenuation down to 0.002 cm/s.

4.8.5 *Simultaneous intracellular / ladder recordings*

The ladder array was tested in a set of experiments in which simultaneous intracellular recordings were made. The ladder array worked as expected in making a more intact preparation feasible (Figure 4.32). The cricket was mounted ventral side up, and a thin strip of cuticle over the nerve cord removed. The ladder could then be slid underneath the nerve cord, and a stable recording achieved. This dissection did not require freeing the entire nerve cord from the abdomen, and the recordings were similar in quality.

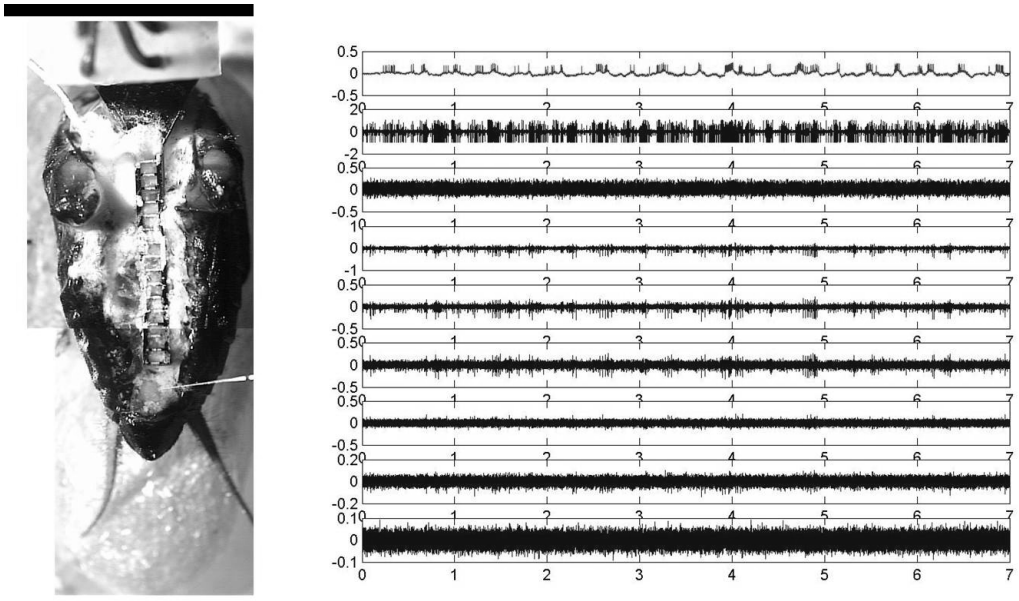

Figure 4.32. Simultaneous intracellular and multielectrode recording
The ladder and intracellular pipette are seen in place on the preparation (left). Recordings from the intracellular pipette (top trace) and first 8 channels of the multielectrode (next 8 traces) are seen at right.

With the preparation in this configuration, the terminal ganglion is also more readily available for interrogation (in a ventral prep, it is on the top surface of the animal, as opposed to at the bottom). As such, the ladder used in this configuration is highly amenable to simultaneous intracellular recording from the terminal ganglion. The nerve cord is in place on the ladder, and the intracellular sharp electrode is penetrating a single cell in the terminal ganglion. The recording shows the intracellular waveform in red, and the first 8 channels of the ladder (moving upward) in blue.

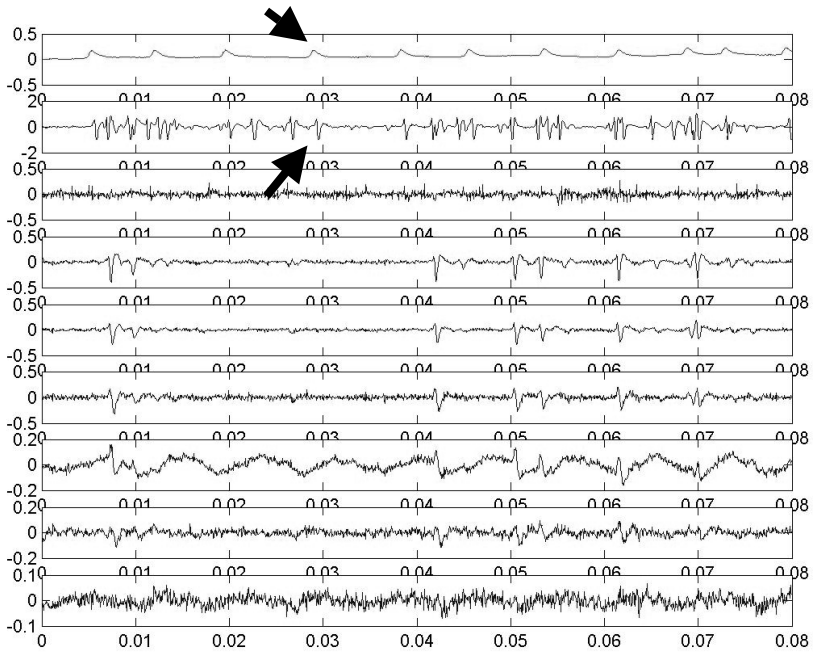

Figure 4.33. Identification of units by simultaneous intracellular
The extracellular waveform of the penetrated unit is identified from coincident spikes (red arrows). This relates extracellular spike template to the intracellularly penetrated unit.

The utility of this dual recording is seen in Figure 4.33. With simultaneous intracellular recordings we have a method to quantitatively identify which neuron is responsible for an extracellular waveform. As can be seen in the time expanded trace in Figure 4.33, the neuron penetrated by the intracellular electrode was not a giant fiber in this case. Spikes from the penetrated cell appeared on the first channel of the ladder, but did not propagate. However, other spikes can be seen propagating to later channels on the ladder. Although this experiment was unsuccessful in that we did not penetrate the correct cell, it can be seen that the extracellular waveform, and hence the measured conduction and amplitude, can be related to an intracellularly penetrated cell. There are local interneurons in the terminal ganglion (ones that do not project down the nerve cord), and it is likely that this was the type of cell that was penetrated

[162]. Recordings from one of these local interneurons have shown it to respond in a phasic manner to wind stimuli, which is what we observed.

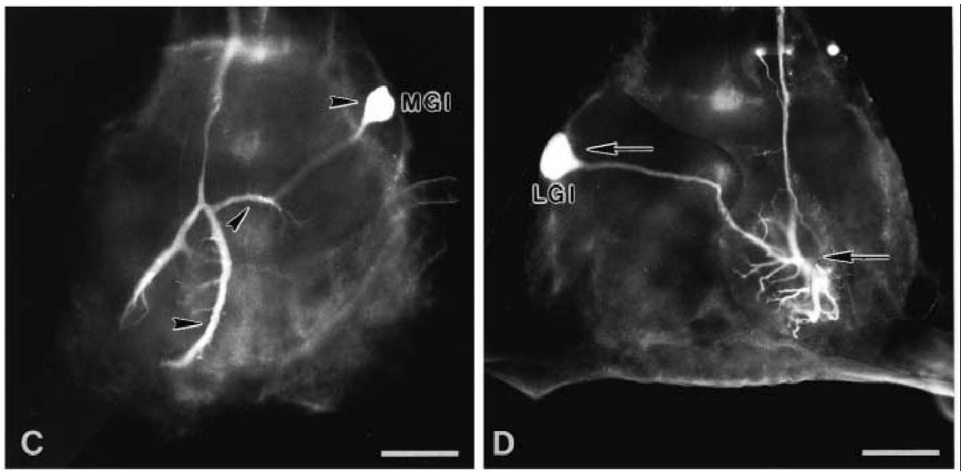

Figure 4.34. Backfill of penetrated unit identifies the neuron
The morphology of the GIs is well documented, and filling of the neuron after recording permits whole mount imaging of the neuron morphology, and thus anatomical identification of the neuron. Image adapted from [163].

Having established which extracellular waveform is produced by the cell, an anatomical identification of the cell can then be carried out using standard backfilling techniques. Figure 4.34 illustrates this process. Upon recording an adequate amount of data for measurement and identification of the largest GIs, and then performing a simultaneous intracellular recording to identify a single neuron, the intracellular neuron is backfilled with a standard dye. Iontophoretic injection over 10 min with 10 nA of Lucifer yellow is adequate. At the end of the experiment the terminal ganglion can be imaged whole mount, and the identity of the cell that was penetrated is revealed.

In this manner, we have a method to measure the extracellular amplitude and conduction velocity of a known neuron. The absolute value of these quantities will vary from specimen to specimen, and may change over tens of minutes in an unstable recording. However, an advantage of invertebrates is that the anatomy is highly

reproducible, meaning that the relative diameters and positions of the axons of the giant fibers within the nerve cord is highly conserved across specimens. This means that although the measured amplitude and conduction velocity of a given GI will vary from preparation to preparation, its position within the hiercharchy of all the GIs should remain fixed. We now how a tool to test how well this holds up. If it turns out that the hierarchy of amplitudes and conduction velocities is enough information to deduce neuron identity, then recordings with the ladder alone can be used, provided a large enough N value to be assured of cell identity.

4.9 Devices for recording across or around the nerve bundle

Using simultaneous intracellular recordings to identify neurons is quantitative; however it requires a large number of preliminary experiments to show that the hierarchy of conduction velocities is an accurate predictor of neuron identity. Getting this large number of data points can be difficult, as obtaining several intracellular recordings from each neuron is a difficult task. In addition, it can misidentify neurons with similar conduction velocities. Our histological results suggest that some neurons have axons with area similar to within 0.3%. The biological variation in conduction velocity is about 1%, thus the neurons would not be separable using conduction velocity measurement alone.

A better approach is to modify our electrode geometry such that we can deduce axon position within the nerve cord directly from the multielectrode recordings. The morphology seen in Figure 4.10 is highly reproduced from animal to animal, and thus a cuff type electrode with several recording sites spaced around the circumference could deduce, by the relative magnitude of the signal at each position, the identity of the axon. In addition, having a “more orthogonal” distribution of spikes across recording sites will greatly aid in resolving overlaps.

4.9.1 *Hook electrode design*

Several cuff electrode designs exist in the literature, and have been used successfully to record and stimulate nerve bundles [15, 16, 164-166]. Most of these, however, focus on recording from large (1mm) diameter nerves in mammals. These are usually visual sciatic nerves or peripheral motor nerve bundles. In order to investigate more directly sensory neural computation in a smaller system, we would like to customize our cuff for small invertebrate nerves.

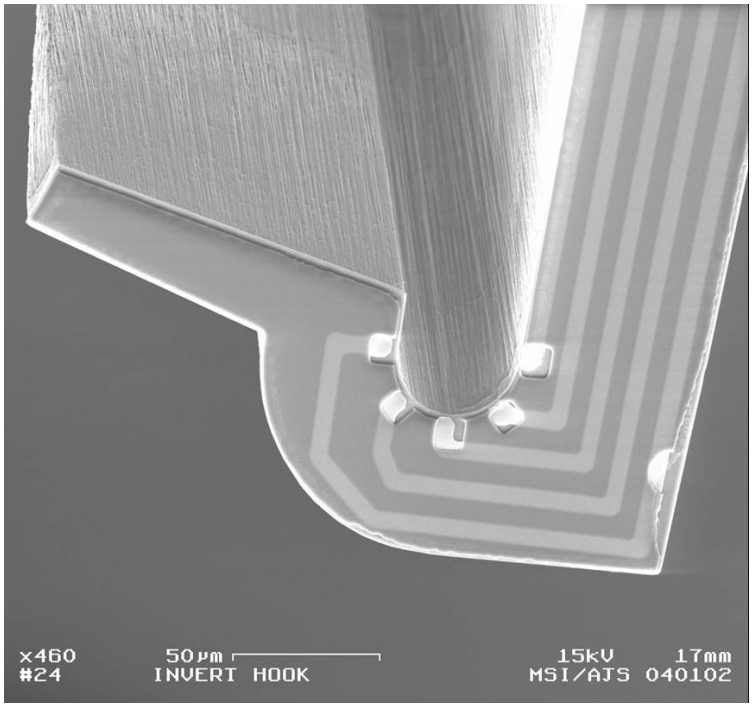

Figure 4.35. A five channel hook electrode for recording around a nerve bundle The circumferentially spaced recording sites are designed to have potential varying with axon position in the bundle

The first cuff developed utilized the existing fabrication process and is seen in Figure 4.35. It consists of a 40 micron diameter trough with 5 recording sites spaced around one half of the diameter. It is designed for the auditory nerve of the moth, an even simpler invertebrate model system, which we discuss below. Due to the

constraints of fabrication, it was not possible to put recording sites on the inner surface of the trough. However, because the device was fabricated using the existing process, it was a simple addition to the wafer, and would be a useful way to garner more information from a device similar in size to a standard single wire hook electrode.

4.10 The moth auditory system

As mentioned above, the smaller 40 micron diameter hook multielectrode was designed for use with another, even simpler invertebrate sensory system, the moth auditory nerve. This work was carried out with the additional guidance of Prof. J. Yack. The moth we have chosen, *Drepana arcuata*, is a fascinating specimen in its own right, and previous to this work its hearing had been unstudied. As such, enough data were collected whilst learning the preparation, using standard techniques and with the collaboration of Prof. A Surlykke and I. Hasenfuss, to warrant a manuscript purely concerned with its biology [167]. We present a summary of the biological background and relevant results here. The remainder of the details, concerning the evolution, frequency tuning, sensory physiology, and biomechanics of the ear are discussed in [167].

Neuroethologically the moth auditory system is tremendously inviting, and has fostered a number of ground breaking studies in physiology, sensory acuity, and evolutionary biology [168-173]. The pioneering work of Prof. K. Roeder led the way to insects being seen as exemplar model systems in which to study the neural basis of behavior. The moth ear is primarily used for evasion of bats. Echolocating bats use ultrasound sonar to hone in on and capture nocturnal moths. Moths, in turn, have evolved ultrasound sensitive ears which detect these echolocating chirps [174]. Information from these ears is used to guide evasive behavior, in many cases simply steering away from the source [170]. At higher amplitude levels, however, some

species of moth will actually perform a powered dive. All of the information utilized by the brain when performing these behaviors comes from auditory neurons in each ear, of which there are often as few as four or in many species only two. The system has been an excellent model one due to its simplicity and the ease of relating anatomy and physiology to behavior. However, a long-standing limitation in these studies has been the overlap of spikes recorded with standard single wire electrodes, hence the motivation for our hook multielectrode.

4.10.1 *Drepana arcuata*

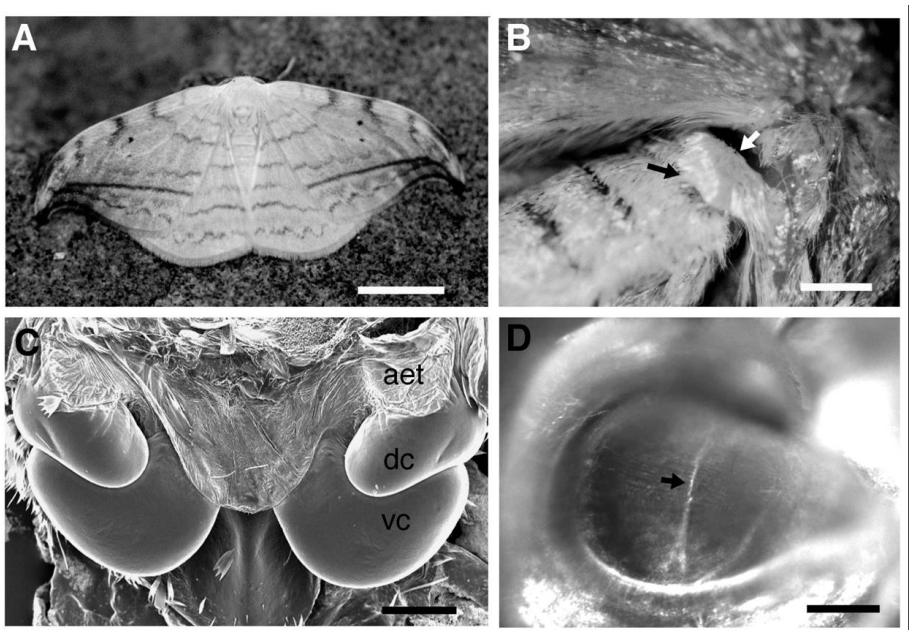

Figure 4.36. Drepanid moth and auditory nerve morphology
The hook-tipped moth (Drepana arcuata) (A), a lateral view of the ear (B), a rostral-cadual view of the air chambers enclosing the tympanal membrane (C), and a sensillum innervating the membrane (D).

The morphology of the moth and ear are shown in Figure 4.36. The tympanal membrane is housed between two chambers (4.36c), a feature unique to this moth. One of four scolopidia (structures in which is the stretch sensitive auditory neurons reside, spanning the membrane and thus transducing acoustic vibration) is seen

indicated by the black arrow in Figure 4.36d. Incident ultrasound causes the membrane to vibrate, which in turn causes the stretch sensitive neurons to depolarize and fire action potentials. Also unique to this moth is that the four sense cells innervate the tympanum at different points (although this cannot be seen in Figure 4.36d, it is illustrated in [167]). In all other moth ears, the sensillum connect to the tympanum at the same point. This could have ramifications for the amplitude sensitivity of the nerve cells, which we discuss below.

Recordings of the activity of the neurons in the auditory nerve using standard single wire electrodes, and in response to ultrasonic pulses, are seen in Figure 4.37. As with other moths, the number of spikes elicited in the first auditory neuron, A1, is proportional to the amplitude of the sound. The second auditory neuron (A2) begins firing at sound levels approximately 20 dB above the threshold of the first. Thus, the two cells work together to span a larger dynamic range in amplitude than either acting alone. This fractionation in amplitude by the auditory neurons is common in other moths, and as such the morphological differences in the ear of Drepana arcuata (two enclosing chambers, and scolopidia innervating the tympanum at different points) make it a very interesting animal. Why does it have these different features if it has "normal" moth hearing? Perhaps having the scolopidia innervate the tympanum at different points is a method of achieving the varied amplitude sensitivity mechanically. Sensillum at the outer edge of the tympanum will be stretched less for a given membrane deflection. A discussion of this possibility and the biomechanics of the tympanum, as well as the other fascinating biological features, are found in [167].

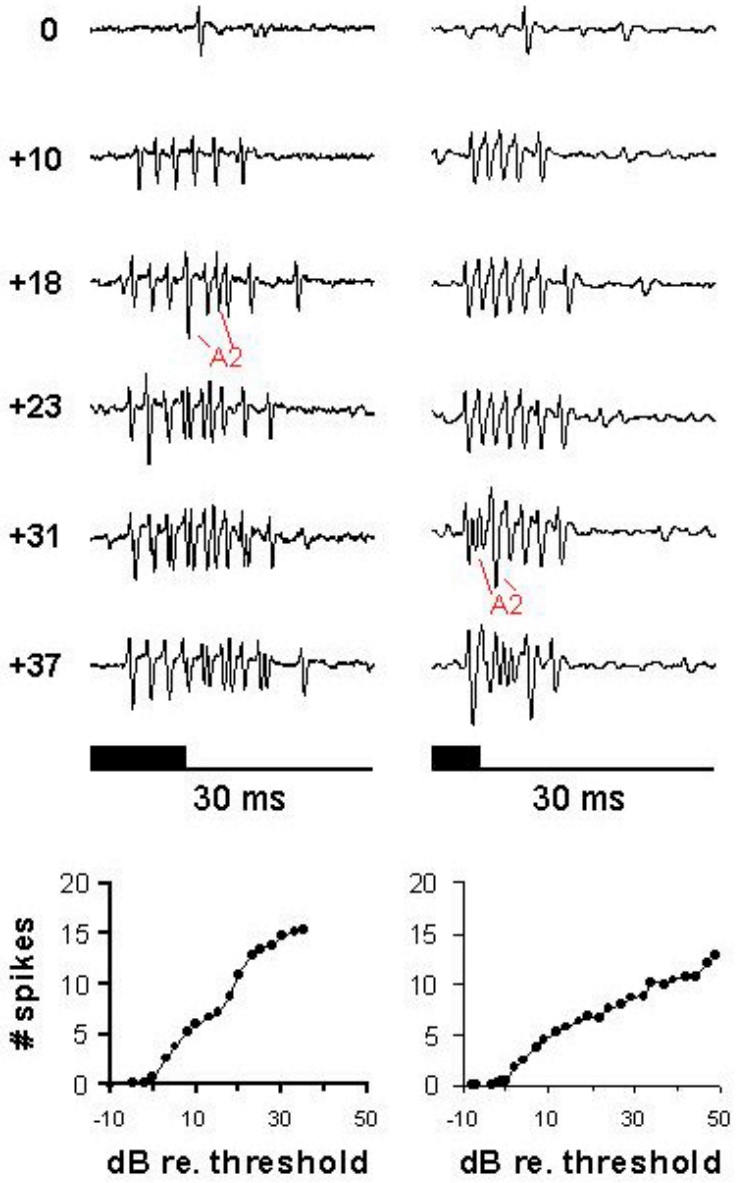

Figure 4.37. Standard recordings from the moth auditory nerve
Recordings with a standard electrode from two specimens. The number of A1 spikes increases linearly with amplitude, suggesting a rate code. The threshold of A2 varied greatly across animals. The problem of spike overlaps is illustrated by traces in which A1 and A2 spikes overlap (+18 dB on left, +31 dB on right).

5 1
4 2
3

4.11 Hook electrode test in the moth

The recordings in Figure 4.37 illustrate the limitation of a single electrode. As the amplitude of stimulus increases, recruiting the A2 cell, the response waveform becomes highly oscillatory, composed of a burst of A1 spikes with A2 spikes superposed at unknown phases. The hook electrode was tested to see if it could provide additional information in sorting this type of activity, using our template matching algorithm. The hook was placed in a prep dissected in an identical manner to that used for single wire recordings. The trough functioned nicely, aligning the nerve across the hook, draped over the edge having the recording sites. The nerve was then lifted until both ends were clearly above the bath, and petroleum jelly applied to the end of the hook, to keep the nerve cord from drying out.

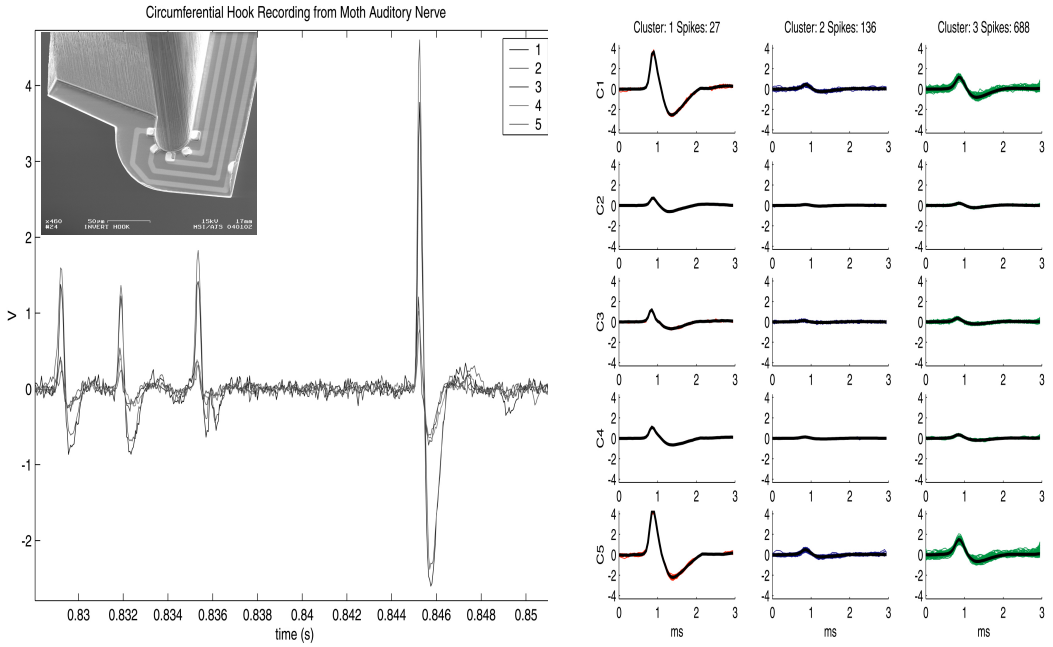

Figure 4.38. Recordings from the moth auditory nerve with the hook multielectrode
The numbering of recording sites and the raw five channel waveforms (channel number indicated by color) are seen at left. Three units were discriminated and their spike templates are seen at right.

A sample of the raw five-channel data is seen in Figure 4.38. We see three spikes from one neuron followed by a single spike from a larger unit. We then used our manual spike clustering algorithm to extract and cluster the spikes. Three very distinct clusters were seen, and the resultant spike templates are shown in Figure 4.38b. The clustering was aided by the appearance of only three units, high signal to noise ratio, and the large differences in spike amplitude. It is generally accepted that the A2 cell is larger in diameter, and has a higher sound amplitude threshold for excitation. Thus, we would expect cluster 1, being the largest spike and having only 27 examples, is most likely the A2 neuron. The spikes in cluster 3 were from a unit that responded to audio stimuli, whereas those in cluster 2 were tonically firing. This implies that this cluster corresponds to spikes from A1, and that cluster 2 is most likely the B cell. We can not be totally confident, however, in the case that this moth has functioning A3 and A4 cells. We could, then, be mistaking them for A1 or A2, although the amplitude threshold for elicitation of the spikes we have recording is a strong indicator that this is not the case.

Unfortunately the spikes from different units are seen to vary across the channels in an identical manner. For example, in Figure 4.38 all three units have the largest waveform on channels one and five.

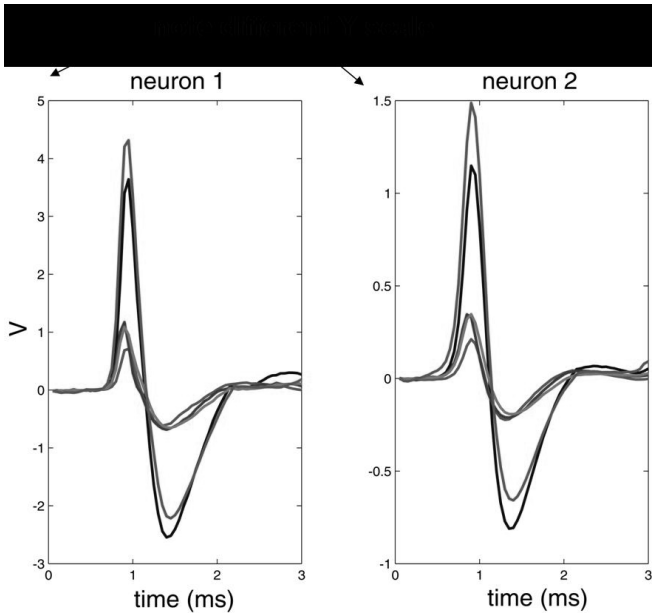

Figure 4.39. Similar spike distributions on the hook multielectrode
Spike templates for units 1 and 3 in Figure 4.29. Note the different y-axis scale. However, the templates from different units have the same distribution in spike shape and amplitude across channels.

In Figure 4.39, we examine more closely the five-channel spike templates for two of the discriminated units. We note immediately that although these spikes came from different axons (judging by the large difference in peak spike amplitude, 5V vs. 1.5V after amplification), their distribution across multitelectrode recording sites is very similar.

Several hypotheses as to the lack of variance in spike templates are worth investigating. The most obvious problem with this device is the lack of recording site-nerve membrane contact. With the recording sites on the side of the trough rather than inside it, we are not in a position that seals the nerve to the recording sites. In addition, we don't have a method to control residual saline. With recording sites some tens of microns apart, separated by a continuous surface, is seems probable that a small amount of saline remains on this surface. This conduction bath will act to short out all five recording sites. The large amplitude seen on channels one and five is equally

troubling because these traces have their conductor running nearest to the edge of the electrode shank, where defects are most likely to occur. This would indicate that the variance in amplitude is due simply to the variation in exposed gold, and not in any physical position of the axon relative to the recording sites.

4.12 Improving the sealing impedance – tweezer electrodes

The above experimentation with the hook electrode made it clear that for additional information to be garnered from laterally spaced recording sites, the precise nature and geometry of the contact between the cord and electrode needs to be monitored and controlled. As mentioned above, the most likely cause of the poorly separated units is inadequate sealing of the recording sites to the external surface of the nerve bundle. After presenting the results of the hook electrode to several investigators, fruitful discussions yielded a new experimental plan. Prof. Robert Olberg and Dr. Tom Adelman were very helpful in their advice. In studying the Dragonfly visual system, these investigators had developed a planar polyimide multielectrode with several rectangular recording sites designed to record across the ventral nerve cord. The crucial factor, however, was that they employed a glass coverslip as an opposing surface, with which they gently pressed the cord onto the multielectrode. This gentle compression serves two purposes: it “squeegees” out the saline on the surface of the device, and it spreads the axons inside the nerve bundle across the recording sites. The electrode recording sites need to “see” the external surface of the nerve bundle, and nothing else. In this configuration, it was reported that very good isolation of axons across several recording sites could be achieved, to the point where simple visual inspection of the multichannel recording showed spikes from one unit distributed across 3 neighboring sites, and another unit might have a spike appearing on 3 separate but neighboring sites (R. Olberg, personal

communication). Getting the correct, highly insulating conditions between the nerve and electrode surface proved difficult. In order to carefully test these conditions, we decided to develop similar “tweezing” multielectrodes, with the goal of controlling and observing the nerve-electrode interface.

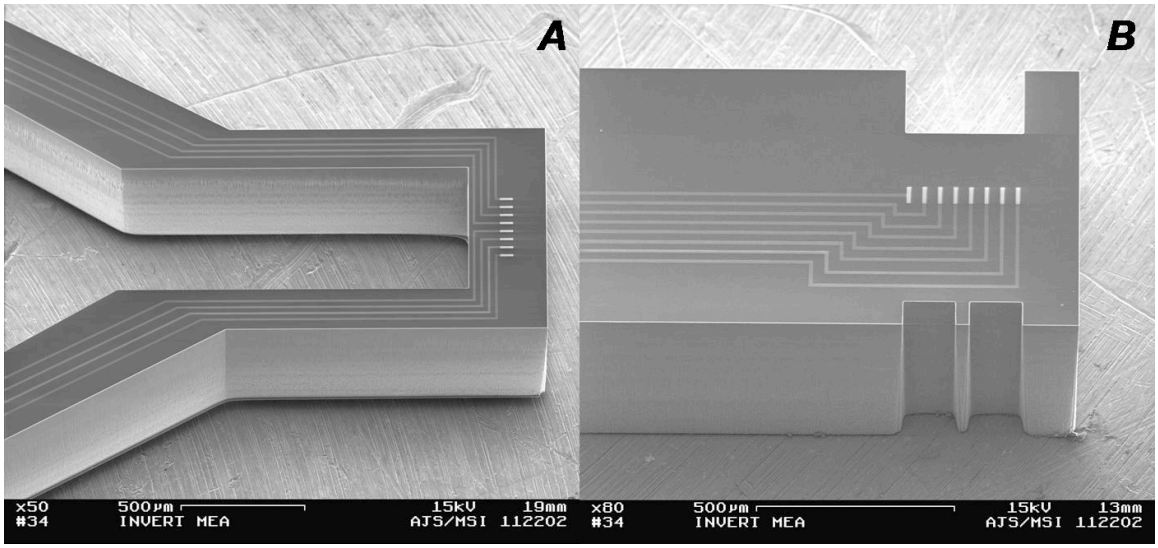

Figure 4.40. SEMs of tweezing electrode designs.
Tweezing electrodes having 8 recording sites spanning 300 microns (each hemi-cord is approximately 150 microns in diameter. The nerve cord runs parallel to the recording sites (left to right in (A), top to bottom in (B). This places four recording sites laterally across each hemi-cord.

The resulting devices are seen in Figure 4.40. Each has eight recording sites, 10 microns wide and 50 microns long, spaced evenly over 300 microns. With each hemi-cord having diameter 140 microns, this will place 4 recording sites across each hemi-cord. Two types of electrode structure having the same pattern of recording sites were fabricated, enabling two different angles of approach to the preparation. The first, seen in Figure 4.40a, is designed such that the nerve cord can be draped over the bridge containing the recording sites, and the manipulator holding the electrode will be parallel to the nerve cord, in the rostral-caudal line of the animal. Specifically, it was to be used by threading the dissected free thoracic ganglion through the opening. In

this manner, the manipulator would be at the rostral end of the prep, leaving the cerci free for stimulation. The second design, shown in Figure 4.40b, is designed to be brought in laterally, at any point along the nerve cord. Notches are etched in the end of the electrode, facilitating alignment of the hemi-cords to the recording sites, holding them in place once the cord is lifted.

Either of these devices can be held in place while gentle compression is applied to the nerve cord. This pressure could be applied by a simple flat surface such as a coverslip. However, it became apparent that with two multielectrodes facing each other and providing the tweezing force, it may be possible to further enhance the multiunit separation. With recording sites on both surfaces that are squeezing the nerve cord, it may be possible to resolve not only lateral position of the axons, but garner some dorso-ventral information as well.

4.12.1 *Interconnect for tweezing electrodes*

The desire to have two multielectrodes with their recording sites face-to-face at separations less than several hundred microns presents challenges for the interconnection scheme. The chief problem lies in interference of the conductor interconnects. Without adding through wafer vias, we have the interconnect pads on opposed surfaces at the base of the electrodes, necessitating some sort of interference design. Such a design is seen in Figure 4.41.

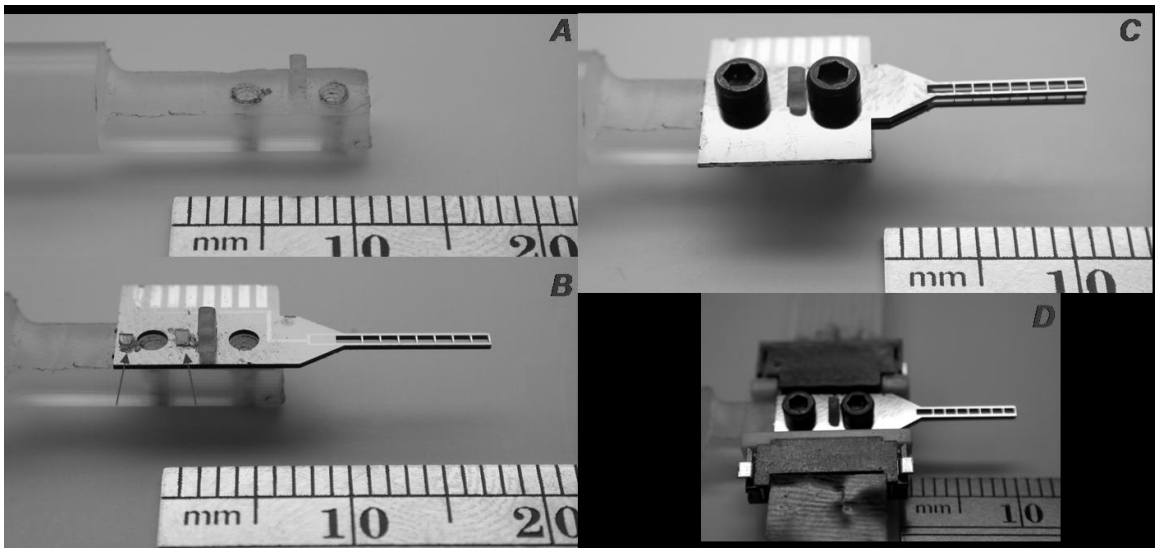

Figure 4.41. Interconnect for tweezer chips
A new flouropolymer holder, with an alignment block and two threaded bolt holes (A). The first chip placed face up on the holder, with spacers on the top surface (cleaved number 1 coverslips of thickness 150 microns) (B). In (C), the second chip has been placed on the holder face down, and the mounting bolts inserted. Note that the chips are identical, and as such the interconnect for the bottom chip comes out toward the top of the figure, and the top chip's interconnect comes out in the opposite direction, to the bottom of the figure. The completed two chips in place with the flat flex cable (FFC) connectors attached to the devices are seen in (D).

The commercially available flat flex cable (FFC) connectors used as input connectors on the amplifier were found to accept 350 micron thick wafer chips. The electrodes designed for use as tweezers were patterned with interconnects meeting the specifications of the FFC connectors, and thus could be directly inserted into the connector, making contact on all channels.

The interconnect area of the chip was then made to project from the left edge of the base of the electrode (Figure 4.41b). In this manner, an identical chip placed face down will have it's interconnect protruding from the right side (Figure 4.41c). This enables the two electrodes to be brought completely into contact, and has the additional advantage that the same device can be used either for a top or bottom electrode.

The electrodes have two bolt holes and a rectangular through-hole. Again, a fluoropolymer rod was machined into a holder. The first electrode is threaded over an alignment block machined into the holder, mating to the rectangular hole in the electrode (Figure 4.41b). The edges of the block provide rough alignment. Pieces of flat spacer material are then mounted on the bottom electrode. In this case, cleaved pieces of #1 coverslip (thickness ~150 microns) were used. The second electrode is then threaded face down on the alignment block, and the two bolts are screwed into aligned holes threaded in the holder.

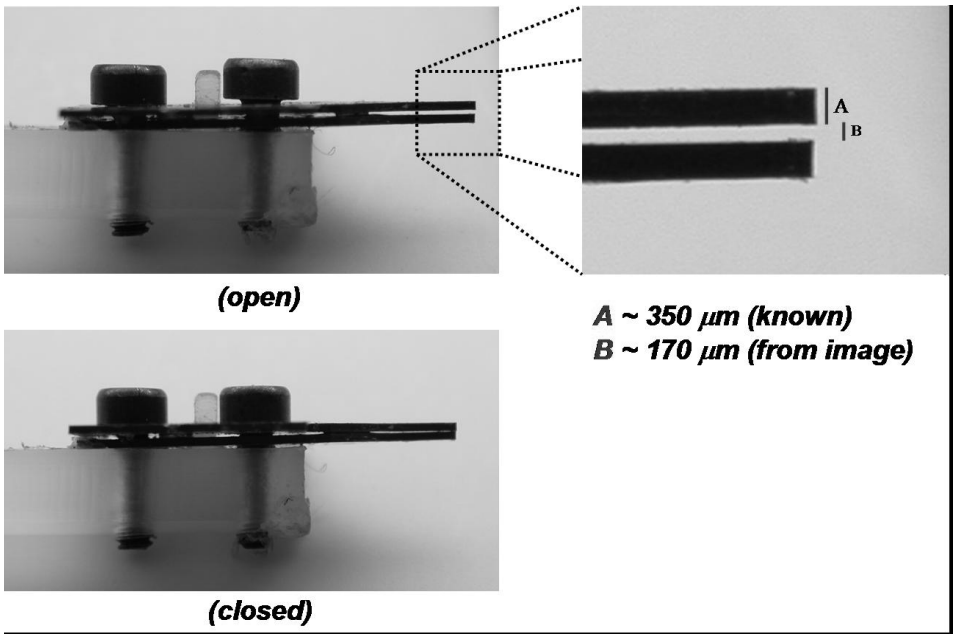

Figure 4.42. Tweezer separation and clamping
Tweezer separation is imaged in the open state (A). Higher magnification view shows the separation approximately 170 microns, as measured by calibrating the image to the known thickness of the wafer. In (C) we see the tweezers fully clamped together by screwing of the right bolt.

Measurement of the separation and clamping ability of the tweezers is shown in Figure 4.42. The rear bolt has been tightened until the electrodes are clamped on the spacer. At this point, the tweezers are separated by a distance roughly equal to the thickness of the spacer. This was measured optically using a light microscope and the

known thickness of the wafer (Figure 4.42b). The electrodes are brittle, and crack with large amounts of flexion, but in the above tweezer configuration there is enough play to bring the ends of the tweezer together (Figure 4.42c).

4.12.2 *Recordings with the tweezers*

Testing of the tweezer electrodes in the cricket ventral nerve cord is illustrated in Figures 4.43-4. For the initial recordings, a single hemi-cord was placed over the tweezer, and the other cut to reduce biological noise. The nerve in place on the bottom electrode is illustrated in Figure 4.43, on the perpendicular array. It can be seen to be placed accurately across the first four recording sites of the electrode.

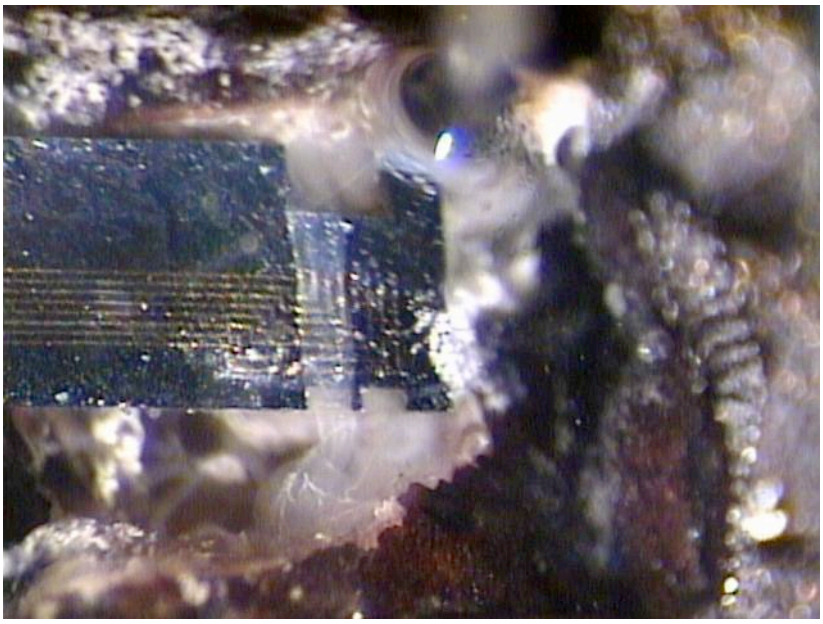

Figure 4.43. The cricket ventral nerve on the bottom tweezer multielectrode
The nerve cord is seen running across the leftmost four recording sites of the multielectrode.

Recordings were made with both tweezers in place, from all 16 recording sites (8 on top, 8 on bottom) versus a silver chloride bath ground placed in the thoracic cavity. A portion of the raw sixteen channel recording is seen in Figure 4.44.

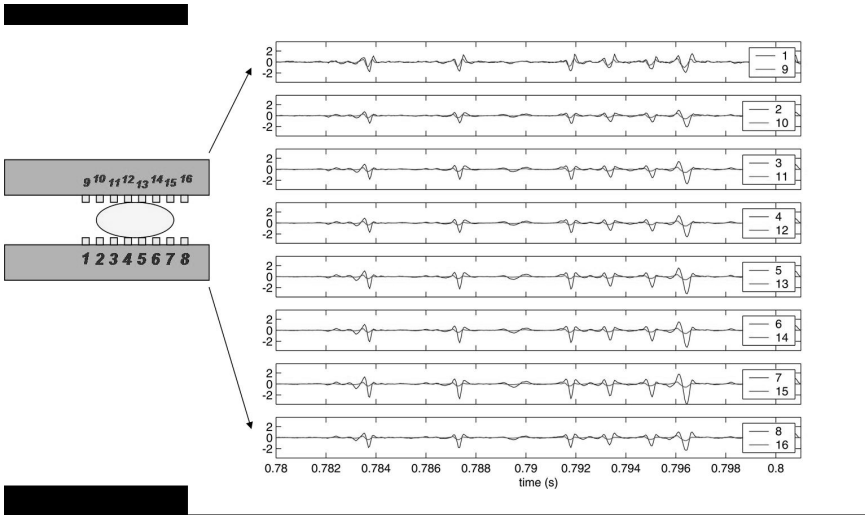

Figure 4.44. Recordings with the tweezers
The configuration is schematically illustrated at left, and 16 channel recordings are shown at right. The lower channels are in red, and upper channels in blue.

As in the case with the hook electrode, we seem to have nearly identical reproduction of every spike on every channel. That is, spikes from different neurons appear with the same distribution of amplitudes across the recording sites. Mild compression was applied with the second bolt, but the recordings did not change significantly. Cluster analysis was carried out and five distinct waveforms were readily discriminated (Figure 4.45).

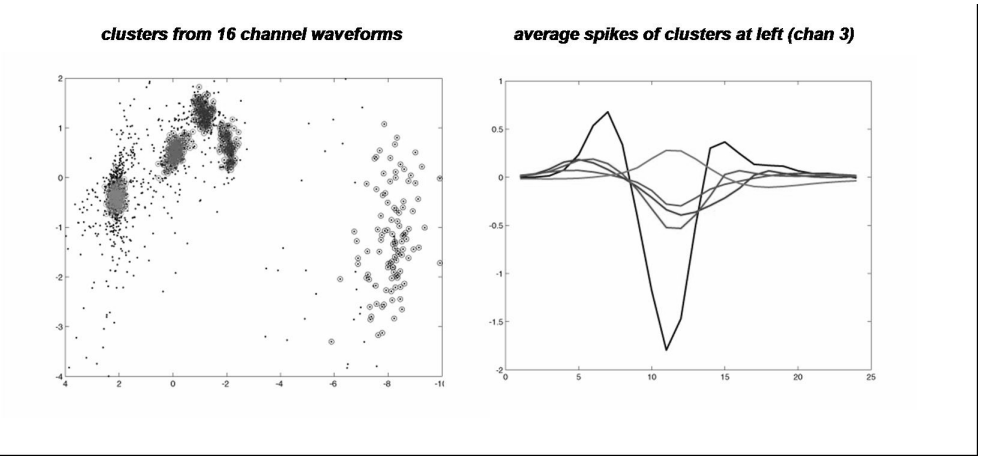

Figure 4.45. Five units discriminated in the tweezer recordings
Clusters are seen at left, and averaging the spikes seen in the clusters produces the templates at right (on a single channel).

Although we did not obtain the clear separation of units across recording sites we were looking for, we carry the analysis further by comparing clusters derived from all channels versus those derived from a single channel. This comparison is shown in Figure 4.46.

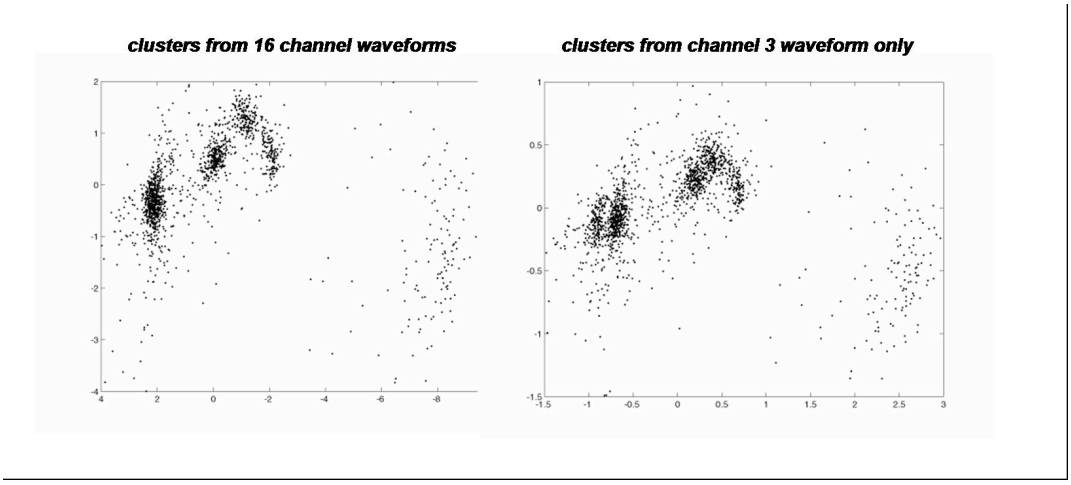

Figure 4.46. Comparison of single versus multi-channel data
Clusters based on single channel (left) and multichannel (right) data. The clusters in the multichannel waveform data are more distinct.

What we find is that the clusters derived from all 16 channels are indeed more clearly separated than those derived from a single channel, although the improvement is not dramatic. It is possible that the improvement in clusters is simply due to recording the same spike on an additional 15 channels, and the resultant averaging away of thermal noise. The fact that the raw traces vary so little with neuron shows that better isolation is possible and necessary.

4.13 Summary of Multielectrodes for Multiunit Recording In Vivo

We have developed a process for microfabricating extracellular multielectrodes that are capable of resolving the activity of multiple neurons *in vivo*. Additional technologies were developed to interface with the devices, amplify the

multichannel signal, and analyze the resultant data. We have shown that devices which sample the conduction of spikes along a nerve bundle can be used to accurately resolve the firing times of 8 neurons when firing at low rates, and 4 neurons in situations with a high level of spike superposition. These devices have the advantage that a single monolithic device, placed onto the nerve cord, can give recordings suitable for multiunit isolation, without the need for multiple electrodes independently placed using several manipulators. The miniature multielectrode, signal acquisition and interconnection scheme we have developed make possible multielectrode recording in the field, something that could not be done with conventional electrodes and "off the shelf" data acquisition hardware.

The algorithm we have used to extract firing times from our data is linear, and very simple. A more sophisticated algorithm such as optimal linear filters or independent component analysis may provide better sorting of the spikes, using the data we have already acquired. However, in personal communications with Prof. Miller, it was found that the optimal linear filtering algorithm is limited by several neurons having similar conduction velocity. Our data confirm this, and show that even with additional longitudinal recording sites (16 vs 8), we are still only able to resolve ~4 neurons accurately during bursts of activity from many of the units.

In order to address this problem, we designed "hook" and "tweezer" multielectrodes for recording around or laterally across a nerve bundle. A 5 channel "hook" multielectrode and 8 channel "tweezer" electrodes were fabricated, in the hopes of achieving a more orthogonal distribution of spikes from different neurons across electrode recording sites. The hook electrode, having recording sites spaced around one-half of a 40 micron diameter auditory nerve, was found to produce nearly identical distributions of spike across the recording sites. This meant that the extra

recording sites were not providing additional information useful for deconvolving multiunit activity or identifying axons. The problem is thought to lie in isolating neighboring recording sites. Any layer of saline present on the surface of the device will act to "shunt" these recording sites, resulting in identical traces.

The "tweezer" devices were fabricated to investigate the possibility of isolating recording sites via mild squeezing of the nerve cord. A novel interconnect allowing two multielectrodes to be placed face-to-face and used to tweeze the nerve cord was fabricated and successfully tested. The data recorded with the tweezers, unfortunately, was similar to that of the hook. Spikes from different neurons had similar distributions across the tweezer recording sites. However, spike sorting carried out on the full multichannel data was cleaner than that done using a single channel, so some amount of additional information was obtained. It would not, however, be enough to resolve more than 4 units in all possible combinations of firing times.

The tweezer devices establish that simple mechanical squeezing of the nerve cord is not enough to provide adequate isolation of closely spaced recording sites. The surface chemistry at the nerve bundle-electrode interface needs to be controlled. Several options are available for controlling this chemistry. Clearly, the way to proceed is to replace the saline at the recording site area with less conducting media that keeps the nerve bundle healthy. An old trick used by neurobiologists is to replace the media with glucose, or other sugars. This may work well for our preparation. In addition, some investigators have reported success using medical supplies such as EEG paste or surgical gels (R. Olberg, personal communication). These investigators report that although the results were difficult to reproduce, in some cases application of these media produced signals that attenuated rapidly between nerve bundle and multielectrode, yielding better axon isolation.

CHAPTER 5: CONCLUSIONS AND FUTURE DIRECTIONS

In this work we have microfabricated devices that attempt to address three long-standing problems in neuroscience. In the area of neuroprosthetics, we have microfabricated model prostheses with controlled geometry in order to understand how the brain's immune response is affected by device size. We used these devices to identify some of the cell types and possible signaling pathways involved in the immune response. Full understanding and control of the response will likely require active manipulation of the biochemical environment surrounding the prosthetic, and to this end we added fluidic channels to our neuroprosthetics. Several useful calculations of the flow properties for devices with different outlet geometry were carried out. These developments are necessary if neuroprosthetic devices are to have a strong, reliable connection to neural tissue, which will take their ability to relieve the symptoms of neurological disorders in human patients to new heights.

The second area of study was in patterned neural cell culture. We microfabricated extracellular multielectrodes on glass wafers, placed aligned guidance proteins on the surface, and observed the activity of patterned reconstructed networks of hippocampal neurons. This approach has two advantages over standard methods. The cultured cells are patterned, and as such the network can be designed with simpler structure and synaptic connectivity than random cultures. In addition, having extracellular electrodes built into the substrate allows for long-term, noninvasive observation of network activity. The major limitation is the lack of ability to record the intracellular potential. If we can use devices such as these to understand how small networks of neurons interact in biochemically controlled environments, we can deduce from the ground up how more complicated neural networks develop, and process information.

Finally, we extended our extracellular electrode array process to work with silicon substrates that could be selectively etched away to produce devices suitable for *in vivo* work. We produced a sixteen channel linear device that measures the conduction of action potentials, and was capable of resolving the activity of 4 or 8 of the giant fibers in the ventral nerve cord of the cricket. We modified this device such that it would be usable in more intact preparations, and in conjunction with intracellular recording, in order to quantify the accuracy of neuron identification from extracellular records. The inability of the device to resolve all 8 units in arbitrary activity patterns led us to the development of devices which record circumferentially around or laterally across the nerve cord. Although these devices showed promise by "sharpening" the data during spike clustering, they did not produce a more orthogonal distribution of multichannel spike waveforms, and thus did not aid in the resolution of spike overlaps, the major obstruction to multiunit recording [125]. It is likely that the problem resides in the surface chemistry at the interface of the nerve bundle and electrode surface, and improved sealing of the bundle to the surface would greatly improve the recordings. Although our devices did not solve the multiunit recording problem, they represent a significant advance. Currently, investigators often only use clean spikes from a single neuron, recorded with single electrodes, in their analyses. Our understanding of how neurons perform such fabulous ensemble computation can not be advanced until we can record their simultaneous activity, and our experiments show that a single microfabricated device can provide enough information to resolve the activity of 4 neurons, inclusive of simultaneous activity. We now have the technology with which we can test exciting theories of ensemble neural coding.

5.1 Microfabricated Neuroprosthetics

If neuroprostheses are to realize their great potential to add to our fundamental knowledge of the nervous system and to restore functions lost due to trauma or disease in humans, it is critical that devices and procedures be developed to minimize or eliminate the formation of the encapsulating sheath. One approach to this problem is to minimize the tissue damage on insertion by making the prosthesis extremely small with smooth surfaces and rounded corners as previously suggested. This approach assumes that the less damage done during insertion the better, and that a smaller cross-section device will cause less initial damage. Data presented here describe early (1 week or less) and prolonged (2 weeks or longer) responses to devices with different sizes, surface characteristics, and insertion methods [42, 91]. We microfabricated devices of varied geometry and surface roughness as well as obtaining devices from the Center for Neural Communication (University of Michigan). We found that the smallest devices damaged less tissue, left a smaller hole when removed from the tissue, and initially produced a smaller volume of reactive tissue than larger devices. The prolonged response of the brain to devices of all sizes was the same, however, resulting in a compact cellular sheath containing astrocytes and microglia [43].

Data presented here continue to support our hypothesis that reactive responses observed after device insertion are of two types – an early reactive response observed immediately after device insertion and a prolonged reactive response that develops with time [91]. The early reactive response may be initiated by the insertion process itself and the resultant damage to brain vasculature and other cells. Since the volume of tissue participating in this response can be related to the cross-sectional area of device shafts, vascular damage and infiltration of cells from the periphery may be important in the development of this process. Initial stages of this response observed

within the first several days after insertion include loss of typical GFAP distribution indicating that significant cellular rearrangement may be occurring. This period is followed by an increase in expression of proteins indicative of reactive astrocytes and microglia, and the concentration of these cells near the insertion site. The prolonged reactive response may occur independently of the early reactive response since the characteristic distribution of cells around the insertion sites is independent of the magnitude of the early response. The hallmark of this response is the formation of a compact sheath around the devices such that all tissue, except that in the immediate vicinity of the sheath, appears similar to that observed in control brain regions.

This project has continued with the work of Scott Retterer [95]. The channel fabrication process has been updated to a more sophisticated oxide sacrificial layer technique, but still uses the DRIE to produce the bulk probe structure, with similar dimensions.

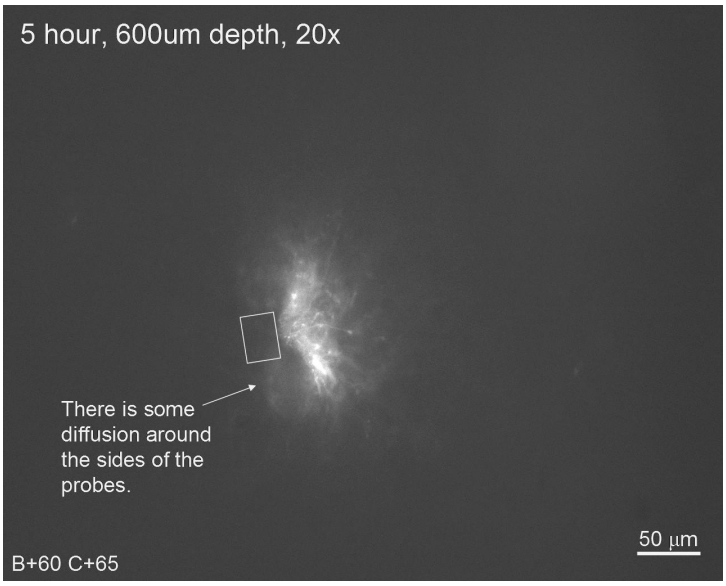

Figure 5.1 Release of transferrin into rat cortex from microfluidic probe
The yellow rectangle indicates the position of the probe. The white fluorescent signal is transferrin that has been taken up by neighboring neurons.

These new probes have now been successfully used to deliver drugs to the rat cortex. The large active molecule Transferrin, labeled with Texas red, was found to diffuse at least 40 microns, and up to 200 microns from the probe site. The drug was taken up by nearby neurons, as can be seen by the spindly shape of the fluorescent image in Figure 5.1. These drugs are delivered directly to the neural tissue, and as such were not screened by the blood brain barrier. This may have profound affects on the ability to reduce scarring and improve the device/brain interface.

5.2 Substrate multielectrodes and *in vitro* cell culture

Designed neuron networks can be constructed using chemical patterning techniques, allowing researchers to investigate the computational capabilities of networks with different architectures. Electrical activity needs to be monitored not only at multiple cells within a cell network, but at multiple locations along single cells, and for long time periods. Single cell, multi-site studies with conventional micropipette patch electrodes have provided considerable information on electrical phenomena in neurons. However, larger numbers of cells and sites need to be monitored simultaneously, and MEAs are useful for characterizing electrical activity [175-177]. Small groups of neurons are also of interest to investigators studying neuronal ensembles [158], and microelectrode arrays have proven useful in this effort [61]. Combining these electrophysiology techniques with advances in molecular cell biology should help to resolve the connection between protein expression, cell network architecture, and computation. The designed cell networks studied in this report raise several issues with regard to cell network construction and computational capabilities. For instance, only some cell networks produced spike trains with regular amplitude attenuation. This may be explained by peculiarities in the cell network: less dendritic currents coupled to the microelectrode, the presence of an axon(s), or

unknown factors affecting the distribution of ion channels within the cells. The spatial averaging inherent in extracellular recordings is useful for monitoring collective responses of multiple cell compartments, but makes resolving responses of individual compartments extremely difficult if not impossible. Reduction of microelectrode size and advances in control of cell growth and electrode coupling may be required to facilitate controlled multi-site recordings from single cells.

Investigators have found extracellular potentials that resemble the first, second, and third derivatives of the intracellular potential [131, 132]. The shapes of extracellular waveforms will vary due to differences in cell-electrode coupling and intrinsic parameters of the active membrane. The insulating, filtering, and other effects of neighboring cells and processes are difficult to estimate, and may have a significant effect on detected potentials. Many factors are thus required to find an adequate explanation for multi-electrode extracellular waveforms. These difficulties led us to our modeling studies [3], which have provided explanations for certain characteristics found in our experiments such as activity-dependent attenuation in spike amplitude.

Chemical patterning techniques can produce organized cell networks, providing limited control of local cell density and increasing the yield of active microelectrodes in MEAs. Bursts of coincident multi-unit activity, which are common in densely-plated conventional cultures and difficult to deconvolve, are typically not present depending on the dimensions of the chemical cues located on the substrate. By directly coupling single cell bodies, axons, and dendrites to extracellular microelectrodes, designed cell networks will help to develop a more quantitative understanding of extracellular recordings and signal propagation throughout the cell. This in turn will provide information about the long-term development of neuronal cell networks and the role of cell morphology in function and computation. High

resolution imaging and targeted multi-stain immunocytochemistry [178] may help to resolve biochemical issues, and allow for the determination of single unit polarity and intra/inter-cellular signal propagation within constructed cell networks.

5.3 Multielectrodes for multiunit recording *in vivo*

We hope that this technology will finally make possible the study of ensemble neural activity. The problem of multiunit recording must be resolved for our understanding of neurobiology to move to more complicated, integrating areas of the nervous system. We have shown that sampling the conduction of spikes using our novel microfabricated devices can solve this problem to some degree. These devices have a success rate that depends heavily on the patterns of activity present in the neural ensemble. Although ultimately one would like to develop a device and algorithm that can resolve arbitrary patterns of activity across all neurons, this may be unnecessary. At this point we should take a step back and consider what patterns of activity are biologically relevant. The awake, behaving cricket being approached by a swooping wasp may only need one spike from three neurons at precise intervals to complete an entire evasive maneuver, which our device, were it usable in an intact preparation, would be adequate to resolve.

For this reason the technologies we have developed are made even more critical. Garnering information from a nerve cord at a single point with circumferential or lateral recording sites will enable the experimenter to “patch in” to activity in the nerve cord in a more intact specimen. The apparatus as we have it now is capable of multielectrode recording in the field. This is made possible by the miniaturized, battery powered amplifier. The apparatus consists of the multielectrode, amplifier, portable data acquisition hardware and a laptop computer. The fact that the multielectrode can be put in place and multiunit data obtained without the need for

several manipulators makes field multiunit recording possible. In future work we hope to use this novel field recording apparatus to observe multiunit activity in the natural environment, and hence understand what the biologically relevant patterns of activity are. This is a very exciting prospect.

Of equal importance to the design of the microfabricated device are the interconnection scheme, packaging, and performance of the signal acquisition electronics. The development of reliable, quick, miniature interconnects between the device and external systems is crucial. This is especially true of systems that include both electronics and microfluidic channels, where both electrical and fluidic coupling must be achieved simultaneously. This area will see rapid development as lab-on-a-chip devices become prevalent. With the continued miniaturization of component electronics, the signal acquisition hardware immediately behind (if not on-chip) the multielectrode will continue to shrink in size will increasing dramatically in processing power. One important advance will be the move to spike sorting in hardware. Devices such as the field programmable gate array (FPGA) will make it possible to implement spike sorting algorithms at very high speeds in hardware. This preprocessing of the raw recordings will free up large amounts of bandwidth in the signal transmitted to data acquisition systems, enabling more neurons to be monitored. The reduced bandwidth required to transmit preprocessed data will make practical multiunit recordings using telemetry, where multiple neurons in a freely behaving animal can be observed. If the raw data can be processed by electronics on the implanted device, then we may overcome the bandwidth limitations of radio transmission.

While the conduction sampling device (ladder) can be used in a reduced preparation in the field, the next great advance will be made when multiple units can

be resolved with a device that attaches to the nerve cord at a single point. This enables the experimenter to remove a very small patch of cuticle and insert the device, leaving the animal largely intact. If this patch of cuticle can be reliably resealed, it will be possible for the animal to freely behave, either tethered or with telemetry. Multiunit recordings from an awake, behaving animal in its natural environment promise to unlock many of the secrets of neural computation. Our goal with the hook and tweezer devices was to establish useful device geometries for multiunit recording at a single point, and the results of our experiments show that to resolve multiple units, a method of insulating the closely spaced recording sites must be developed. The most likely method of achieving this insulation will be in applying a chemical treatment of media substitution. Finding media that keeps the nerve bundle healthy whilst insulating the recording sites from each other and the surrounding bath is the critical problem. The likely candidates are EEG pastes and surgical gels, glycerine, or even sugar solutions.

In the next few sections, we discuss several important aspects of the multiunit recording project.

5.3.1 *Neuron identification*

Other techniques may be brought to bear in order to identify neurons *in situ*. One such method is to use "training session" stimuli. When the stimulus that each neuron prefers is known, they can be used to elicit many spikes from a single unit, and thus identify its extracellular spike shape. In our cricket data, the fact that spikes elicited from some of the units depended strongly on the stimulus direction, despite the relatively crude stimulus, suggests that a "training" session of stimuli, coupled with the accurate measurement of conduction velocity, may be enough to identify units *in situ*. This identification will need to be verified with more simultaneous intracellular recordings and backfills, which we can achieve with our ladder devices. If

two or more neurons have virtually identical spike shape and conduction velocity, however, this technique would not separate them, hence the need for circumferential or lateral information.

5.3.2 *Stability*

We have not assessed the limits of stability of these invertebrate preparations. With a perfusion system and petroleum jelly isolation, we would expect the preparation to be stable for a few hours, based on similar experiments [67]. Ease of integration with microfluidic structures is an obvious bonus of microfabricated arrays [62]. In addition to an on-chip, miniaturized perfusion system, microfluidic channels would offer the possibility of localized pharmacological experiments. These could include release of neuromodulators at specific ganglia or at specific points along the nerve cord.

5.3.3 *Other preparations and minimum cord length*

Many other preparations could benefit from these types of multielectrode array. In addition to the abdominal nerve cord in other arthropods, such as the crayfish or lobster, they would be useful in the peripheral nerves of various vertebrates, including fish, frogs and even mammals. In preparations where a shorter length of nerve is available, cuff or tweezer electrode arrays can still provide additional information. Even if the isolation of recording sites in the cuff electrodes proves a problem, the ability to resolve multiple units using conduction sampling will still be possible. As we have found, the separability will depend on the rough magnitude of the conduction velocities of the units, the differences in their conduction velocities, and the available sampling rate of the A/D. In a case where one unit has a conduction velocity of 1 m/s, and the next is three percent slower, 0.97 m/s, there would be a

readily resolvable difference in spike arrival time (100 μs, or one sample at 10 kHz) after approximately 3 mm. While it may not be possible to resolve several units over such short distances, with adequate sampling rate and a modest difference in conduction velocity, the largest two or three units would be separable.

5.3.4 *Nerve Bundle Modeling*

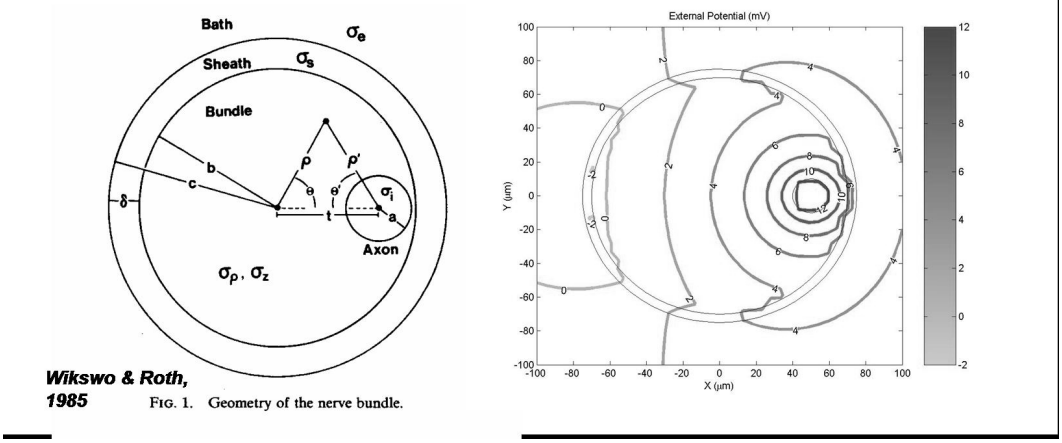

Wikswo & Roth, 1985 FIG. 1. Geometry of the nerve bundle.

Figure 5.2. Analytical model of an axon off-center in a nerve bundle
Wikswo and Roth present the solution for the electric field of a axon eccentrically located inside a nerve bundle.

With devices capable of placing multiple recording sites circumferentially around nerve cords of diameter in the tens of microns range, the role of the nerve sheath needs to be understood. Axon position within the bundle may be entirely masked by the nerve sheath in normal recording configurations. Wikswo and Roth have formulated an analytical model of the electric potential of an axon eccentrically located in a nerve bundle [179]. This model will aid in fabrication of devices and interpretation of recorded potentials. The question of whether usefully differentiated signals can be obtained from circumferential microelectrodes is an open and exciting question.

5.3.5 *Future electrode designs*

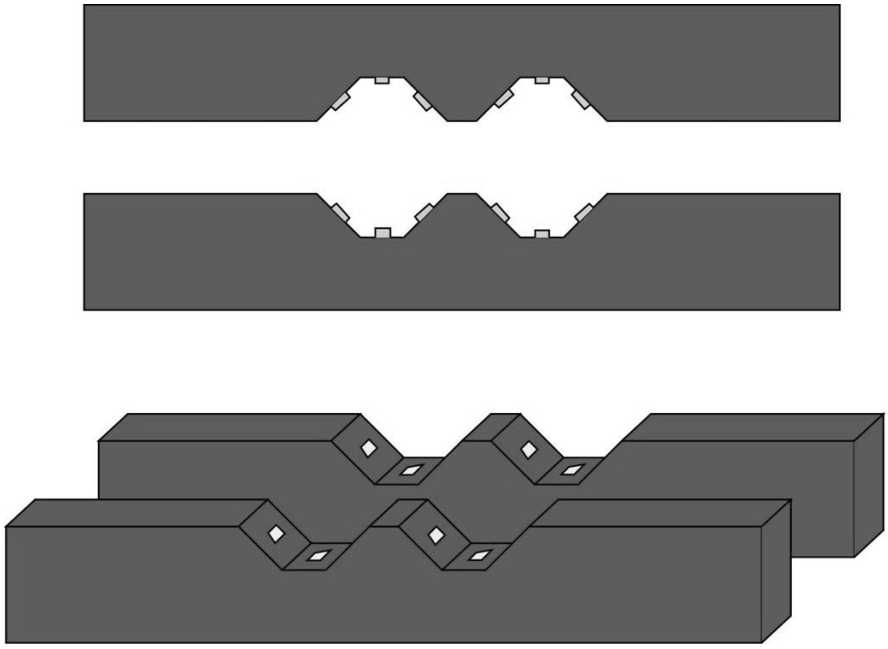

Figure 5.3. Future electrode design
A future electrode structure, designed to solve the sealing impedance problem and garner both conduction velocity and circumferential information from a nerve bundle, is seen above in cross section (A) and schematic (B).

Clearly the optimum electrode design for multiunit resolution, disregarding a need to keep an intact preparation, would combine circumferential and conduction measurements. Such a device is illustrated in Figure 5.3. Similar to the grid array, is has a sequence of recording sites spaced at points along the nerve cord. However, trenches have been etched in each bridge, and recording sites spaced along the sidewalls. These trenches can be added to the current fabrication process using a preliminary KOH etch. Patterning the gold recording sites on the sidewalls and bottom of the trenches presents difficulties, however. We have pursued the initial steps of this fabrication process, and have found that indeed the patterning of resist in the trenches for the gold liftoff step is problematic. Because the trenches are tens of microns deep, the sidewalls and bottom of the trench are not in direct contact with the mask. During

exposure, then, the angled sidewalls and bottom of the trench are exposed to light that is subject to exaggerated diffraction effects from the mask. As a result, the resist pattern on the sidewalls and bottom is poorly defined, often to the point of developing completely away. If it is becomes possible to overcome these problems, however, such a device would provide the optimum amount of information with which to sort spikes. Two such devices, opposing each other, could be clamped onto the nerve to provide both circumferential information and a tight seal.

5.3.6 *Surface modification for better sealing*

Certain chemical modifications to the electrode surface may greatly enhance the separation of units across lateral recording sites. Chemicals such as PEG could be applied before the experiment. These could make the surface hydrophyllic, such that the nerve bundle sheath would adhere to the electrode surface, removing the shunting layer of saline.

5.3.7 *PCA on concatenated waveforms*

We carried out principle components analysis on the entire concatenated waveform, which may be unnecessary. Some subset of spike features may have been adequate. The full waveform of the spike on a single channel could be used, for example, in conjunction with a separate number representing the conduction velocity. However, the concatenation preserves all possible information about conduction velocity and changes in spike waveform, and is readily computable for several thousand spikes on a modern PC.

5.3.8 *Methods for automated clustering*

Several methods exist for automated clustering of data. The simplest methods, such as K-means clustering, simply partition the space among a set of centroids,

iteratively assigning points to each centroid until a set of self consistent (e.g. each point is associated with the nearest centroid) clusters is obtained. This method was tested on our large cricket data set, but the linear boundaries created between centroids often included spikes from a neighboring cluster. The irregular shape and proximity of the clusters created problems for the K-means algorithm.

Recently, more advanced methods have been found to be useful, and would most likely find success with our data set. Superparamagnetic clustering uses calculations from statistical physics to cluster data [180]. Each data point is assigned a spin, and the "temperature" of the resulting system is varied. The expectation values of certain properties of the system indicate when it is in an organized state. At certain temperatures, the interactions of neighboring points within a cluster causes their spins to align, while distinct clusters are not aligned. This algorithm does not suffer from limitations of oddly shaped clusters, and can even deal with ring shaped clusters.

Finally, "agent" based methods may also prove useful in automated clustering. With these methods, multiple "agents" are sent roaming on the data landscape. They interact with data points and with each local neighbors, to determine the number and members of clusters in the data. This method has the advantage that the agents can be run in parallel, and thus it can be computationally efficient, run on a cluster of PCs.

5.3.9 *Moth biological results*

Our anatomical results confirm that drepanid ears are structurally distinct from other insect tympanal ears in having an internal tympanal membrane (i.e. not directly exposed to the animal's exterior) and a chordotonal organ embedded within the tympanal membrane. Further, the drepanid ear is different from all other Lepidoptera ears (with the exception of hedylid butterflies) in having sensory neurons separate from one another, rather than clustered together. In spite of the unique morphology

the overall hearing physiology resembles that of other moths of similar size with respect to frequency range and hearing sensitivity. However, some physiological details are distinct. These include the large variations in response duration and in relative threshold of less sensitive sensory cells, probably reflecting the special morphology.

5.4 Summary

The tools of microfabrication and nanotechnology provide exciting new ways to approach long-standing problems in life science. The functions that can be performed by these devices and the range of new applications for them seem endless. In this work we have tried to use these techniques to take novel approaches to long-standing problems in neurobiology. Where the field of neuroprosthetics is currently hindered by the immune system response, we have shown that microdevices can be developed to understand and control this response, using device geometry and fluid channels for drug delivery. In molecular neurobiology, we developed microfabricated substrates with electrodes and patterned guidance proteins in order to create and monitor networks of real neurons that are small enough to be completely understood, and totally analyzed. Finally, we have developed devices that will enable multineuron recording in living animals. With these devices we can move beyond the function of single neurons, and start asking questions about how groups of neurons are able perform their extraordinarily complex computations in such small volume, with such speed, and with remarkable efficiency.

CHAPTER 6: APPENDIX

6.1 APPENDIX A: Neuroprosthetic study biological methods

6.1.1 *Surgery and device insertion procedure*

The following work was carried out at the Wadsworth Center, Albany, New York. CNF-devices were inserted into the right cerebral cortical hemisphere as previously described (55). Briefly, rats (100-125 g) were anesthetized by intraperitoneal injection of tribromoethanol (targeted dose = 23 mg/100 g body weight) or a mixture of Ketaset and xxx (0.15ml/100g body weight) and mounted in a stereotaxic animal holder. A small midline skin incision was made, the skin pulled aside, and a 2-mm burr hole made in the skull at a point 3 mm lateral and 3 mm distal from Bregma. After piercing the dura, the device was aligned above the hole in the bone and advanced until it just touched the surface of the brain. It was then retracted 1 mm and driven forward 3 mm (2 mm insertion into the brain) at a speed of 2 mm/sec. This resulted in the device shaft being inserted into the cortex while the tab remained above the brain surface. CNCT-devices were inserted manually using fine forceps to grip their tabs. Devices were aligned above the hole in the bone and inserted with a rapid, single motion into the cortex to the depth of the shaft. The tab and hole were covered with a piece of sterile dialysis tubing glued to the skull with Super Glue®. The skin was closed with wound clips and the animals were allowed to recover. All procedures were approved by the Wadsworth Center Institutional Animal Care and Use Committee.

6.1.2 *Preparation of brain tissue*

Animals were prepared for immunohistochemistry and conventional pathology 1 day and 1, 2, 4, 6, or 12 weeks after device insertion. At least two animals were used for each device type at each of the time points studied. The contralateral hemisphere served as a control for each animal. At the scheduled times, animals were anesthetized with tribromoethanol and perfusion fixed with 4% paraformaldehyde in 0.1M phosphate buffer, pH7.4 using methods similar to those previously described (55). Briefly, The skin and skull were removed and the devices were gently withdrawn from the tissue. The brains were then blocked *in situ* and the portion containing the device insertion site and the corresponding contralateral tissue were removed from the cranium. The tissue and devices were post-fixed for 24-48 hrs. The tissue and devices were stored in HEPES-buffered Hanks saline (HBHS) containing sodium azide until further processing. The tissue was sectioned using a vibratome. Coronal tissue slices (100 :m thick) were collected beginning at the brain surface and continuing for 2.5 mm. Tissue slices were stained for GFAP (sections 6 and 16), vimentin (sections 7 and 17), or ED1 (sections 5 and 15) to describe glial morphology and distribution.

For GFAP and vimentin tissue slices were prepared for immunohistochemistry by treatment with 5% sodium borohydride, solubilized with 0.2% Triton X-100 in HBHS, and incubated with 0.1% bovine serum albumin (BSA) in HBHS to block non-specific binding, followed by rabbit anti-cow GFAP antibody (1:100 dilution, Sigma Chemical Co., St. Louis. Missouri, USA) or monoclonal mouse anti-vimentin antibody (1:100 dilution, Sigma Chemical Co.) and rhodamine-labeled anti-rabbit IgG or anti-mouse antibody (1:100 dilution, Sigma Chemical Co.). Samples were mounted in buffered glycerol saturated with n-propylgallate in well slides prepared between two coverslips.

For ED1, tissue slices were treated as described above; however, after the BSA blocking step samples were incubated with 0.3% hydrogen peroxide in HBHS to block endogenous peroxidase. This incubation was followed by monoclonal mouse anti-ED1 antibody (1:50 dilution, Serotec Co., Cedarlane Laboratories, Ltd., Ontario, Canada), HRP-labeled anti-mouse IgG antibody (1:100 dilution, Sigma Chemical Co.) and TSA-tetramethyl rhodamine (NEN Life Sciences, Boston, MA., USA). Samples were mounted as described above.

Devices were stained for GFAP and cell nuclei by treatment with 1% Triton X-100 in HBHS, and incubation with 5% bovine serum albumin (BSA) in HBHS to block non-specific binding, followed by rabbit anti-cow GFAP antibody (1:200 dilution, Sigma Chemical Co.), biotin-conjugated anti-rabbit IgG antibody (BAR, 1:200 dilution, Sigma Chemical Co.), Quantum-Red Streptavidin conjugate (1:20 dilution, Sigma Chemical Co.) and CyQuant™ (1:30000, Molecular Devices, Eugene, Oregon, USA). Samples were mounted in well slides as described above.

Preparation controls were prepared for each immunohistochemical run. These were processed without primary antibodies for all antigens tested. For TSA-amplification, controls were also processed without secondary antibodies but did contain the TSA incubation step. All of these controls were negative for fluorescence. The presented results are representative of 3 or more tissue slices prepared from animals inserted with each type of device.

6.1.3 *Imaging and Image Analysis*

Images of the tissue and of devices labeled for cellular components were collected by confocal laser scanning microscopy using a Bio-Rad MRC600 or a NORAN confocal system mounted on Olympus IX-70 inverted microscopes using 10x (0.40 NA)- and 40x (1.0 NA)- objective lenses. The images were collected as three-

dimensional stacks presented as maximum value projections using BIO-RAD™ , Intervision™ and ANALYZE™ software (47, 48). Images of the devices were also recorded using an ETEC scanning electron microscope in the secondary electron mode after coating the devices with gold in a sputter coater.

6.2 APPENDIX B: Process Notes

Notes on mask making:

Masks need to be rinsed VERY thoroughly if the resist is stripped with 1165. Rinse for a long time with strong DI gun directly hitting mask, slowly move laterally and down. Acetone followed by final IPA may help. 1165 has strong surfactants and takes A LOT of rinsing. Some people use Nanostrip instead—may be better.

Photolith notes:

If you have milky residue after drying wafer, it is probably contamination in DI or developer bucket. Large regions of resist coming up on mask is a resist adhesion problem—common with clear field masks and resist on thick oxide layers (e.g. the first photolith step of this process). YES Oven HMDS vapor primes (30 min) instead of P20 spin on liquid prime can help. One should be able to use Soft Contact mode without trouble with a vapor primed wafer.

Begin with bare silicon 4" wafers. Want thin (<= 350 microns), as wafer thickness determines thickness of electrode shank for the normal process. Single side polished are fine for the normal process (there is an extension to this process that thins the wafers using another deep etch of the backside and another mask). Often thin wafers can only be found double polished, and obviously they work fine for the normal process (but are more expensive). Any orientation is fine, usually <100>, and any doping is fine.

Process steps:

1. Thermal oxidation.

Usually at least 10 wafers per run, using standard MOS clean before oxidation. Wet oxide furnace for 240 minutes at 1100 C. This gives a ~ 1365 nm thick oxide film. Measure/record thickness at several points with interferometer. Worth measuring index of refraction with elipsometer, too.

2. YES oven vapor prime (HMDS – 34 minutes)
3. Spin Shipley 1818 photoresist (on front side)

2000 rpm for 2 seconds, 4000 rpm for 40 seconds, no spin dry, 3 second ramps (gives ~ 2 micron film). Soft bake the wafer on a hot plate at 115 C for 90 seconds.

4. Expose with mask "*Fly 6.0 Gold Mask*".

6 second exposure in either the EV620, Karl Suss MA6, or equivalent contact aligner. Rough alignment of pattern to wafer flat and centering required (bye eye (MA6) or using machine default positions (EV)). You may have problems with resist adhesion (e.g. it comes off wafer and sticks to mask). If this happens, it may be 1165 residue on the mask (if it's a new mask)—clean mask with IPA and nitrogen blow dry. Also works best if the oxide is recently grown.

5. Image reversal (NH3 bake in YES oven—80 mins)
6. Flood exposure (30 seconds in HTG or equivalent)
7. Develop in MF321 for 2.5 min (until visually clear + 30 secs).

Normal develop procedure: place in developer for allotted time, then move to DI water bucket, then remove from DI and hold upright and rinse both sides for 20 secs with DI spray gun, then blow dry until completely dry with nitrogen gun. Same procedure for all development.

8. Descum with 1 min O2 plasma in PT72 (standard O2 plasma recipe)
9. Evaporate Ti and Au

SC4500 evaporator. E-beam evaporation of 10 nm of Ti, followed by thermal evaporation of 250 nm of Au. Load two crucibles of Ti and two boats of Au with three pellets of Au in each (each small pellet gives ~ 100 nm, need 250 nm). Load extra crucible, boat in case there's a problem, you won't need to pump system down again.

E-beam Ti: raise power to 4%, wait 3 min, look at beam and optimize sweep. Raise 1% per minute until evaporating at 2Å/sec. Put down ~ 10 nm (0.1 k Å).

Thermal Au: very sensitive and fast ramping up of power will result in a useless film with huge boulders in it! Au will spit if heated quickly! With 10 V supply, source 2, last run that worked well was: 15% at 1 min, 30 % at 2 min, 41 % at 3 min, then 2 % per minute to 50 %, then 1 % per minute until getting 5Å /sec (this was 53.5% last time). Over time rate may rise to ~ 10Å/sec. Put down 250 nm (2.5 kÅ). Ramp down same way as up.

10. Liftoff of Ti/Au

Place wafers in 1165 for many hours (e.g. over night). Gold should be completely lifted off. Take out of 1165, immediately rinse in IPA (before 1165 dries), and blow dry with nitrogen. Gold pattern should look perfect, and not come off with gentle scratching with tweezers (good adhesion). If after many hours, some areas have not lifted off, place wafers in acetone in the screw top round plastic bucket (just larger than a 4" wafer) in the ultrasonic portable bath in e-beam lithography. Give them 30 min, then remove, quickly rinse with IPA before acetone dries, and then blow dry. Ultrasonic should clear unlifted sections.

11. Descum – 1 min O2 plasma in PT72.

12. Deposit PECVD triple stack or nitride (or other insulating stack):

Triple stack:

PECVD: 200nm oxide, 400 nm nitride, 200 nm oxide.

First use IPE PECVD recipe #1 (oxide). Standard temperature (240C) and 7.4 minutes. Want 200 nm, seem to get it with 7.4 min dep (doesn't agree with rate in book). Full clean (manual plus plasma) then 25 min nitride (recipe #2) dep, run with standard parameters except 240 C instead of 300 C. This lowers film stress. Want 400 nm, hopefully 25 min gets it—but interferometer is not accurate for measuring multi-stacks, so don't know exact thickness. Full clean again, and then final 7.4 min oxide dep (at standard temp: 240C). Want a triple stack of 200 nm oxide, 400 nm nitride, 200 nm oxide.

Old notes for nitride insulation only:

Use IPE PECVD nitride recipe #2 for 60 min, but use temperature 200 C instead of 300 C. This reduces stress of the film (so it adheres to gold better). Measure nitride thickness with the interferometer's Nitride on Au recipe (must recalibrate with a bare gold substrate! Need a gold film wafer around). Usually have ~800 or ~900 nm of nitride.

13. Spin Shipley 1818 photoresist (on front side)

2000 rpm for 2 seconds, 4000 rpm for 40 seconds, no spin dry, 3 second ramps. Soft bake the wafer at 115 C for 90 seconds.

14. Expose with mask "*Fly 6.0 Holes Mask*".

3.2 second exposure in the EV620, Karl Suss MA6, or equivalent contact aligner. *Align* using alignment marks. This alignment needs to be within ~ 1 micron

for small (10 x 10 micron) recording site holes to have roughly the right area of exposed gold.

15. Develop in CD26 for 3 min or until nicely clear as seen in microscope. Check alignment in microscope, save pictures.

16. RIE etch of triple stack/nitride in PT72

Used standard recipe #8. 70% flow of CF4, 30 % RF power. Averages about 77 nm / min for the 200 C nitride. Last run did 12.5 min followed by 2 min for a total of 14.5 min. This was bad! Devices at edge of wafer started to have their gold fade (e.g. the gold was etched by the plasma, and almost gone!). Need to do 1 min runs as you get close to breaking through the nitride, checking remaining thickness with the interferometer, and rotate wafer positions on the platen to average out non-uniformities in etch rate.

17. Strip resist

Either soak in acetone (> 30 min) or put in acetone in ultrasonic bath (> 30 min), then rinse in IPA (before acetone dries to avoid residue), followed by blow dry. Inspect—if there is still scum on wafer, do an O2 plasma descum in Branson or PT72.

18. Spin Shipley 1045 photoresist (on front side)

Thick resist recipe: 400 rpm 5 sec, 800 rpm 5 sec, 1500 rpm 30 sec. 3 second ramps. *Dynamic deposit:* during the first 400 rpm spin, pour 1045 directly out of the bottle onto the center of the wafer, until it spreads ¾ of the way to the edge of the wafer. Stop pouring as it ramps to 800 rpm. *WIPE* the edge of the bottle and top of the bottle lip clean with acetone on a beta wipe after each spin to prevent resist flakes from building up in the bottle lid and screw. Keep bottle clean for future pouring! Soft bake the wafer at 90 C for 4.5 min. Or 1 hour in oven at 90 C. Gently remove from

hotplate, hold in air for a few secondss before placing on cooling block. This helps prevent cracks, which seem to appear more often if you put the wafer directly on cooling block from hot plate. Lots of cracks in thick resist can lead to defects—respin if lots of cracks.

19. Expose with mask "*Fly 6.0 Paddle Mask*".

12 second exposure in the EV620, Karl Suss MA6, or equivalent contact aligner. *Align* using alignment marks. This alignment needs to be within ~ 1 micron for hook electrodes to come out (recording sites are just next to edge of structure).

20. Develop in CD26 for 6 min or until nicely clear as seen in microscope.

21. Check alignment in microscope, save pictures.

22. RIE etch through oxide with CF4 plasma in PT72

Etch through thermal oxide layer using same recipe #8 in PT72. Last time, *50 min* was perfect. After this etch, the trenches should all look like plain grey silicon (if they have any color, e.g. blue or red, there is still some oxide—measure it's thickness in the interferometer and perform another etch until all the trenches on the wafer are clear).

23. Strip resist edge bead.

Don't want wafer to get stuck to clamp in Unaxis with the thick resist, so clean edge bead. Place wafer on spinner, spin at 500 rpm, and place a q-tip with acetone on the edge of the spinning wafer to clean approx 1/8 inch (from outer edge of wafer inward, approx 1/8 inch) of resist off. Once you've defined the 1/8 inch of cleared resist, pick the wafer up by the edge with one hand and use a q-tip in the other hand to clean this 1/8 inch strip (with a repeatedly cleaned acetone soaked q-tip) until the

resist is completely gone in this outermost ring of the wafer. Also clean the outward facing edge of the wafer, and any resist on the backside.

24. Deep etch through wafer in Unaxis 770 or PT770

Use OTRENCH recipe. Supposedly etches at ~ 2 microns / minute. Measure this with the profilometer (P10 or alpha step). Last run (2/28/02) got 307 microns etched after 117 minutes = 2.56 microns/minute. Very fast! On this run 148 minutes total time was perfect for complete etch through the wafer. Before stripping resist, check that the features have cleared nicely all the way to the bottom of the wafer by viewing the wafer in transmission in an optical microscope (the Olympus or the microscope with scale bars in photolith). The dark silicon features should have sharp edges similar to the CAD pattern all the way down. If there are blobs of darkness as you move down in focus then the silicon has not cleared at the bottom of the trench and another 15 or 20 mins of etching is necessary. If the backside oxide film is nicely intact (and it should be) then the He alarm should never sound during the deep etch (on the last run it never sounded). If the He alarm goes off (meaning the membrane broke and He is leaking through the wafer holes) then complete the etch with OTRNOHE recipe. It's the OTRENCH recipe with He cooling turned off. This recipe will burn the resist very quickly, so only etch for the minimum amount of time possible. Anything above 5 min, and it may be difficult to get the resist off. The etch should be done it steps, and cracks seem to appear in the nitride during the deep etch. It would be good to characterize their appearance over time—taking pictures of the devices at specific intervals of deep etching—say every 30 min.

25. Strip resist.

Use any method—O2 plasma in Branson (resist *strip* recipe) for 7 minutes works well, though verification that it does not sputter/scum up the gold would be

good (some users report that Branson scums up samples). Wet stripping with acetone bath/ultrasonic followed by IPA bath/ultrasonic may be used also, but may not work if resist is burnt. Wet cleaning may be only option if O2 plasma is sputtering gold.

26. *Optional* -- RIE etch backside oxide PT72 CF4 plasma

Currently have been simply breaking backside oxide before using devices, but this is sub-optimal. Would be good to flip wafer over and run 50 minute PT72 CF4 plasma etch again to strip the oxide from the backside of the wafer. Another method that works is to place wafer face up in a teflon wafer holder, put it in a plastic bucket, and fill with BOE very carefully until it wets the backside of the wafer only (surface tension will aid in preventing the chemical from covering the front side—but the front can still have the resist mask from the final deep etch, which can be stripped after this wet etch). Once it has etched through the backside oxide (visual inspection should reveal the backside is a flat grey color, with no angular variation), the wafer should be rinsed thouroughly and dried.

BIBLIOGRAPHY

1. Maluf, N., *An introduction to microelectromechanical systems engineering*. Artech House microelectromechanical systems library. 2000, Boston: Artech House. xix, 265.
2. Powers, M.J., et al., *A microfabricated array bioreactor for perfused 3D liver culture.* Biotechnology and bioengineering., 2002. **78(3)**: p. 257-69.
3. James, C.D., et al., *Extracellular Recordings from Constructed Neuronal Networks using Planar Microelectrode Arrays.* IEEE Trans Biomed Eng, 2002 (submitted for publication).
4. Levene, M.J., et al., *Zero-mode waveguides for single-molecule analysis at high concentrations.* Science, 2003. **299**(5607): p. 682-686.
5. Hoch, H.C., L. Jelinski, and H.G. Craighead, *Nanofabrication and biosystems : integrating materials science, engineering, and biology*. 1996, Cambridge ; New York: Cambridge University Press. xviii, 423.
6. Yoo, K., et al., *Fabrication of biomimetic 3-D structured diaphragms.* Sensors and Actuators a-Physical, 2002. **97-8**: p. 448-456.
7. Beer, R.D., R.E. Ritzmann, and T.M. McKenna, *Biological neural networks in invertebrate neuroethology and robotics*. Neural networks, foundations to applications. 1993, Boston: Academic Press. xi, 417.
8. Agnew, W.F., et al., *Histopathologic evaluation of prolonged intracortical electrical stimulation.* Exp Neurol, 1986. **92**(1): p. 162-85.
9. Agnew, W.F., et al., *Electrical stimulation of the brain. IV. Ultrastructural studies.* Surg Neurol, 1975. **4**(5): p. 438-48.

10. Drake, K.L., et al., *Performance of planar multisite microprobes in recording extracellular single-unit intracortical activity.* IEEE Trans Biomed Eng, 1988. **35**(9): p. 719-32.
11. Hambrecht, F.T., *Neural prostheses.* Annual review of biophysics and bioengineering., 1979. **8**.
12. Heetderks, W.J. and F.T. Hambrecht, *Applied Neural Control in the 1990s.* Proceedings of the IEEE, 1988. **76**(9): p. 1115-1121.
13. McCreery, D.B., W.F. Agnew, and L.A. Bullara, *The effects of prolonged intracortical microstimulation on the excitability of pyramidal tract neurons in the cat.* Ann Biomed Eng, 2002. **30**(1): p. 107-19.
14. Bhadra, N. and J.T. Mortimer, *Extraction forces and tissue changes during explant of CWRU-type intramuscular electrodes from rat gastrocnemius.* Ann Biomed Eng, 1997. **25**(6): p. 1017-25.
15. Grill, W.M. and J.T. Mortimer, *Neural and connective tissue response to long-term implantation of multiple contact nerve cuff electrodes.* J Biomed Mater Res, 2000. **50**(2): p. 215-26.
16. Veraart, C., W.M. Grill, and J.T. Mortimer, *Selective control of muscle activation with a multipolar nerve cuff electrode.* IEEE Trans Biomed Eng, 1993. **40**(7): p. 640-53.
17. Grill, W.M. and J.T. Mortimer, *Inversion of the current-distance relationship by transient depolarization.* IEEE Trans Biomed Eng, 1997. **44**(1): p. 1-9.
18. Grill, W.M. and J.T. Mortimer, *Electrical properties of implant encapsulation tissue.* Ann Biomed Eng, 1994. **22**(1): p. 23-33.
19. McCreery, D.B., et al., *A quantitative computer-assisted morphometric analysis of stimulation-induced injury to myelinated fibers in a peripheral nerve.* J Neurosci Methods, 1997. **73**(2): p. 159-68.

20. McCreery, D.B., et al., *A characterization of the effects on neuronal excitability due to prolonged microstimulation with chronically implanted microelectrodes.* IEEE Trans Biomed Eng, 1997. **44**(10): p. 931-9.

21. Tyler, D.J. and D.M. Durand, *A slowly penetrating interfascicular nerve electrode for selective activation of peripheral nerves.* IEEE Trans Rehabil Eng, 1997. **5**(1): p. 51-61.

22. Woodford, B.J., et al., *Histopathologic and physiologic effects of chronic implantation of microelectrodes in sacral spinal cord of the cat.* J Neuropathol Exp Neurol, 1996. **55**(9): p. 982-91.

23. Ceballos-Baumann, A.O., et al., *Thalamic stimulation for essential tremor activates motor and deactivates vestibular cortex.* Neurology., 2001. **56(10)**: p. 1347-54.

24. Pirker, W., et al., *Chronic thalamic stimulation in a patient with spinocerebellar ataxia type 2.* Movement disorders : official journal of the Movement Disorder Society., 2003. **18(2)**: p. 222-5.

25. Alesch, F., et al., *Stimulation of the ventral intermediate thalamic nucleus in tremor dominated Parkinson's disease and essential tremor.* Acta neurochirurgica., 1995. **136(1-2)**.

26. Banwell, J.G., et al., *Management of the neurogenic bowel in patients with spinal cord injury.* The Urologic clinics of North America., 1993. **20(3)**: p. 517-26.

27. Blond, S., J. Siegfried, and C.H.R.U.L.F. Department of Neurosurgery, *Thalamic stimulation for the treatment of tremor and other movement disorders.* Acta neurochirurgica. Supplementum., 1991. **52**.

28. Caparros-Lefebvre, D., et al., *Chronic thalamic stimulation improves tremor and levodopa induced dyskinesias in Parkinson's disease.* Journal of neurology, neurosurgery, and psychiatry., 1993. **56(3)**: p. 268-73.

29. Bell, T.E., K.D. Wise, and D.J. Anderson, *A flexible micromachined electrode array for a cochlear prosthesis.* Sensors and Actuators a-Physical, 1998. **66**(1-3): p. 63-69.

30. Loizou, P.C., *Introduction to cochlear implants.* IEEE engineering in medicine and biology magazine : the quarterly magazine of the Engineering in Medicine & Biology Society., 1999. **18(1)**: p. 32-42.

31. Spelman, F.A., *The past, present, and future of cochlear prostheses.* IEEE engineering in medicine and biology magazine : the quarterly magazine of the Engineering in Medicine & Biology Society., 1999. **18(3)**: p. 27-33.

32. Margalit, E., et al., *Retinal prosthesis for the blind.* Survey of ophthalmology., 2002. **47(4)**: p. 335-56.

33. Chow, A.Y., et al., *Subretinal implantation of semiconductor-based photodiodes: durability of novel implant designs.* Journal of rehabilitation research and development., 2002. **39(3)**: p. 313-21.

34. Rizzo, J.F., 3rd, et al., *Retinal prosthesis: an encouraging first decade with major challenges ahead.* Ophthalmology., 2001. **108(1)**: p. 13-4.

35. Popoviâc, M.B., *Control of neural prostheses for grasping and reaching.* Medical engineering & physics., 2003. **25(1)**: p. 41-50.

36. Litke, A.M., et al., *Large-scale imaging of retinal output activity.* Nuclear Instruments & Methods in Physics Research Section a-Accelerators Spectrometers Detectors and Associated Equipment, 2003. **501**(1): p. 298-307.

37. Kennedy, P.R. and R.A. Bakay, *Restoration of neural output from a paralyzed patient by a direct brain connection.* Neuroreport., 1998. **9(8)**: p. 1707-11.

38. Schmidt, S., et al., *Biocompatibility of silicon-based electrode arrays implanted in feline cortical tissue.* Journal of biomedical materials research., 1993. **27(11)**: p. 1393-9.

39. Rousche, P.J., R.A. Normann, and U.o.U.S.L.C. Department of Bioengineering, *A method for pneumatically inserting an array of penetrating electrodes into cortical tissue.* Annals of biomedical engineering., 1992. **20(4)**.

40. Hoogerwerf, A.C. and K.D. Wise, *A 3-Dimensional Microelectrode Array for Chronic Neural Recording.* Ieee Transactions on Biomedical Engineering, 1994. **41**(12): p. 1136-1146.

41. Edell, D.J., et al., *Factors Influencing the Biocompatibility of Insertable Silicon Microshafts in Cerebral-Cortex.* Ieee Transactions on Biomedical Engineering, 1992. **39**(6): p. 635-643.

42. Turner, J.N., et al., *Cerebral astrocyte response to micromachined silicon implants.* Exp Neurol, 1999. **156**(1): p. 33-49.

43. Szarowski, D.H., et al., *Brain responses to micro-machined silicon devices.* Brain Research, 2003. **983**(1-2): p. 23-35.

44. Chen, J.K., et al., *A multichannel neural probe for selective chemical delivery at the cellular level.* Ieee Transactions on Biomedical Engineering, 1997. **44**(8): p. 760-769.

45. Murvai, J., et al., *Prediction of protein functional domains from sequences using artificial neural networks.* Genome Research, 2001. **11**(8): p. 1410-1417.

46. Kim, G. and A.P. Barros, *Quantitative flood forecasting using multisensor data and neural networks.* Journal of Hydrology, 2001. **246**(1-4): p. 45-62.

47. Shapiro, M., *Plasticity, hippocampal place cells, and cognitive maps.* Archives of Neurology, 2001. **58**(6): p. 874-881.

48. Elliott, C.J.H. and A.J. Susswein, *Comparative neuroethology of feeding control in molluscs.* Journal of Experimental Biology, 2002. **205**(7): p. 877-896.

49. Pfluger, H.J. and R. Menzel, *Neuroethology, its roots and future.* Journal of Comparative Physiology a-Sensory Neural and Behavioral Physiology, 1999. **185**(4): p. 389-392.

50. Heisenberg, M., *Genetic approach to neuroethology.* Bioessays, 1997. **19**(12): p. 1065-1073.

51. Konishi, M., *Neuroethology of Sound Localization in the Owl.* Journal of Comparative Physiology a-Sensory Neural and Behavioral Physiology, 1993. **173**(1): p. 3-7.

52. Hoy, R., T. Nolen, and P. Brodfuehrer, *The Neuroethology of Acoustic Startle and Escape in Flying Insects.* Journal of Experimental Biology, 1989. **146**: p. 287-306.

53. Camhi, J.M., *Invertebrate Neuroethology - Introduction.* Experientia, 1988. **44**(5): p. 361-362.

54. Huber, F., *Invertebrate Neuroethology - Guiding Principles.* Experientia, 1988. **44**(5): p. 428-431.

55. Bacon, J.P. and R.K. Murphey, *Receptive fields of cricket giant interneurones are related to their dendritic structure.* J Physiol, 1984. **352**: p. 601-23.

56. Jacobs, G.A., J.P. Miller, and R.K. Murphey, *Integrative mechanisms controlling directional sensitivity of an identified sensory interneuron.* J Neurosci, 1986. **6**(8): p. 2298-311.

57. Burrows, M., G. Laurent, and A.H.D. Watson, *The Role of Intersegmental Interneurones in the Transfer of Mechanosensory Information between Local Centers in the Locust.* Journal of Physiology-London, 1988. **396**: p. P75-P75.

58. Laurent, G. and M. Burrows, *Intersegmental Interneurons Can Control the Gain of Reflexes in Adjacent Segments of the Locust by Their Action on Nonspiking Local Interneurons.* Journal of Neuroscience, 1989. **9**(9): p. 3030-3039.

59. Laurent, G. and M. Burrows, *Distribution of Intersegmental Inputs to Nonspiking Local Interneurons and Motor Neurons in the Locust.* Journal of Neuroscience, 1989. **9**(9): p. 3019-3029.

60. Jin, W., R.J. Zhang, and J. Wu, *Voltage-sensitive dye imaging of population neuronal activity in cortical tissue.* J Neurosci Methods, 2002. **115**(1): p. 13-27.

61. Bai, Q. and K.D. Wise, *Single-unit neural recording with active microelectrode arrays.* IEEE Trans Biomed Eng, 2001. **48**(8): p. 911-20.

62. Chen, J., et al., *A multichannel neural probe for selective chemical delivery at the cellular level.* IEEE Trans Biomed Eng, 1997. **44**(8): p. 760-9.

63. Buzsaki, G., et al., *High-frequency network oscillation in the hippocampus.* Science, 1992. **256**(5059): p. 1025-7.

64. Najafi, K., J. Ji, and K.D. Wise, *Scaling limitations of silicon multichannel recording probes.* IEEE Trans Biomed Eng, 1990. **37**(1): p. 1-11.

65. Kim, K.H. and S.J. Kim, *Noise characteristic design of CMOS source follower and voltage amplifier for active semiconductor microelectrodes for neural signal recording.* Medical & Biological Engineering & Computing, 2000. **38**(4): p. 469-72.

66. Rinberg, D. and H. Davidowitz, *A stimulus generating system for studying wind sensation in the American cockroach.* Journal of Neuroscience Methods, 2002. **121**(1): p. 1-11.

67. Gozani, S.N. and J.P. Miller, *Optimal discrimination and classification of neuronal action potential waveforms from multiunit, multichannel recordings using software-based linear filters.* IEEE Trans Biomed Eng, 1994. **41**(4): p. 358-72.

68. Dimitrov, A.G. and J.P. Miller, *Analyzing sensory systems with the information distortion function.* Pac Symp Biocomput, 2001: p. 251-62.

69. Penev, P.S., A.G. Dimitrov, and J.P. Miller, *Characterization of and compensation for the nonstationarity of spike shapes during physiological recordings.* Neurocomputing, 2001. **38-40**: p. 1695-1701.

70. Theunissen, F., et al., *Information theoretic analysis of dynamical encoding by four identified primary sensory interneurons in the cricket cercal system.* J Neurophysiol, 1996. **75**(4): p. 1345-64.

71. Theunissen, F.E. and J.P. Miller, *Representation of sensory information in the cricket cercal sensory system. II. Information theoretic calculation of system accuracy and optimal tuning-curve widths of four primary interneurons.* J Neurophysiol, 1991. **66**(5): p. 1690-703.

72. Miller, J.P., G.A. Jacobs, and F.E. Theunissen, *Representation of sensory information in the cricket cercal sensory system. I. Response properties of the primary interneurons.* J Neurophysiol, 1991. **66**(5): p. 1680-9.

73. Turner, J.L., et al., *Changes in extracellular matrix expression following insertion of model neural prosthetic devises.* Journal of Neurochemistry, 2000. **74**: p. S82-S82.

74. Carter, R.R. and J.C. Houk, *Multiple single-unit recordings from the CNS using thin-film electrode arrays.* 1993.

75. Hetke, J.F., et al., *Silicon ribbon cables for chronically implantable microelectrode arrays.* IEEE Trans Biomed Eng, 1994. **41**(4): p. 314-21.

76. Ji, J., et al., *A low-noise demultiplexing system for active multichannel microelectrode arrays.* IEEE transactions on bio-medical engineering., 1991. **38(1)**: p. 75-81.

77. Hoogerwerf, A.C. and K.D. Wise, *A three-dimensional microelectrode array for chronic neural recording.* IEEE Trans Biomed Eng, 1994. **41**(12): p. 1136-46.

78. Maynard, E.M., et al., *The Utah intracortical Electrode Array: a recording structure for potential brain-computer interfaces.* Electroencephalography and clinical neurophysiology., 1997. **102(3)**: p. 228-39.

79. Normann, R.A., E. Richardson, and K.S. Guillory, *Retinal ganglion cell recordings with a high-density multi- electrode array.* Investigative Ophthalmology & Visual Science, 2001. **42**(4): p. 3640.

80. Reitboeck, H.J., *Fiber microelectrodes for electrophysiological recordings.* Journal of neuroscience methods., 1983. **8(3)**: p. 249-62.

81. Tanghe, S.J. and K.D. Wise, *A 16-Channel Cmos Neural Stimulating Array.* Ieee Journal of Solid-State Circuits, 1992. **27**(12): p. 1819-1825.

82. McCreery, D.B., W.F. Agnew, and J. McHardy, *Electrical characteristics of chronically implanted platinum-iridium electrodes.* IEEE transactions on bio-medical engineering., 1987. **34(9)**: p. 664-8.

83. Stensaas, S.S. and L.J. Stensaas, *The reaction of the cerebral cortex to chronically implanted plastic needles.* Acta neuropathologica., 1976. **35(3)**.

84. Yuen, T.G., W.F. Agnew, and P.C.U.S.A. Huntington Medical Research Institutes, *Histological evaluation of polyesterimide-insulated gold wires in brain.* Biomaterials., 1995. **16(12)**: p. 951-6.

85. Bovolenta, P., et al., *CNS glial scar tissue: a source of molecules which inhibit central neurite outgrowth.* Progress in brain research., 1992. **94**.

86. Norenberg, M.D. and U.o.M.S.o.M.F.L. Department of Pathology, *Astrocyte responses to CNS injury.* Journal of neuropathology and experimental neurology., 1994. **53(3)**: p. 213-20.

87. Norton, W.T., et al., *Quantitative aspects of reactive gliosis: a review.* Neurochemical research., 1992. **17(9)**: p. 877-85.

88. Eng, L.F., et al., *Astrocytic response to injury.* Progress in brain research., 1992. **94**.

89. Landis, D.M., *The early reactions of non-neuronal cells to brain injury.* Annual review of neuroscience., 1994. **17**.

90. Schiffer, D., et al., *Immunohistochemistry of glial reaction after injury in the rat: double stainings and markers of cell proliferation.* Journal of Developmental Neuroscience, 1993. **11(2)**: p. 269-80.

91. Szarowski, D.H., et al., *Brain Responses to Micro-machined Silicon Devices.* Brain Research, 2003 (submitted for publication).

92. Spataro, L., et al., *Dexamethasone Treatment Reduces Astroglia Responses to Inserted*

Neuroprosthetic Devices in Rat Neocortex. Journal of Neuroscience, 2003 (submitted for publication).

93. Gravesen, P., J. Branebjerg, and O.S. Jensen. *Microfluidics-a review*. 1993. Neuchatel, Switzerland.

94. Tritton, D.J., *Physical fluid dynamics*. 2nd ed. 1988, Oxford Oxfordshire New York: Clarendon Press ;

Oxford University Press. xvii, 519.

95. Retterer, S., et al., *Microfluidic Devices Used to Control Local Biochemical Environments During Implantation.* IEEE Transactions on Biomedical Engineering, 2003 (submitted for publication).

96. Maher, M.P., et al., *The neurochip: a new multielectrode device for stimulating and recording from cultured neurons.* J Neurosci Methods, 1999. **87**(1): p. 45-56.

97. Gross, G.W., *Simultaneous single unit recording in vitro with a photoetched laser deinsulated gold multimicroelectrode surface.* IEEE Trans Biomed Eng, 1979. **26**(5): p. 273-9.

98. Pine, J., *Recording action potentials from cultured neurons with extracellular microcircuit electrodes.* J Neurosci Methods, 1980. **2**(1): p. 19-31.

99. Novak, J.L. and B.C. Wheeler, *Multisite hippocampal slice recording and stimulation using a 32 element microelectrode array.* Journal of Neuroscience Methods, 1988. **23**(2): p. 149-59.

100. Jimbo, Y., H.P. Robinson, and A. Kawana, *Strengthening of synchronized activity by tetanic stimulation in cortical cultures: application of planar electrode arrays.* IEEE Trans Biomed Eng, 1998. **45**(11): p. 1297-304.

101. Thiebaud, P., et al., *An array of Pt-tip microelectrodes for extracellular monitoring of activity of brain slices.* Biosensors & Bioelectronics, 1999. **14**(1): p. 61-5.

102. Thiebaud, P., et al., *Microelectrode arrays for electrophysiological monitoring of hippocampal organotypic slice cultures.* IEEE Trans Biomed Eng, 1997. **44**(11): p. 1159-63.

103. Potter, S.M. and T.B. DeMarse, *A new approach to neural cell culture for long-term studies.* Journal of Neuroscience Methods, 2001. **110**(1-2): p. 17-24.

104. Britland, S., et al., *Morphogenetic guidance cues can interact synergistically and hierarchically in steering nerve cell growth.* Exp Biol. Online, 1996. **1**(2): p. 1-11.

105. Kleinfeld, D., K.H. Kahler, and P.E. Hockberger, *Controlled outgrowth of dissociated neurons on patterned substrates.* J Neurosci, 1988. **8**(11): p. 4098-120.

106. Stenger, D.A., et al., *Coplanar molecular assemblies of amino- and perflourinated alkylsilanes: characterization and geometric definition of mammalian cell adhesion and growth.* J. Amer. Chem. Soc., 1992. **114**: p. 8435-8442.

107. Lom, B., K.E. Healy, and P.E. Hockberger, *A versatile technique for patterning biomolecules onto glass coverslips.* J Neurosci Methods, 1993. **50**(3): p. 385-97.

108. Georger, J.H., et al., *Coplanar Patterns of Self-Assembled Monolayers for Selective Cell-Adhesion and Outgrowth.* Thin Solid Films, 1992. **210**(1-2): p. 716-719.

109. Letourneau, P.C., *Cell-to-substratum adhesion and guidance of axonal elongation.* Dev Biol, 1975. **44**(1): p. 92-101.

110. Bernard, A., et al., *Printing patterns of proteins.* Langmuir, 1998. **14**(9): p. 2225-2229.

111. Kane, R.S., et al., *Patterning proteins and cells using soft lithography.* Biomaterials, 1999. **20**(23-24): p. 2363-2376.

112. James, C.D., et al., *Aligned microcontact printing of micrometer-scale poly-L-lysine structures for controlled growth of cultured neurons on planar microelectrode arrays.* IEEE Trans Biomed Eng, 2000. **47**(1): p. 17-21.

113. Scholl, M., et al., *Ordered networks of rat hippocampal neurons attached to silicon oxide surfaces.* J Neurosci Methods, 2000. **104**(1): p. 65-75.

114. Lauer, L., et al., *Aligned microcontact printing of biomolecules on microelectronic device surfaces.* IEEE Transactions on Biomedical Engineering, 2001. **48**(7): p. 838-42.

115. Branch, D.W., et al., *Long-term stability of grafted polyethylene glycol surfaces for use with microstamped substrates in neuronal cell culture.* Biomaterials, 2001. **22**(10): p. 1035-47.

116. James, C.D., et al., *Patterned protein layers on solid substrates by thin stamp microcontact printing.* Langmuir, 1998. **14**(4): p. 741-744.

117. Ruardij, T.G., M.H. Goedbloed, and W.L. Rutten, *Adhesion and patterning of cortical neurons on polyethylenimine- and fluorocarbon-coated surfaces.* IEEE Trans Biomed Eng, 2000. **47**(12): p. 1593-9.

118. Buitenweg, J.R., et al., *Measurement of sealing resistance of cell-electrode interfaces in neuronal cultures using impedance spectroscopy.* Medical & Biological Engineering & Computing, 1998. **36**(5): p. 630-637.

119. Robinson, D.A., *The Electrical Properties of Metal Microelectrodes.* Proceedings of the IEEE, 1968. **56**(6): p. 1065-1071.

120. Weiland, J.D. and D.J. Anderson, *Chronic neural stimulation with thin-film, iridium oxide electrodes.* Ieee Transactions on Biomedical Engineering, 2000. **47**(7): p. 911-918.

121. Cobbold, R.S.C., *Transducers for biomedical measurements: principles and applications*. 1974, New York,: Wiley. xiv, 486.

122. James, C.D., et al., *Patterned protein layers on solid substrates by thin stamp microcontact printing.* Langmuir, 1998. **14**(4): p. 741-4.

123. Banker, G., H. Asmussen, and K. Goslin, *Rat Hippocampal neurons in low-density culture.* in Culturing Nerve Cells (2nd edition) G. Banker K. Goslin eds. Cambridge, MA: MIT Press, 1998, pp 339-370, 1998.

124. Brewer, G.J., et al., *Optimized survival of hippocampal neurons in B27-supplemented Neurobasal, a new serum-free medium combination.* J Neurosci Res, 1993. **35**(5): p. 567-76.

125. Lewicki, M.S., *A review of methods for spike sorting: the detection and classification of neural action potentials.* Network, 1998. **9**(4): p. R53-78.

126. Turner, A.M., et al., *Attachment of astroglial cells to microfabricated pillar arrays of different geometries.* J Biomed Mater Res, 2000. **51**(3): p. 430-41.

127. Spruston, N., et al., *Activity-Dependent Action-Potential Invasion and Calcium Influx into Hippocampal Ca1 Dendrites.* Science, 1995. **268**(5208): p. 297-300.

128. Mickus, T., H. Jung, and N. Spruston, *Properties of slow, cumulative sodium channel inactivation in rat hippocampal CA1 pyramidal neurons.* Biophys J, 1999. **76**(2): p. 846-60.

129. Golding, N.L., W.L. Kath, and N. Spruston, *Dichotomy of action-potential backpropagation in CA1 pyramidal neuron dendrites.* J Neurophysiol, 2001. **86**(6): p. 2998-3010.

130. Fromherz, P., *Extracellular recording with transistors and the distribution of ionic conductances in a cell membrane.* Eur Biophys J, 1999. **28**(3): p. 254-8.

131. Grattarola, M. and S. Martinoia, *Modeling the neuron-microtransducer junction: from extracellular to patch recording.* IEEE Trans Biomed Eng, 1993. **40**(1): p. 35-41.

132. Henze, D.A., et al., *Intracellular features predicted by extracellular recordings in the hippocampus in vivo.* J Neurophysiol, 2000. **84**(1): p. 390-400.

133. Hodgkin, A.L. and A.F. Huxley, *A Quantitative Description of Membrane Current and Its Application to Conduction and Excitation in Nerve.* Journal of Physiology-London, 1952. **117**(4): p. 500-544.

134. Regehr, W.G., et al., *Sealing cultured invertebrate neurons to embedded dish electrodes facilitates long-term stimulation and recording.* J Neurosci Methods, 1989. **30**(2): p. 91-106.

135. Akin, T., et al., *A micromachined silicon sieve electrode for nerve regeneration applications.* IEEE Trans Biomed Eng, 1994. **41**(4): p. 305-13.

136. BeMent, S.L., et al. *Silicon microelectrode impedance, geometry, and neural cell recording ability*. in *Proceedings of the Seventh Annual Conference of the IEEE/Engineering in Medicine and Biology Society. Frontiers of Engineering and Computing in Health Care - 1985*. 1985. Chicago, IL, USA: IEEE; New York NY USA.

137. Bragin, A., et al., *Multiple site silicon-based probes for chronic recordings in freely moving rats: implantation, recording and histological verification.* Journal of Neuroscience Methods, 2000. **98**(1): p. 77-82.

138. Chen, J. and K.D. Wise, *A silicon probe with integrated microheaters for thermal marking and monitoring of neural tissue.* IEEE Trans Biomed Eng, 1997. **44**(8): p. 770-4.

139. James, C., *Electrophysiological and Developmental Studies of Reconstructed Hippocampal Neuron Networks Using Microfabrication Techniques.* PhD Thesis, Cornell University, 2002.

140. Sakurai, T. and K. Tamaru, *Simple formulas for two- and three-dimensional capacitances.* IEEE Transactions on Electron Devices, 1983. **ED-30**(2): p. 183-5.

141. Spence, A.J., R.R. Hoy, and M.S. Isaacson, *A Micromachined Silicon Multielectrode for Multiunit Recording.* J Neurosci Methods, 2003 (in press).

142. Jacobs, G.A. and F.E. Theunissen, *Functional organization of a neural map in the cricket cercal sensory system.* J Neurosci, 1996. **16**(2): p. 769-84.

143. Miller, J.P. and G.A. Jacobs, *Relationships between neuronal structure and function.* J Exp Biol, 1984. **112**: p. 129-45.

144. Roddey, J.C. and G.A. Jacobs, *Information theoretic analysis of dynamical encoding by filiform mechanoreceptors in the cricket cercal system.* J Neurophysiol, 1996. **75**(4): p. 1365-76.

145. Murphey, R.K., et al., *Transplantation of cricket sensory neurons to ectopic locations: arborizations and synaptic connections.* J Neurosci, 1983. **3**(4): p. 659-72.

146. Clague, H., F. Theunissen, and J.P. Miller, *Effects of adaptation on neural coding by primary sensory interneurons in the cricket cercal system.* J Neurophysiol, 1997. **77**(1): p. 207-20.

147. Mizrahi, A. and F. Libersat, *Independent coding of wind direction in cockroach giant interneurons.* J Neurophysiol, 1997. **78**(5): p. 2655-61.

148. Paydar, S., C.A. Doan, and G.A. Jacobs, *Neural mapping of direction and frequency in the cricket cercal sensory system.* J Neurosci, 1999. **19**(5): p. 1771-81.

149. Jacobs, G.A. and F.E. Theunissen, *Extraction of sensory parameters from a neural map by primary sensory interneurons.* J Neurosci, 2000. **20**(8): p. 2934-43.

150. Jacobs, G.A. and R.K. Murphey, *Segmental origins of the cricket giant interneuron system.* J Comp Neurol, 1987. **265**(1): p. 145-57.

151. Wheeler, B.C. and S.R. Smith, *High-resolution alignment of action potential waveforms using cubic spline interpolation.* J Biomed Eng, 1988. **10**(1): p. 47-53.

152. Zouridakis, G. and D.C. Tam, *Identification of reliable spike templates in multi-unit extracellular recordings using fuzzy clustering.* Comput Methods Programs Biomed, 2000. **61**(2): p. 91-8.

153. Zouridakis, G. and D.C. Tam, *Multi-unit spike discrimination using wavelet transforms.* Comput Biol Med, 1997. **27**(1): p. 9-18.

154. Brown, G.D., S. Yamada, and T.J. Sejnowski, *Independent component analysis at the neural cocktail party.* Trends Neurosci, 2001. **24**(1): p. 54-63.

155. Kim, K.H. and S.J. Kim, *Neural spike sorting under nearly 0-dB signal-to-noise ratio using nonlinear energy operator and artificial neural-network classifier.* IEEE Trans Biomed Eng, 2000. **47**(10): p. 1406-11.

156. Mukhopadhyay, S. and G.C. Ray, *A new interpretation of nonlinear energy operator and its efficacy in spike detection.* IEEE Transactions on Biomedical Engineering, 1998. **45**(2): p. 180-7.

157. Maragos, P., J.F. Kaiser, and T.F. Quatieri, *On amplitude and frequency demodulation using energy operators.* IEEE Transactions on Signal Processing, 1993. **41**(4): p. 1532-50.

158. Wilson, M.A. and B.L. McNaughton, *Dynamics of the hippocampal ensemble code for space.* Science, 1993. **261**(5124): p. 1055-8.

159. Gray, C.M., et al., *Tetrodes markedly improve the reliability and yield of multiple single-unit isolation from multi-unit recordings in cat striate cortex.* J Neurosci Methods, 1995. **63**(1-2): p. 43-54.

160. Rinberg, D. and H. Davidowitz, *Multineuron response to wind stimuli in the American cockroach.* Neurocomputing, 2001. **38-40**: p. 837-843.

161. Baba, Y., H. Masuda, and T. Shimozawa, *Proportional inhibition in the cricket medial giant interneuron.* J Comp Physiol [A], 2001. **187**(1): p. 19-25.

162. Bodnar, D.A., J.P. Miller, and G.A. Jacobs, *Anatomy and physiology of identified wind-sensitive local interneurons in the cricket cercal sensory system.* J Comp Physiol [A], 1991. **168**(5): p. 553-64.

163. Kloppenburg, P. and H.O. M, *Voltage-activated currents in identified giant interneurons isolated from adult crickets gryllus bimaculatus.* J Exp Biol, 1998. **201 (Pt 17)**: p. 2529-41.

164. Deurloo, K.E., J. Holsheimer, and H.B. Boom, *Transverse tripolar stimulation of peripheral nerve: a modelling study of spatial selectivity.* Med Biol Eng Comput, 1998. **36**(1): p. 66-74.

165. Grill, W.M. and J.T. Mortimer, *Stability of the input-output properties of chronically implanted multiple contact nerve cuff stimulating electrodes.* IEEE Trans Rehabil Eng, 1998. **6**(4): p. 364-73.

166. Grill, W.M., Jr. and J.T. Mortimer, *Quantification of recruitment properties of multiple contact cuff electrodes.* IEEE Trans Rehabil Eng, 1996. **4**(2): p. 49-62.

167. Surlykke, A., et al., *Hearing in hooktip moths (Drepanidae: Lepidoptera).* J Exp Biol, 2003. **206**(15): p. 2653-2663.

168. Payne, R.S., K.D. Roeder, and J. Wallman, *Directional sensitivity of the ears of noctuid moths.* The Journal of experimental biology., 1966. **44(1)**: p. 17-31.

169. Roeder, K.D., *Auditory system of noctuid moths.* Science., 1966. **154(756)**: p. 1515-21.

170. Roeder, K.D. and R.S. Payne, *Acoustic orientation of a moth in flight by means of two sense cells.* Symposia of the Society for Experimental Biology., 1966. **20**.

171. Roeder, K.D., *Acoustic alerting mechanisms in insects.* Annals of the New York Academy of Sciences., 1971. **188**: p. 63-79.

172. Roeder, K.D., *Responses of the less sensitive acoustic sense cells in the tympanic organs of some noctuid and geometrid moths.* Journal of insect physiology., 1974. **20(1)**: p. 55-66.

173. Roeder, K.D., *Neural factors and evitability in insect behavior.* The Journal of experimental zoology., 1975. **194(1)**: p. 75-88.

174. Roeder, K.D., *Acoustic sensitivity of the noctuid tympanic organ and its range for the cries of bats.* Journal of insect physiology., 1966. **12(7)**: p. 843-59.

175. Buzsaki, G., et al., *Pattern and inhibition-dependent invasion of pyramidal cell dendrites by fast spikes in the hippocampus in vivo.* Proceedings of the National Academy of Sciences of the United States of America, 1996. **93**(18): p. 9921-9925.

176. Chang, J.C., G.J. Brewer, and B.C. Wheeler, *Modulation of neural network activity by patterning.* Biosens Bioelectron, 2001. **16**(7-8): p. 527-33.

177. Gross, G.W., et al., *Odor, drug and toxin analysis with neuronal networks in vitro: extracellular array recording of network responses.* Biosens Bioelectron, 1997. **12**(5): p. 373-93.

178. Gaietta, G., et al., *Multicolor and electron microscopic imaging of connexin trafficking.* Science., 2002. **296(5567)**: p. 503-7.

179. Roth, B.J. and J. Wikswo, John P., *The electrical potential and the magnetic field of an axon in a nerve bundle.* Mathematical Biosciences, 1985. **76**(1): p. 37-57.

180. Blatt, M., S. Wiseman, and E. Domany, *Superparamagnetic clustering of data.* Physical Review Letters, 1996. **76**(18): p. 3251-3254.